Low-Frequency Noise in SiGe HBTs and Lateral BJTs

A Thesis
Presented to
The Academic Faculty

by

Enhai Zhao

In Partial Fulfillment
of the Requirements for the Degree
Doctor of Philosophy

School of Electrical and Computer Engineering
Georgia Institute of Technology
December 2006

Low-Frequency Noise in SiGe HBTs and Lateral BJTs

Approved by:

Professor John D. Cressler, Advisor
School of Electrical and Computer Engineering
Georgia Institute of Technology

Professor Joy Laskar
School of Electrical and Computer Engineering
Georgia Institute of Technology

Professor Ioannis Papapolymerou
School of Electrical and Computer Engineering
Georgia Institute of Technology

Professor William D. Hunt
School of Electrical and Computer Engineering
Georgia Institute of Technology

Professor Phillip First
School of Physics
Georgia Institute of Technology

ACKNOWLEDGEMENTS

I would like to express my sincere gratitude to all those who gave me the opportunity to complete this thesis.

I wish to express my deepest thanks to my advisor, Dr. John D. Cressler. Thank you for educating me, for supporting my PhD work, and most importantly, for showing me the essence of life as a scientific researcher.

I would like to sincerely thank Dr. Joy Laskar, Dr. Ioannis Papapolymerou, Dr. William D. Hunt, and Dr. Phillip First, who served as my committee members, for all their valuable comments and corrections.

Thank you to all my colleagues in our group: Dr. Zhenrong Jin, Dr. Jarle Johansen, Dr. Qingqing Liang, Dr. Tianbing Chen, Ramkumar Krithivasan, Chendong Zhu, Yuan Lu, Joel Andrews, Lance Kuo, Jon Comeau, Xiangtao Li, Marco Bellini, Laleh Najafizadeh, Aravind Appasamy, Curtis Grens, Akil Sutton, Becca Haugerud, Peng Cheng, Jiahui Yuan, Dr. A. P. Gnana Prakash, Dr. Bongim Jun. This work could not have been accomplished without their significant contributions.

I also want to thank my parents, Hongzhong Zhao and Junmei Dong, for their constant support throughout the years and for showing me the value of hard work by their own examples.

TABLE OF CONTENTS

ACKNOWLEDGEMENTS . . . . **iii**

LIST OF TABLES . . . . **vi**

LIST OF FIGURES . . . . **vii**

SUMMARY . . . . **xi**

I INTRODUCTION **1**

- 1.1 LFN 1
  - 1.1.1 Wiener-Khintchine Theorem 1
  - 1.1.2 Thermal Noise 3
  - 1.1.3 Shot Noise 4
  - 1.1.4 Random Telegraph Signal Noise 5
  - 1.1.5 Generation-Recombination Noise 7
  - 1.1.6 Flicker Noise 10
- 1.2 Development of Complementary SiGe HBTs 12
  - 1.2.1 SiGe HBT Technology 13
  - 1.2.2 Complementary SiGe HBTs 16
- 1.3 LFN in SiGe HBTs 18
- 1.4 LFN in Lateral BJTs 19
- 1.5 Scope of the Thesis 20

II TECHNIQUES FOR LFN MEASUREMENTS ON BJTS **24**

- 2.1 Introduction 24
- 2.2 Measurement Setup 24
- 2.3 Hybrid-π Model for LFN Measurement 25

III PHYSICAL LFN MODELS FOR SIGE HBTS **30**

- 3.1 Introduction 30
- 3.2 Carrier Random-Walk Model 32
- 3.3 Two-Step Tunneling Model 34
- 3.4 Tunneling-Assisted Trapping Model 35

IV LFN IN COMPLEMENTARY SIGE HBTS 38

4.1 Introduction 38

4.2 Effects of the IFO on LFN 40

4.3 Effects of Temperature on LFN 42

4.4 Effects of Proton Radiation on LFN 45

4.5 Effects of Geometric Scaling on LFN 48

4.6 Physics of LFN in Complementary SiGe HBTs 50

V THE GEOMETRICAL DEPENDENCE OF LFN IN NPN SIGE HBTS 59

5.1 Introduction 59

5.2 L_E Effects 62

5.3 XEC and XTC Effects 64

5.4 Discussion 65

VI LFN OF LATERAL BJTS 73

6.1 Introduction 73

6.2 DC and AC Characteristics 73

6.3 LFN in Lateral BJTs 77

VII CONCLUSIONS AND FUTURE WORK 82

APPENDIX A — DERIVATION OF FLUCTUATIONS FROM TRAPS 85

APPENDIX B — THE TUNNELING COMPONENT OF THE BASE CURRENT . 98

REFERENCES 101

VITA 108

LIST OF TABLES

1 SPICE noise parameters K_F and A_F and $D_{it}(E_{FNm})/C_{mo}^2$ (refer to Section 4.6) for npn+pnp SiGe complementary HBTs with A_E=0.4×6.4 μm^2. 44

2 Peak current gain and threshold voltage for lateral *pnp* BJTS using a NCOLL + NBL design approach (GOX represents the gate oxide). 74

LIST OF FIGURES

1 Schematic base bandgap in a SiGe HBT with a linearly graded Ge profile. 14

2 Energy band diagram for a *pnp* SiGe HBT with a linearly graded and a retrograded Ge profile. 16

3 Block diagram for the base-collector dual channel power spectral density measurement system. 25

4 Hybrid-π model for the base-collector dual-channel LFN measurement system. . . 25

5 Typical power spectral densities S_{VB} and S_{VC} measured from the dual-channel system for a *pnp* SiGe HBT at I_B=8.0 μm with A_E=0.4×6.4μm^2. 28

6 Extracted power spectral densities S_{IB} from S_{VB} and S_{VC} and measured coherence data for a *pnp* SiGe HBT at I_B=8.0 μm with A_E=0.4×6.4 μm^2. 29

7 Schematic of carrier transport processes of the random-walk model for IFO interface states in a *pnp* device. 32

8 Schematic of IFO for two-step tunneling model for a *pnp* device. 34

9 Schematic cross section of *npn*+*pnp* SiGe complementary HBTs (SIC is the self-aligned collector implant, BPSG is the boro-phospho-silicate glass). 38

10 Gummel characteristics for *pnp* SiGe HBTs with different IFO thicknesses, but with the same emitter area A_E=0.4×6.4 μm^2, at V_{BC}=0.5 V. 39

11 The base saturation current and the emitter resistance as a function of IFO thickness. Data measured from *pnp* SiGe HBTs with A_E=0.4×6.4 μm^2, and V_{BC}=0.5 V. λ_{ci} is the characteristic IFO thickness for I_B. 40

12 Noise spectra for *pnp* SiGe HBTs with the same A_E=0.4×6.4 μm^2 but different IFO thicknesses at I_B=1.0 μA and V_{BC}=0.5 V. 41

13 The dependence of LFN on I_B for *pnp* SiGe HBTs with different IFO thicknesses but the same A_E=0.4×6.4 μm^2, at V_{BC}=0.5 V and f=10 Hz. 42

14 The dependence of LFN on the IFO thickness at different I_B. The spectral densities are for *pnp* SiGe HBTs with A_E=0.4×6.4 μm^2, with V_{BC}=0.5 V and f=10 Hz. λ_{cn} is the characteristic IFO thickness for LFN. 43

15 Gummel characteristics for *npn* and *pnp* SiGe HBTs with A_E=0.4×6.4 μm^2 and V_{BC}=0.0 V at different temperatures. 44

16 Typical noise spectra for *npn* and *pnp* SiGe HBTs with A_E=0.4×6.4 μm^2, I_B=1.0 μA and $|V_{BC}|$=0.5 V at different temperatures. 45

17 The noise magnitude dependence of *npn* and *pnp* SiGe HBTs with A_E=0.4×6.4 μm^2 and $|V_{BC}|$=0.5 V on I_B at different temperatures. 46

18 The LFN of *npn* and *pnp* SiGe HBTs as a function of temperature at different base currents with A_E=0.4×6.4 μm^2, $|V_{BC}|$=0.5 V, and f=10 Hz. 47

19 Gummel characteristics of pre- and post-irradiated complementary SiGe HBTs with A_E=0.4×3.2 μm^2 at V_{CB}=0.0 V. 48

20 Current gain degradation of complementary SiGe HBTs with A_E=0.4×0.8 μm^2 and A_E=0.4×3.2 μm^2 at V_{CB}=0.0 V. 49

21 I_B degradation as a function of fluence in forward mode for complementary SiGe HBTs with A_E=0.4×0.8 μm^2 and A_E=0.4×3.2 μm^2 at V_{CB}=0.0 V and $|V_{BE}|$=0.6 V. 50

22 I_B degradation as a function of fluence in inverse mode for complementary SiGe HBTs with A_E=0.4×0.8 μm^2 and A_E=0.4×3.2 μm^2 at V_{CB}=0.0 V and $|V_{BE}|$=0.6 V. 51

23 S_{IB} at different base currents for a *pnp* SiGe HBT with A_E=0.4×6.4 μm^2 at V_{BC}=0.5 V. 52

24 Extracted power spectra densities S_{IB} at 10 Hz as a function of the emitter area at $|V_{BC}|$=0.5 V. 53

25 Comparison of the pre-radiation and the post-radiation S_{IB} spectra for both *npn* and *pnp* SiGe HBTs with A_E=0.4×6.4 μm^2 at $|V_{BC}|$=0.5 V. 54

26 Effects of irradiation on the bias dependence of LFN at 10 Hz for both *npn* and *pnp* SiGe HBTs with A_E=0.4×6.4 μm^2 at $|V_{BC}|$=0.5 V. 55

27 Effects of irradiation on the bias dependence of LFN at 10 Hz in *npn* SiGe HBTs with different interfacial oxide thicknesses and A_E=0.4×6.4 μm^2 at V_{CB}=0.5 V. . . 56

28 Noise power spectral densities measured from two identical transistors for *npn* and *pnp* SiGe HBTs, respectively, with the emitter area A_E=0.4×0.8 μm^2 at I_B=1.0 μA and $|V_{BC}|$ = 0.5 V. The model discussed in Section 4.6 is used for simulation with $\tau_0 \approx 2.2 \times 10^{-6}$ s, $\lambda \approx 0.8$Å, $N_{IFO}(E_{FNm}, z, t_{ox})/C_{mo}^2$ for z ranging from 5.0 Å to 5.1 Å around 5.0×10^{29} cm·F^{-2}·eV^{-1}, $D_{it}(E_{FNm})/C_{mo}^2 \approx 3.0\times10^{20}$ cm^2 · F^{-2}·eV^{-1}. 57

29 Noise variation coefficient versus emitter area for *npn* SiGe HBTs with t_{ox}=5.2 Å and *pnp* SiGe HBTs with t_{ox}=5.9 Å. 58

30 Schematic cross-section of a *npn* SiGe HBT. 59

31 Gummel characteristics of *npn* SiGe HBTs with different emitter length L_E. Data were measured from *npn* SiGe HBTs with W_E=0.4 μm, XEC=0.4 μm, and V_{CB}=0.5 V. 60

32 The base saturation current I_{B0} as a function of the emitter length L_E for *npn* SiGe HBTs with L_E between 0.5 μm and 20.0 μm. Data were measured from *npn* SiGe HBTs with W_E=0.4 μm, XEC=0.4 μm, and V_{CB}=0.5 V. 61

33 The multiplication product of S_{IB} and A_E at I_B=1.0 μA versus frequency for *npn* SiGe HBTs with different L_E. Data were measured from *npn* SiGe HBTs with W_E=0.4 μm, XEC=0.4 μm and V_{CB}=0.5 V. 62

34 The product of the magnitude of $1/f$ noise S_{IB} at 10 Hz and A_E versus I_B with different L_E. Data were measured from *npn* SiGe HBTs with W_E=0.4 μm, XEC=0.4 μm and V_{CB}=0.5 V. 63

35 The SPICE noise parameter A_F as a function of the emitter length L_E. For each L_E, data were measured from *npn* SiGe HBTs with W_E=0.4 μm, XEC=0.4 μm and V_{CB}=0.5 V on seven different dies. 64

36 Normalized noise magnitude S_{IB} at 10 Hz to unity for the shortest L_E as a function of the emitter length L_E. Data were measured from *npn* SiGe HBTs with W_E=0.4 μm, XEC=0.4 μm and V_{CB}=0.5 V. I_p^2/P_E is defined in Section 5.4. 65

37 The noise coefficient δ at I_B=1.0 μA as a function of A_E. For each A_E, data were measured from *npn* SiGe HBTs with W_E=0.4 μm, XEC=0.4 μm and V_{CB}=0.5 V on seven different dies. 66

38 Typical noise power spectral densities S_{IB} measured from devices with A_E=0.4×5.0 μm^2 and different XEC at I_B=1.0 μA and V_{CB}=0.5 V versus frequency. 67

39 The magnitude of $1/f$ noise, S_{IB} at 10 Hz, measured from devices with A_E=0.4×5.0 μm^2 and V_{CB}=0.5 V as a function of the base current I_B. 68

40 Normalized $1/f$ noise magnitude, S_{IB} at 10 Hz, to unity for the shortest XEC with A_E=0.4×5.0 μm^2 and V_{CB}=0.5 V versus XEC at different base currents. 69

41 The magnitude of $1/f$ noise, S_{IB} at 10 Hz, measured from devices with A_E=0.25×5.0 μm^2, XEC=0.25 μm, but different XTC at V_{CB}=0.5 V as a function of I_B. 70

42 The base saturation current I_{B0} per unit area versus the ratio of the emitter perimeter P_E to the emitter area A_E. Data were measured from devices with W_E=0.4 μm, XEC=0.4 μm and V_{CB}=0.5 V. C_i and C_p extracted from the region at P_E/A_E=9.0 μm^{-1} are roughly 3.59×10^{-20} A/μm^2 and 9.63×10^{-21} A/μm, respectively. When 5.1 μm$^{-1}\leq P_E/A_E \leq$7.0 μm^{-1}, C_i and C_p are 3.99×10^{-21} A/μm^2 and 1.42×10^{-20} A/μm, respectively. 71

43 The collector current and the substrate vertical current vs. the emitter-base voltage for a lateral *pnp* BJT with different base profiles. The gate is tied to the emitter ($V_{GE} = 0.0V$) and $V_{BC} = 0.0V$. 73

44 The collector current normalized to emitter perimeter I_C/P_E and the base current density (I_B/A_E) of lateral *pnp* BJTs with different emitter geometries as a function of V_{EB} at $V_{GB} = 1.0V$ (pMOS is off), and $V_{BC} = 0.0V$. 75

45 β as a function of P_E/A_E for lateral a *pnp* BJT with $W_B = 0.40\mu m$. HV pMOS has HiPLDD in both the emitter and the collector. LV pMOS has no HiPLDD. 76

46 Typical cut-off frequency f_T for a lateral *pnp* BJT built with the NCOLL + NBL profile, HV pMOS, and $W_B = 0.40\mu m$. 77

47 Typical collector current noise power spectral densities for lateral *pnp* BJTs with the NWELL + NBL profile, HV pMOS and $W_B = 0.40\mu m$ (V_{GB}=1.0 V (pMOS is off)). 78

48 S_{IC} at 10 Hz as a function of I_C for lateral *pnp* BJTs with the NCOLL + NBL profile (V_{GB}=1.0 V (pMOS is off)). 79

49 S_{IC} at 10 Hz as a function of I_C for lateral *pnp* with the NWELL + NBL profile (V_{GB}=1.0 V (pMOS is off)). 80

50 Calculated S_{IC} as a function of A_E for lateral *pnp* BJTs with the NWELL + NBL profile. V_{GB}=1.0V (PMOS off). 81

51 The processes involved in recombination through traps: (a) electron capture, (b) electron emission, (c) hole capture, (d) hole emission. 91

SUMMARY

The objective of the research reported here was to characterize the low-frequency noise (LFN) in both the silicon-germanium heterojunction bipolar transistor (SiGe HBT) and the lateral silicon bipolar junction transistor (BJT).

This work constitutes a comprehensive investigation of the LFN behavior in complementary SiGe HBTs, including the geometric dependence of LFN, the dependence of $1/f$ noise on interfacial oxide (IFO) thicknesses and temperatures, and the radiation response of $1/f$ noise. It also examines the LFN of lateral BJTs and proposes an application-oriented research approach for investigating the LFN of advanced bipolar technologies.

Details of this dissertation can be found in the following refereed publications:

1. Novel dual-channel LFN measurement system (Chapter II, also published in [1]).
2. Physical noise models for the LFN of SiGe HBTs (Chapter III, also published in [1][2]).
3. The characteristics of LFN in complementary SiGe HBTs (Chapter IV, also published in [1][2]).
4. The characteristics of LFN in *npn* SiGe HBTs with different geometries (Chapter V, also submitted in [3]).
5. The characteristics of LFN in lateral BJTs (Chapter VI, also published in [4]).

CHAPTER I

INTRODUCTION

1.1 LFN

The voltage and current fluctuations at the terminals of electronic devices that are usually referred to as noise originate from random microscopic behavior of the charge carriers within electronic devices. Noise, which exists in almost all semiconductor materials, is one of the fundamental properties associated with semiconductor devices. Normally, since noise sets the lowest detectable signal level, it is regarded as an unwanted disturbing random signal. However, useful information such as material purity, defect density, and material reliability can be captured by analyzing noise. Thus, understanding noise can help device designers minimize its impact on circuits and systems, probe carrier transport mechanisms, and characterize defects in materials. Therefore, noise investigation has become a useful tool in studying materials and devices. LFN normally refers to random fluctuations under 100 KHz, which imposes a practical limit on the performance of all electronic devices, including complementary SiGe HBTs and lateral BJTs. LFN, incorporating all the general features of noise, has a unique noise mechanism and impact on circuits and systems. Hence, it has been a topic of interest for decades.

In this section, a brief review of the standard mathematical methods used to describe a completely random waveform, namely Wiener-Khintchine theorem and autocorrelation functions, is briefly introduced. Then, five major types of LFN, including thermal noise, shot noise, random telegraph signal noise (RTS noise), generation-recombination noise (G-R noise), and flicker noise ($1/f$ noise) are discussed.

1.1.1 Wiener-Khintchine Theorem

Since the instantaneous values of a random (stochastic) process cannot be predicted, its average statistical properties are employed to characterize this process. One of those convenient statistical measures is the autocorrelation function, which describes the correlation between the process at different points in time. For a statistically stationary process, following [5], the autocorrelation function can be given by

$$< x(t)x(t+\tau) >= \lim_{T\to\infty} \frac{1}{T} \int_{-T/2}^{T/2} x(t)x(t+\tau)dt \tag{1}$$

where T is the duration of the measurement. Thus, $< x(t)x(t+\tau) >$ is independent of t for a statistically stationary process.

Fourier transforms, which are normally used in a strictly periodic function, can be used to determine the average spectrum of this stochastic process, where the period tends to infinity. Here, the Fourier transform is defined by

$$X(f) = \int_{-\infty}^{\infty} x(t)exp(-j2\pi ft)dt \tag{2}$$

$$x(t) = \int_{-\infty}^{\infty} X(f)exp(j2\pi ft)df \tag{3}$$

According to Parseval's theorem,

$$\int_{-\infty}^{\infty} x_1(t)x_2^*(t)dt = \int_{-\infty}^{\infty} X_1(f)X_2^*(f)df \tag{4}$$

Hence,

$$\int_{-\infty}^{\infty} |x(t)|^2 dt = \int_{-\infty}^{\infty} |X(f)|^2 df \tag{5}$$

which presents the total energy of the fluctuations. Therefore, the average power can be obtained by

$$\lim_{T\to\infty} \frac{1}{T} \int_{-\infty}^{\infty} |x(t)|^2 dt = \lim_{T\to\infty} \int_{0}^{\infty} \frac{2|X(f)|^2}{T} df \tag{6}$$

where the term $2|X(f)|^2/T$ has units of power per hertz. Thus, the average power spectral density for this stochastic process is given by

$$S(f) = \lim_{T\to\infty} \frac{< 2|X(f)|^2 >}{T} \tag{7}$$

Finally, the power spectral density is correlated to the autocorrelation function via the Wiener-Khintchine theorem

$$< x(t)x(t+\tau) >= \int_0^\infty S(f) cos(2\pi f\tau) df \tag{8}$$

$$S(f) = 4\int_0^\infty < x(t)x(t+\tau) > cos(2\pi f\tau) d\tau \tag{9}$$

The practical measurement of $S(f)$ will be discussed in Chapter II.

1.1.2 Thermal Noise

Thermal noise (Johnson noise, or Nyquist noise), which was first measured and characterized by J.B. Johnson [6] and H. Nyquist [7], originates from the equilibrium fluctuations of the electric current inside an electrical conductor. Due to the random thermal motion of electrons, thermal noise exists regardless of any applied voltage. Hence, thermal noise should be distinguished from other noise, which normally consists of current fluctuations when an applied voltage forces a macroscopic current to flow. Following Nyquist's theorem, the thermal noise source can be presented either as a source S_v in units of voltage power spectral density in series with resistance R, or as a source S_i in units of current power spectral density in parallel to conductance G, where

$$S_v = 4kTRp(f) \tag{10}$$

$$S_i = 4kTGp(f) \tag{11}$$

and

$$p(f) = \frac{hf}{kT}[\frac{1}{2} + \frac{1}{exp(\frac{hf}{kT} - 1)}] \tag{12}$$

The term p_f is close to unity over a broad range from the infrared region at room temperature to the GHz region at cryogenic temperatures [8]. Hence, (10) and (11) at low-frequency (<100 KHz) can be rewritten to

$$S_v = 4kTR \tag{13}$$

$$S_i = 4kTG \tag{14}$$

Therefore, thermal noise can be considered as a kind of white noise at low-frequency. In addition, thermal noise occurs in any impedance, regardless of whether it is a real resistance or an equivalent impedance.

1.1.3 Shot Noise

Shot noise is a type of noise caused by the random thermal motion of individual charge carriers in a overall *dc* current. The magnitude of shot noise increases as the average amplitude of the current increases. Shot noise is always associated with a *dc* current and cannot be observed without applying biasing currents.

Shot noise has been studied for a long time. W. Schottky reported shot noise in tubes and developed Schottky's theorem in 1918 [9]. Later, S. O. Rice analyzed shot noise based on the underlying Poisson process, which has a constant intensity [10]. Hence, the physics of shot noise is generally explained by the Poisson process. The following is a simplified method that can be used to derivate the magnitude of the current power spectral density for shot noise using the properties of the Poisson process. Assuming N carriers pass a point in a time interval τ at a net rate n, then

$$< N > = < n > \tau \tag{15}$$

One can also define another random process Y as

$$Y = \frac{\triangle N}{\tau} \tag{16}$$

where $\triangle N = N - < N >$. Since this is a Poisson process, $<N>=<\triangle N^2>$. Then,

$$< Y^2 > = \frac{< \triangle N^2 >}{\tau^2} = \frac{< N >}{\tau^2} = \frac{< n > \tau}{\tau^2} = \frac{< n >}{\tau} \tag{17}$$

Applying the Wiener-Khintchine theorem yields

$$S_Y(0) = \int_{-\infty}^{\infty} < Y^2 > d\tau = \lim_{\tau \to \infty} 2\tau < Y^2 > = 2 < n > \tag{18}$$

Note that only S_Y at 0 Hz is calculated here. Therefore, the current power spectral density for shot noise is defined by

$$S_i = q^2 S_Y(0) = 2q^2 < n > = 2qI \tag{19}$$

where the *dc* current $I=q<n>$. In addition, as with thermal noise, shot noise can also be considered as white noise at low-frequencies.

1.1.4 Random Telegraph Signal Noise

Random telegraph signal noise (RTS noise) is a set of random discrete pulses in the applied current, and is normally observed in small-size devices such as short-channel MOSFETs. RTS noise has also been reported in SiGe HBTs as the device geometry continues to scale down [11]. With the decreasing size of device geometry, the distribution of traps inside the devices becomes non-uniform. Hence, the trapping-detrapping processes associated with individual trapping centers become very important. RTS noise is generally believed to originate from these traps.

The power spectral density of RTS noise was first derived by Machlup [12], who briefly discussed how to evaluate RTS noise. Initially, one can assume that state 0 associated with the average time interval $<\tau_0>$ has an amplitude x_0=0, and state 1 associated with the average time interval $<\tau_1>$ has an amplitude x_1=$\triangle I$ [12][13]. Thus, the probabilities that RTS noise is present in state 0 and state 1 at any given time are given by

$$P_0 = \frac{<\tau_0>}{<\tau_0> + <\tau_1>} \tag{20}$$

and

$$P_1 = \frac{<\tau_1>}{<\tau_0> + <\tau_1>} \tag{21}$$

respectively. Then, the autocorrelation of RTS noise is expressed by

$$c(\tau) =< x(t)x(t+\tau) >= \sum_{i=0}^{1}\sum_{j=0}^{1} x_i x_j P_i(t)P_{ij}(t+\tau) \tag{22}$$

where $P_{ij}(t+\tau)$ is the probability that $x(t+\tau) = x_j$ under the condition x_t=x_i. As x_0=0 and x_1=$\triangle I$, (22) can be rewritten to

$$c(\tau) = (\triangle I)^2 P_1(t)P_{11}(t+\tau) \tag{23}$$

Here, $P_{11}(t+\tau)$ is the probability of $x(t+\tau) = x_1$; in other words, $P_{11}(t+\tau)$ is the probability of an even number of transitions in time interval τ, initializing from state 1 at time t. Similarly, $P_{10}(t+\tau)$

is defined as the probability of an odd number of transitions in time interval τ, initializing from state 1 at time t. Assuming τ is small enough, $P_{11}(t+\tau)$ can be given by the sum of two independent events: 1) an odd number of transitions in t with one transition in τ, and 2) an even number of transitions in t with no transition in τ. Therefore,

$$P_{11}(t+\tau) = P_{10}(t)\frac{\tau}{<\tau_0>} + P_{11}(t)(1 - \frac{\tau}{<\tau_1>}) \tag{24}$$

Since P_{11}+P_{10}=1, (24) can be revised to

$$\frac{dP_{11}(t)}{dt} + P_{11}(t)(\frac{1}{<\tau_0>} + \frac{1}{<\tau_1>}) = \frac{1}{<\tau_0>} \tag{25}$$

Note that when $P_{11}(0)$=1, the solution for (25) is

$$P_{11}(t) = \frac{<\tau_1>}{<\tau_0> + <\tau_1>} + \frac{<\tau_0>}{<\tau_0> + <\tau_1>}exp[-(\frac{1}{<\tau_0>} + \frac{1}{<\tau_1>})t] \tag{26}$$

Substituting (26) and (23) into (9), the current power spectral density of RTS noise is

$$S_i(f) = \frac{4\triangle I^2}{(<\tau_0> + <\tau_1>)[(\frac{1}{<\tau_0>} + \frac{1}{<\tau_1>})^2 + (2\pi f)^2]}, \tag{27}$$

which shows a Lorentzian spectrum.

1.1.5 Generation-Recombination Noise

Generation-recombination noise (G-R noise), like RTS noise, is generally due to the trapping-detrapping processes of charge carriers. However, G-R noise does not show discrete detectable pulse signals in the time domain. G-R noise has been investigated in numerous materials and devices [14][15], and is often employed as a diagnostic tool in probing the defects in semiconductor devices and materials [8][16]. This section introduces the basic principles of G-R noise with a single carrier life-time constant, which is very helpful in investigating more complex G-R noise phenomena and flicker noise in devices.

G-R noise, for simple cases, can be described by a fluctuation in the number N of charged carriers and arises due to the trapping centers that have a predominant life-time such as deep-lying donors or acceptors and Shockley-Read-Hall centers. The fluctuation in N is defined by

$$\frac{dN}{dt} = G(N) - R(N) + \triangle G(t) - \triangle R(t) \tag{28}$$

where $G(N)$ and $R(N)$ are the generation and recombination rates of the charged carriers, respectively, and $\triangle G(t)$ and $\triangle R(t)$, which generate shot noise, are the variance of $G(N)$ and $R(N)$, respectively. At equilibrium, N can be given by $N \approx N_0 + \triangle N$, where N_0 is the equilibrium number of charged carriers and $\triangle N$ is the first order variance of N. Hence, $G(N)$ and $R(N)$ can be expanded in a Taylor series as

$$G(N) \approx G(N_0) + \frac{dG}{dN}|_{N=N_0} \triangle N \tag{29}$$

and

$$R(N) \approx R(N_0) + \frac{dR}{dN}|_{N=N_0} \triangle N \tag{30}$$

Since $G(N_0)$=$R(N_0)$ in an equilibrium state, a predominant life-time τ can be defined by

$$\tau = [(\frac{dG}{dN} - \frac{dR}{dN})|_{N=N_0}]^{-1} \tag{31}$$

(28) is rewritten to

$$\frac{d\triangle N}{dt} = \frac{\triangle N}{\tau} + \triangle G(t) - \triangle R(t) \tag{32}$$

Applying a Fourier transform to (32) yields

$$j\omega F(\triangle N) = \frac{F(\triangle N)}{\tau} + F(\triangle G) - F(\triangle R) \tag{33}$$

So

$$F(\triangle N) = \frac{\tau[F(\triangle R) - F(\triangle G)]}{1 - j\omega\tau} \tag{34}$$

Hence, the power spectral density for the fluctuation in N is given by

$$S_N(f) = \frac{\tau^2[S_G(f) + S_R(f)]}{1 + \omega^2\tau^2} \tag{35}$$

Since $S_G(f)$ and $S_R(f)$ correspond to the shot noise generated by $\triangle G(t)$ and $\triangle R(t)$, respectively, they are given by

$$S_G(f) = 2G(N_0) = 2R(N_0) = S_R(f) \tag{36}$$

Hence, (35) is rewritten to

$$S_N(f) = 4G(N_0)\frac{\tau^2}{1 + \omega^2\tau^2} \tag{37}$$

The average power of this fluctuation is given by

$$< \triangle N^2 >= \int_0^\infty S_N(f)df = G(N_0)\tau \tag{38}$$

Substituting (38) into (37) yields

$$S_N(f) = 4 < \triangle N^2 > \frac{\tau}{1+\omega^2\tau^2} \tag{39}$$

If the fluctuation is dominated by trapping-detrapping processes via Shockley-Read-Hall centers, one can substitute (142) in Appendix A into (39) yielding

$$\triangle S_N(f) = 4N_t f(E_t)[1 - f(E_t)]\frac{\tau}{1+\omega^2\tau^2}\triangle E \tag{40}$$

where $\triangle S_N(f)$ is the power spectral density per unit volume, N_t is the trap density in units of $(cm^{-3} \cdot eV^{-1})$, $f(E_t)$ is the trap Fermi-Dirac distribution with trap energy E_t, and $\triangle E$ is the trap energy bandwidth determined by $f(E_t)$ [17][18][19]. (40) proves that G-R noise has a Lorentzian spectrum.

1.1.6 Flicker Noise

If a noise power spectral density is inversely proportional to frequency, this noise is referred to flicker noise or $1/f$ noise. Therefore, the current power spectral density for flicker noise can be expressed by

$$S_i(f) = C_0\frac{I^B}{f^A} \tag{41}$$

where C_0, A, and B are all constant coefficients. Generally, for $1/f$ noise, the frequency exponent A is between 0.8 and 1.2. This has been found in a great variety of electronic devices such as vacuum tubes, resistors, MOSFETs, and BJTs. Although all of these devices show $1/f$ noise, there is no evidence to indicate that a common physical mechanism is responsible and $1/f$ noise is still a mystery.

According to an extensive study on $1/f$ noise, two different fundamental models are generally used to explain the physics of $1/f$ noise, namely the mobility fluctuation model and the number fluctuation model.

For the mobility fluctuation model, the power spectral density of $1/f$ noise is given by the Hooge's empirical formula as

$$\frac{S_i(f)}{I^2} = \frac{S_\mu(f)}{\mu^2} = \frac{\alpha_H}{Nf} \tag{42}$$

where μ is the mobility, S_μ is the power spectral density for mobility, and α_H is the Hooge's parameter [20][21]. Although this model is extensively used, there is no evidence to show that the Hooge's parameter is a universal constant. Therefore, more work remains necessary to investigate the physics of the Hooge's parameter.

Generally, the physics of number fluctuation model is similar to that of G-R noise. In other words, the number fluctuation model predicts G-R noise with multiple life-time constants. Hence, one can develop (39) into

$$S_N(f) = 4 < \triangle N^2 > \int_0^\infty g(\tau)\frac{\tau}{1+\omega^2\tau^2}d\tau \tag{43}$$

where g_τ is the probability of a Lorentzian spectrum with a life-time τ defined by

$$\int_0^\infty g(\tau)d\tau = 1 \tag{44}$$

For the case of $1/f$ noise, g_τ may be given by

$$\begin{cases} g(\tau) = \frac{1}{\tau ln(\tau_1/\tau_0)} \quad (\tau_0 \leq \tau \leq \tau_1) \\ g(\tau) = 0 \quad (\tau < \tau_0 \ or \ \tau_1 < \tau) \end{cases} \tag{45}$$

Substituting (45) into (43) yields

$$S_N(f) = \frac{2 < \triangle N^2 >}{\pi f ln(\tau_1/\tau_0)}[tan^{-1}(\omega\tau_1) - tan^{-1}(\omega\tau_0)] \quad (\tau_0 \leq \tau \leq \tau_1) \tag{46}$$

which demonstrates $1/f$ dependence.

1.2 Development of Complementary SiGe HBTs

From a semiconductor manufacturing standpoint, Si is not considered as an excellent material for modern integrated circuits (IC), although it has achieved great success in the last half decade. The overwhelming dominance of silicon in semiconductor industry is the result of its numerous advantages, including an easily grown and high-quality dielectric material (SiO_2), excellent thermal and mechanical properties, an extremely high dynamic range for both n-type and p-type doping, and surprisingly large and defect-free single crystals [22].

Although Si is preferred in fabrication, it is not an ideal material for device designing, especially for RF and microwave circuit applications operating at significantly high frequencies. High-frequency circuit applications impose highly restrictive performance demands on the speed of a device, which is ultimately determined by how fast the carriers can be transported through the device. However, the maximum velocity of both electrons and holes in Si is normally restricted to 1×10^7 cm/s, and the mobility for these carriers in Si is relatively small. Therefore, the intrinsic low speed of Si-based devices limits their high frequency applications.

With the rapid emergence and development of the information age, especially for the many new Internet applications, the use of novel hardware in computers and communications systems requiring higher speed and lower cost is vital for the semiconductor industry. Since the development of Si technology becomes more and more difficult to meet these new requirements, a novel silicon-germanium (SiGe) heterojunction bipolar transistor (HBT) has been introduced commercially. Introducing Ge into Si, which uses bandgap engineering in the Si material system, greatly improves the speed of carriers in SiGe alloys. Since the lattice constant of Ge is larger than that of Si, the bandgap of Ge (0.66eV) is smaller than that of Si (1.12eV). Hence, strained SiGe alloys produce a bandgap shrinkage that reduces the density of states and increases the mobility of carriers. In addition, a carefully designed Ge profile can generate a large drift electric field in the neutral base, effectively decreasing the minority carrier transit time in the base.

1.2.1 SiGe HBT Technology

The basic idea of SiGe HBTs dates to the invention of BJTs in the 1950s [23]. The theoretical foundation of modern SiGe BiCMOS technology was developed by Herbert Kroemer, who postulated that the energy bandgap of a SiGe layer could be altered with alloy grading [24]. However, one of the most challenging tasks in the early development of SiGe HBTs was to fabricate a very thin, high-quality SiGe base layer while maintaining good control over the Ge fraction, boron doping, and layer thickness due to the 4.2 % difference between the lattice constants of Si and Ge. Thus, it has taken nearly thirty years to develop and build practical techniques for the commercial production of SiGe HBTs. In a number of growth techniques that have proven capable of fabricating device-quality SiGe films, the ultra-high vacuum/chemical vapor deposition (UHV/CVD) technique [25] and the atmospheric pressure chemical vapor deposition (APCVD) technique [26] have been found to be the best suited for building up-to-date commercial SiGe HBTs. The first functional SiGe HBT was demonstrated in 1987 [27]. Since then, SiGe HBT technology has become widely used as a practical circuit technology. Recently, SiGe HBTs with f_T up to 350 GHz have been demonstrated [28]. Hence, SiGe HBT technology is challenging the superiority of III-V HBT technology.

For SiGe HBTs, most of its improved performance metrics over Si BJTs, such as current gain (β), Early voltage (V_A), and transit times (τ_b and τ_e), come from the carefully designed bandgap incorporating Ge. A typical schematic base bandgap in a SiGe HBT with a linearly graded Ge profile is demonstrated in Figure 1, where E_{gb0} is the bandgap for Si material under low-doping, $\triangle E_{gb}^{app}$ is the bandgap narrowing induced by heavy doping, $\triangle E_{g,Ge}(x)$ is the Ge-induced bandgap

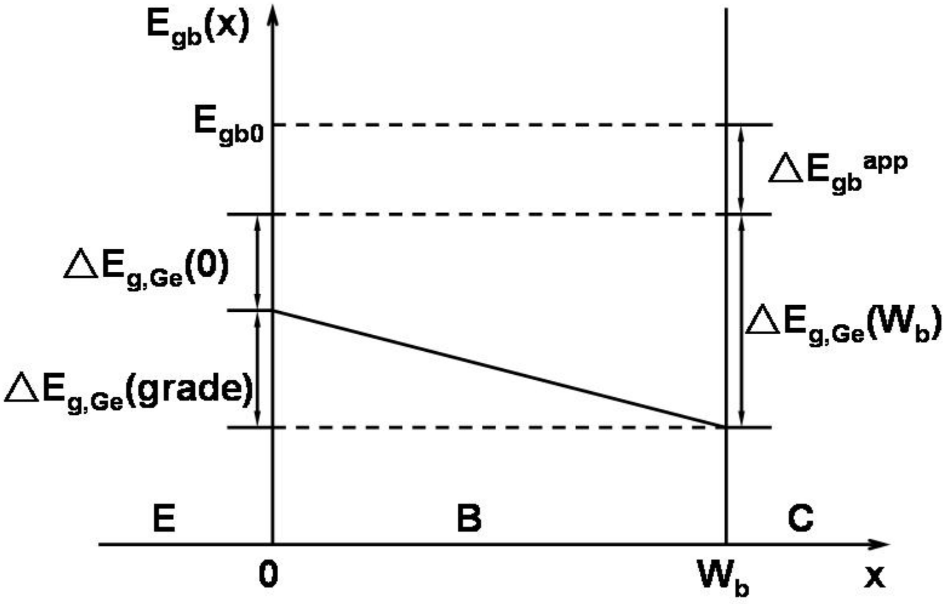

Figure 1: Schematic base bandgap in a SiGe HBT with a linearly graded Ge profile.

offset at position x, and $\triangle E_{g,Ge}(grade) = \triangle E_{g,Ge}(W_b) - \triangle E_{g,Ge}(0)$. Figure 1 clearly shows the bandgap shrinkage induced by the strained SiGe layer. The diminution of the bandgap causes a higher intrinsic carrier density in SiGe HBTs. Hence, the Gummel number in the base is reduced, which eventually gives a higher collector current and a higher β. In order to exhibit the improvement of SiGe HBTs, the current ratio between SiGe and Si is given by

$$\frac{\beta_{SiGe}}{\beta_{Si}}|_{V_{BE}} \approx \frac{\gamma\eta\triangle E_{g,Ge}(grade)exp[\triangle E_{g,Ge}(0)/kT]}{kT\{1 - exp[-\triangle E_{g,Ge}(grade)/kT]\}} \tag{47}$$

where γ is the effective density of states ratio between SiGe and Si, and η is the minority carrier diffusion ratio between SiGe and Si [22][29]. Since this factor is dominated by the term $exp[\triangle E_{g,Ge}(0)/kT]$, it is clear that introducing Ge into Si favors the current gain. In addition, this current gain factor also shows that SiGe HBT has a quasi-exponential increase in the cryogenic environment. The presence of a increasing Ge content on the collector side of the neutral base makes the neutral base significantly harder to deplete for a given applied C-B voltage. Hence, V_A is effectively raised. Following [22], the V_A ratio between SiGe and Si is expressed by

$$\frac{V_{A,SiGe}}{V_{A,Si}}|_{V_{BE}} \approx exp[\triangle E_{g,Ge}(grade)/kT]\{\frac{1 - exp[-\triangle E_{g,Ge}(grade)/kT]}{\triangle E_{g,Ge}(grade)/kT}\} \tag{48}$$

which also demonstrates a quasi-exponential increase in V_A with the Ge concentration gradient. The graded energy bandgap could generate a "quasi-electric" field to enhance the transport of charged carriers in the base and induce a higher cut-off frequency (f_T). According to this theory, a Ge concentration gradient across the base of a *npn* SiGe HBT with a lower Ge content at the emitter side can generate a corresponding quasi-electric field to aid electron transport across the base. The advantages of SiGe HBTs in high-frequency performance are represented by the enhancement in the base and emitter transit times. The transit time ratios of τ_b and τ_e are

$$\frac{\tau_{b,SiGe}}{\tau_{b,Si}} \approx \frac{2kT}{\eta \triangle E_{g,Ge}(grade)}\{1 - \frac{kT\{1 - exp[-\triangle E_{g,Ge}(grade)/kT]\}}{\triangle E_{g,Ge}(grage)}\} \tag{49}$$

and

$$\frac{\tau_{e,SiGe}}{\tau_{e,Si}} \approx \frac{kT\{1 - exp[-\triangle E_{g,Ge}(grade)/kT]\}}{\gamma \eta \triangle E_{g,Ge}(grade) exp[\triangle E_{g,Ge}(0)/kT]} \tag{50}$$

respectively. Both are favorably affected by either $\triangle E_{g,Ge}(grade)$ or $\triangle E_{g,Ge}(0)$. Besides those figures-of-merit, several other advantages of SiGe technology over the conventional Si technology are worth mentioning, including: 1) 100% compatible with existing Si technology, 2) low noise performance, and 3) capability of further performance enhancement via scaling.

Due to these significant improvements in performance over Si technology and comparatively lower manufacturing costs than III-V compound semiconductor transistors, SiGe HBTs have become a major challenger to III-V devices, which previously dominated the high-speed and high-frequency market. Furthermore, the SiGe HBT BiCMOS technology, which integrates SiGe HBTs with best-of-breed Si CMOS, naturally offers a better solution in emerging system-on-chip and system-on-package ICs than III-V compound transistors.

1.2.2 Complementary SiGe HBTs

In low-power and high-frequency analog blocks, the performance of complementary analog technology (*npn*+*pnp*) is known to be much better than that of *npn* only technology. Thus, the complementary technology is widely incorporated in analog circuits such as active loads, voltage and current sources, and push-pull drivers [30]. One of the key points in the complementary technology is to preserve the comparable performance between *npn* and *pnp* devices. Nevertheless, the frequency response of *npn* transistors is naturally better than that of *pnp* transistors. This is due to the fact that the electron mobility in the *p* type base of *npn* transistors is comparatively larger than the hole mobility in the *n* type base of *pnp* devices [31]. Hence, the performance enhancement in *pnp* transistors is very desirable.

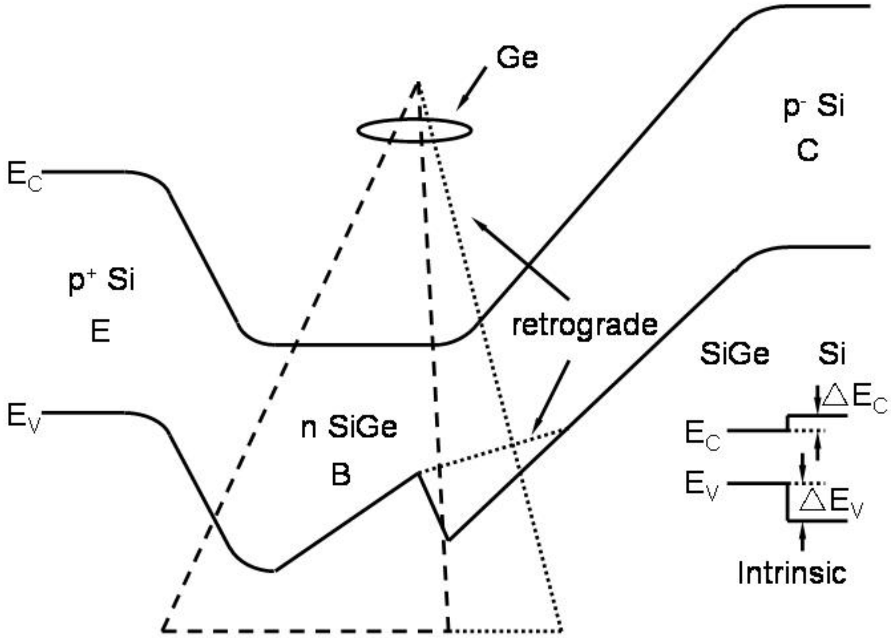

Figure 2: Energy band diagram for a *pnp* SiGe HBT with a linearly graded and a retrograded Ge profile.

The SiGe technology offers a novel solution to meet this requirement since the "quasi-electric" field generated by Ge content grading can accelerate the transport of minority charged carriers. Although the SiGe HBT technology has been developed for nearly thirty years, this has almost entirely focused on *npn* devices. The difficulty in dealing with *pnp* SiGe HBTs is mainly due to the fact that the band alignment is not as restrictive as it was originally assumed to be [22]. For a strained SiGe layer grown on a Si substrate, the offset in the valence band ($\triangle E_V$) is much larger than that in the conduction band ($\triangle E_C$), as shown in Figure 2 [22]. For a *npn* SiGe HBT, this valence band grading is eventually translated into shrinkage in the conduction band. Due to the small conduction band offset, there is no visible barrier in *npn* devices. For a *pnp* SiGe HBT, on the other hand, the large valence band offset directly induces a barrier at the collector side of the base, which produces a pileup of accumulated holes (Figure 2). Then, a retarding electric field in the base is built that compensates the drift field caused by the Ge grading, thereby significantly decreasing performances like current gain and f_T. This phenomenon indicates that designing *pnp* SiGe HBTs is inherently more challenging than designing *npn* SiGe HBTs.

A carefully designed Ge profile can dramatically reduce this intrinsic barrier in *pnp* SiGe HBTs. As shown in Figure 2, retrograding of the Ge profile edge further into the collector can effectively reduce the height of the barrier in *pnp* SiGe HBTs, thus producing significant performance enhancement for the *pnp* SiGe HBT. For example, the peak f_T of *pnp* SiGe HBTs is nearly twice that of *pnp* Si HBTs with equal doping [31]. However, the benefits of this type of retrograding generally come at the expense of the stability of the SiGe film, since the total amount of Ge is limited by the thermodynamic stability criterion [32][33]. When the SiGe layer is larger than the critical thickness, the strained SiGe film will relax and carry unwanted defects. Therefore, the trade-off between the peak Ge content and the Ge retrograde distance must be carefully designed.

Due to these difficulties, only very recently has the complementary SiGe HBT technology (*npn* + *pnp*) been introduced for advanced analog circuit applications [34]. Hence, in this field of analog applications, the complementary SiGe technology is still in its infancy. Another key to improving the performance match between the *npn* and *pnp* SiGe HBT (an obvious desire for analog IC design) lies in adjusting the controllable interfacial oxide (IFO) thickness, which achieves comparable current gains in these devices. Although introducing controllable IFO to complementary SiGe HBTs helps the performance match, it degrades the noise capability of these devices. Hence, the ability to characterize the LFN from IFO inside complementary SiGe HBTs becomes essential.

1.3 *LFN in SiGe HBTs*

For the application of SiGe HBTs in circuits, it is clear that LFN at low frequency is very important for applications such as direct conversion receivers (DCRs), as well as any base band applications. Moreover, even in high frequency applications, LFN still has a strong impact on the circuit performance because it can be up-converted via device non-linearities. For example, the phase noise in oscillators produced by the up-conversion of LFN is crucial to the device performance due to the nature of oscillators (high up-conversion gain and narrow bandwidth). Therefore, in-depth knowledge of the LFN of SiGe HBTs is very valuable for understanding the impact of device characteristics on circuits using those transistors.

The physics of LFN in SiGe HBTs generally shares many common features with that of Si BJTs, especially polysilicon emitter Si BJTs. In 1995, $1/f$ noise in an MBE-grown SiGe HBT, for instance, was found to have no significant difference between SiGe HBTs and Si BJTs [36]. The physical origin of this $1/f$ noise is still believed to come from number fluctuations at the pseudomorphic E-B hetero-interface. Since IFO is generally believed to be a major noise source, researchers tried completely removing this oxide layer in SiGe HBTs, which produced the record-low $1/f$ noise magnitude discovered in an MBE-grown SiGe HBT [37][38]. In 1999, a novel dual-channel correlation measurement was applied to SiGe HBTs, which revealed that the dominant noise source was located at the emitter side of the E-B junction [35]. Irradiation and stress experiments have also been used extensively to probe the noise mechanism in SiGe HBTs. For example, [39] and [40] demonstrated the degradation of $1/f$ noise in post-radiation and post-stress SiGe HBTs, and an investigation of the scaling of SiGe HBTs revealed that SiGe HBTs with small emitter areas have large $1/f$ noise variations [41]. In conclusion, early SiGe HBTs showed very impressive LFN characteristics.

However, due to the comparatively short history of SiGe HBTs, research on the LFN of SiGe HBTs still needs more attention and work, though some efforts have been devoted to improving the understanding of the noise mechanisms in SiGe HBTs. Furthermore, with the recent emergence of complementary SiGe HBTs, the LFN characteristics of those devices are not yet available. Hence, one of the major goals of this research is to investigate the physics and characteristics of $1/f$ noise in complementary SiGe HBTs, particularly the effects of IFO, temperature, and irradiation on $1/f$ noise.

1.4 LFN in Lateral BJTs

The rapid growth of the wireless communications market has resulted in an increasing demand for low-cost, low-noise, and low-power analog circuits such as RF/IF amplifiers, mixers, oscillators, and various power management circuits. BiCMOS technology is very promising for such applications because bipolar devices and CMOS devices can be selectively used to their greatest advantage to achieve optimal system performance.

It is well known that lateral BJTs are inherently available in the standard CMOS technology [42]-[48]. Compared with vertical BJTs (e.g., SiGe HBTs), these naturally-available lateral BJTs offer the opportunity to realize BiCMOS circuits in a very attractive way due to their avoidance of the complex processing steps necessary to add a vertical BJT [42][43]. In general, however, high performance lateral *npn* devices are still desirable in low-power and low-noise circuit applications. For example, due to the low-noise performance of lateral *pnp*, these devices are particularly suited for use in upper side current mirrors. In addition, lateral *pnp* can help increase the power efficiency in the output rail-to-rail buffer or the output stage of the amplifier. However, lateral BJTs also suffer from some intrinsic disadvantages, including enhanced substrate vertical current, poor isolation, poor off-state leakage, and low current gain, all of which significantly limit their usefulness for practical circuit applications [44][45]. Several attempts to build high-performance lateral BJTs using silicon-on-insulator (SOI) structures have been made [42][46][47]. Unfortunately, such approaches are incompatible with conventional bulk CMOS fabrication and are therefore inherently too expensive.

In light of this situation, enhancements in the performance of existing lateral *pnp* BJTs found in conventional BiCMOS processes are obviously very desirable. From a device design standpoint, the performance of these lateral devices can be improved by a number of possible optimization methods, such as adjusting the base width (W_B), emitter area (A_E), gate oxide thickness, and base doping. Therefore, the effects of these design approaches must be understood before the best practical lateral *pnp* BJT can be built.

In addition to investigating the impact of alternative designs on *dc* and *ac* performance, the LFN in lateral *pnp* BJTs is addressed in this study. This area has received very little attention to date. For the circuit applications of lateral BJTs, LFN, which sets the lowest detectable signal limit in a system, can be up-converted to high-frequencies, degrading the spectral purity of the system (i.e., phase noise). Therefore, accurate measurement and understanding of LFN are essential for such applications.

1.5 Scope of the Thesis

This thesis has three main contributions including: 1) characterizing the LFN of complementary SiGe HBTs, 2) characterizing the LFN of *npn* SiGe HBTs with different structure dimensions, 3) characterizing the LFN of lateral *pnp* BJTs. The emergence of complementary SiGe HBTs, which achieved a great success in analog circuits, was a milestone in the development of SiGe HBTs. However, due to their relatively short history, the characteristics of these devices were not fully understood. The LFN performance is one of these key characteristics since complementary SiGe HBTs target analog applications. In the investigation of the LFN in complementary SiGe HBTs, several vital questions were needed to be answered. For example, a record controllable ultra-thin IFO layer was employed to obtain the performance match between *npn* and *pnp* devices. Hence, investigating the effects of this IFO on the LFN of complementary SiGe HBTs was very important. SiGe HBTs showed a very promising potential in extreme environment such as outer space. Therefore, the LFN behavior in this environment with variable temperature and proton radiation needed to be carefully characterized. This thesis, for the first time, presented a comprehensive study on the LFN of SiGe HBTs including building physical models to explain the LFN phenomena, hence, initiated the study to answer those questions. The LFN of devices with different dimensions has been studied for decades. Most of these studies pointed out that the LFN was related to the emitter area. However, considering a significantly large lateral component in the base current, the universal dependence of LFN on the emitter area was questionable. This thesis presented the LFN data measured from *npn* devices with different structure dimensions and confirmed the possibility that LFN could be related to the emitter periphery. Lateral *pnp* BJTs are good compensation for SiGe HBTs in low-power and low-noise circuits due to their simplicity. However, the noise performance of lateral *pnp* BJTs was seldom addressed, especially for devices with different doping profiles. This thesis discussed the LFN performance of lateral *pnp* BJTs optimized by using different doping profiles.

Advanced bipolar technologies including SiGe HBT technology normally deploy IFO between the poly-silicon emitter and the mono-silicon emitter to improve device current gain. However, the $1/f$ noise characteristics of SiGe HBTs are degraded by this practice. Since the thickness of IFO for SiGe HBTs (<10 Å) is minimal, it is not easy to quantify the IFO thickness and the effects of IFO on the $1/f$ noise. For example, a transparency fluctuation model for the $1/f$ noise of poly-emitter BJTs proposed that the magnitude of the $1/f$ noise should be proportional to the cubic power of the IFO thickness [49][50][51]. However, due to the general lack of information about the IFO thickness, this model could not be verified by the measured noise data. With the development of high-resolution ellipsmetric microscopy, the technology for precisely estimating IFO thickness has now become practical. Hence, an analytical model based on the measured IFO thickness for SiGe HBTs with controllable IFO can be established.

The effect of temperature on the performance of SiGe HBTs is a very attractive research topic since bandgap engineering positively influences most of the characteristics of SiGe HBTs at low temperatures, which is seldom the case in Si BJTs. Although SiGe HBTs operate very efficiently in the cryogenic environment, the $1/f$ noise characteristics of these devices over the cryogenic temperature range are seldom addressed. Since SiGe HBTs are becoming more and more important in cryogenic systems such as high-sensitivity cooled detectors, space-born electronics, and superconductor hybrid circuits, an investigation of the temperature dependence of $1/f$ noise is essential for developing the SiGe HBT technology. Furthermore, commercial devices normally operate at temperatures between 0 °C and 80 °C. Therefore, characterizing the $1/f$ noise performance over this temperature range will also be essential to ensure the commercial success of SiGe HBTs. In addition, besides the impact of temperature on the application of SiGe HBTs, variable temperature measurements are efficient tools in probing the physical mechanism of $1/f$ noise. Therefore, an investigation of $1/f$ noise at variable temperatures is necessary to both assess the suitability of SiGe HBTs in variable temperature environments and the physics of $1/f$ noise.

The radiation tolerance of electronic devices is a key factor for the spaceborne communications systems used in satellites, space shuttles, and space stations, due to the possible ionization and displacement damage caused by the high energy particles present in a space environment. Among these particles, protons, which carry an electronic charge and have a mass, are one of the most dangerous. Therefore, measuring and understanding the proton radiation response of LFN is very important for the spaceborne application of SiGe HBTs. In addition, proton radiation is useful in manipulating the traps inside transistors. Hence, radiation experiments can be used to probe the physical noise sources and test the reliability of SiGe HBTs.

Geometric scaling is a very efficient approach for improving the performance of SiGe HBTs because it does not need a change in expensive fabrication processes such as doping and the Ge mole profile. However, aggressive scaling often introduces some unexpected results, including extra leakage, die-to-die variation, and low yield. The LFN of SiGe HBTs is also greatly affected by geometric scaling since the trap distribution is not uniform in small devices. Furthermore, since the spacer oxide is normally considered an important noise source, the $1/f$ noise measured from devices with different ratios between the emitter perimeter and the emitter area can be used to clarify to what extent the spacer oxide affects the overall $1/f$ noise of SiGe HBTs.

Although the circuit model for the $1/f$ noise of BJTs is embedded in industrial standard simulation tools (e.g. SPICE), the physical mechanism for LFN, especially for $1/f$ noise, still remains unclear. Understanding noise physics and building physical models for LFN is a useful way to minimize noise and improve the device performance in circuit applications. For complementary SiGe HBTs, physical models can be used to identify the difference between *npn* and *pnp* devices. Hence, it can improve the performance match for the complementary technology.

Improving the current gain for lateral BJTs can be achieved by optimizing the base doping profile. Although the base doping can be used to manipulate the current gain, the effects of base doping on LFN are still not clear. Furthermore, lateral BJTs have a different current direction from conventional BJTs as the carrier flows along the surface of the gate oxide. In this case, it is important to know whether the gate oxide affects LFN or not. In addition, IFO, which is normally buried in vertical devices, does not exist in lateral BJTs. Therefore, performing LFN measurements on lateral BJTs is likely to expose a different mechanism for LFN.

Given the above considerations, the objective of the thesis was to characterize LFN in SiGe HBTs, investigate LFN physical mechanisms, and examine the characteristics of LFN in lateral

BJTs.

CHAPTER II

TECHNIQUES FOR LFN MEASUREMENTS ON BJTS

2.1 Introduction

LFN generally has different magnitudes spread over a large frequency range. Therefore, the LFN measurements, in contrast to regular DC and AC measurements, must record the power spectrum density of the noise. Since the measured power spectral densities are made up of a combination of all the noise generated from all kinds of components inside the devices, such as resistances, junctions and oxide surfaces, the use of techniques designed to extract the dominant components are vitally necessary. In this work, a novel base-collector dual channel power spectral density measurement technique was employed to probe dominant noise sources inside BJTs. This technique measures the LFN from both the base and the collector. At the same time, it also calculates the coherence between these two channels, which can be used to probe physical noise sources. Furthermore, this technique proves that there is only one dominant noise source associated with the base current in the device used in this work. This chapter discusses the details of this dual-channel technique and how to extract and identify the dominant noise source.

2.2 Measurement Setup

The block diagram of the base-collector dual channel LFN measurement system is shown in Figure 3. The system includes four major components: 1) the device under test (DUT), 2) biasing circuits, 3) pre-amplifiers, and 4) the dynamic signal analyzer. The DUTs were all probed on wafer, and tested in the common-emitter mode. Biasing circuits used two 12 V lead acid batteries (Panasonic Model NO. LC-RD 1217P) to supply biasing currents. The biasing condition were adjusted by two 100 KΩ wire wound potentiometer through stepping motors controlled by a PC. Noise signals were measured from metal film resistors R_S and R_L in series with the base and the collector, respectively. Here, R_S was 1 MΩ, and R_L was 1 KΩ. The pre-amplifiers (model 5113) operated in the differential mode, with a gain of 500 and a frequency roll-off to 6 dB between 0.03 Hz and 300 KHz. The dynamic signal analyzer (Agilent 35670A) recorded and analyzed the amplified noise signals, covering the frequency range from 1 Hz to 52 KHz. The noise power spectral density was measured in the units of V^2/Hz.

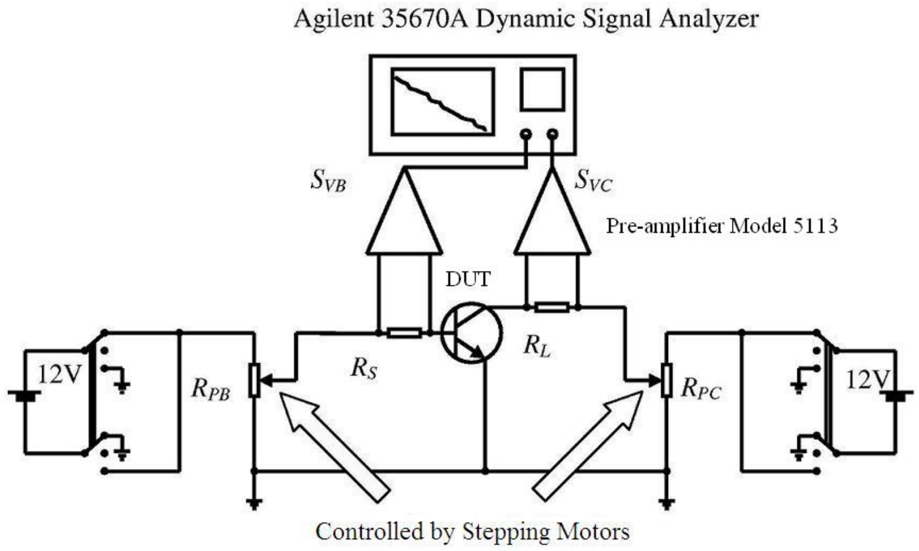
Agilent 35670A Dynamic Signal Analyzer
S_{VB}
S_{VC}
Pre-amplifier Model 5113
DUT
12V
R_{PB}
R_S
R_L
R_{PC}
12V
Controlled by Stepping Motors

Figure 3: Block diagram for the base-collector dual channel power spectral density measurement system.

2.3 Hybrid-π Model for LFN Measurement

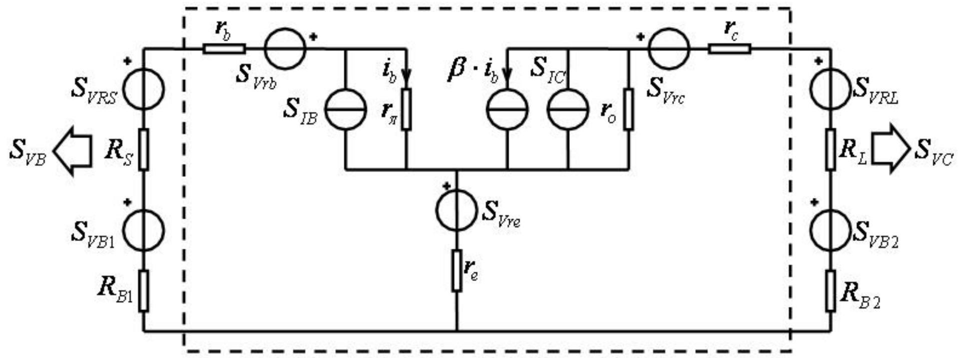
r_b
S_{Vrb}
i_b
$\beta \cdot i_b$
S_{IC}
S_{Vrc}
r_c
S_{VRS}
S_{IB}
r_π
r_o
S_{VRL}
S_{VB}
R_S
R_L
S_{VC}
S_{Vre}
S_{VB1}
S_{VB2}
r_e
R_{B1}
R_{B2}

Figure 4: Hybrid-π model for the base-collector dual-channel LFN measurement system.

The hybrid-π Model is one of the most popular circuit models for analyzing LFN. Figure 4 shows the specific hybrid-π model used in this dual-channel noise measurement system, along with the major noise sources. β is the dynamic current gain, which is given by

$$\beta \approx \frac{\triangle I_C}{\triangle I_B} \tag{51}$$

r_o and r_π are the dynamic input and output resistances of the internal transistor, respectively. r_π is given by

$$r_\pi \approx \frac{\triangle V_{BE}}{\triangle I_B} \tag{52}$$

r_b, r_c and r_e are the internal base, collector, and emitter resistances with their associated voltage noise sources S_{Vrb}, S_{Vrc} and S_{Vre}, respectively. R_{B1} and R_{B2} are the equivalent output resistances associated with the potentiometer for the base and the collector, respectively. The voltage noise sources associated with R_{B1}, R_{B2}, R_S and R_L are shown in the hybrid-π model as S_{VB1}, S_{VB2}, S_{VRS}, and S_{VRL}, respectively. S_{IB} and S_{IBC} represent equivalent current noise sources in the E-B and B-C junctions, respectively. According to those noise sources, the voltage noise spectral densities S_{VB} and S_{VC} measured from R_S and R_L, respectively, are defined by

$$S_{VB} = (\frac{Z'}{Z})^2 S_{VRS} + (\frac{R_S}{Z})^2 [S_{Vrb} + S_{Vre} + S_{VB1} + (r_\pi + r_e\beta)^2 S_{IB} + r_e^2 S_{IC}] \tag{53}$$

and

$$\begin{aligned} S_{VC} &= S_{VRL} + (\frac{R_L}{Z})^2 [\beta^2 (S_{VRS} + S_{VB1} + S_{Vrb} + S_{Vre}) \\ &+ \beta^2 (R_S + R_{B1} + r_b + r_e)^2 S_{IB} + (R_S + R_{B1} + r_b + r_\pi + r_e)^2 S_{IC}] \end{aligned} \tag{54}$$

with Z=R_S+R_{B1}+r_π+r_b+(1+β)r_e, and Z'=Z-R_S [35][52][53]. The cross power spectral density S_{VBC} between S_{VB} and S_{VC} is

$$\begin{aligned} S_{VBC} &\approx -\frac{R_S R_L}{Z^2}[\beta(r_\pi + r_e\beta)(R_S + R_{B1} + r_b + r_e)S_{IB} \\ &+ r_e(R_S + R_{B1} + r_b + r_e + r_\pi)S_{IC}] \end{aligned} \tag{55}$$

Hence, the coherence γ_{coh}^2 between S_{VB} and S_{VC} is given by

$$\begin{aligned} \gamma_{coh}^2 &= \frac{|S_{VBC}|^2}{S_{VB}S_{VC}} \\ &\approx \frac{[\beta(r_\pi + r_e\beta)(R_S + R_{B1} + r_b + r_e)S_{IB} + r_e(R_S + R_{B1} + r_b + r_e + r_\pi)S_{IC}]^2}{[\beta^2(R_S + R_{B1} + r_b + r_e)^2 S_{IB} + (R_S + R_{B1} + r_b + r_e + r_\pi)^2 S_{IC}]} \\ &\times \frac{1}{[(r_\pi + r_e\beta)^2 S_{IB} + r_e^2 S_{IC}]} \end{aligned} \tag{56}$$

Here, S_{Vrb}, S_{Vrc}, S_{Vre}, S_{VRS}, S_{VRL}, S_{VB1}, and S_{VB2} are neglected since all are dominated by thermal noise, which is much lower than either $1/f$ noise or generation-recombination noise.

A typical set of S_{VB} and S_{VC} measured from a *pnp* SiGe HBT at I_B=8.0 μm with A_E =0.4×6.4 μm^2 is shown in Figure 5. If one assumes that S_{IC} is the dominant noise source, then

$$\begin{aligned} \frac{S_{VC}}{S_{VB}} &\approx \frac{\frac{R_L^2}{Z^2}(R_S + R_{B1} + r_b + r_e + r_\pi)^2 S_{IC}}{\frac{R_S^2}{Z^2} r_e^2 S_{IC}} \\ &= \frac{R_L^2(R_S + R_{B1} + r_b + r_e + r_\pi)^2}{R_S^2 r_e^2} \end{aligned} \tag{57}$$

At I_B=8.0 μA, r_π ≈3.1 KΩ. Assuming $r_e \leq$10 Ω, S_{VC}/S_{VB} should be close to 10^4. However, the measured data, according to Figure 5, shows S_{VC}/S_{VB} to be less than 100, which contradicts the assumption. Therefore, S_{IC} cannot be the dominant noise source for the device. Applying the same technique, one can also exclude the possibility of S_{Vrb}, S_{Vrc}, S_{Vre}, S_{VRS}, S_{VRL}, S_{VB1}, and S_{VB2} being the dominant noise source, leaving S_{IB} as the only candidate. Therefore, (53) and (54) can be rewritten to

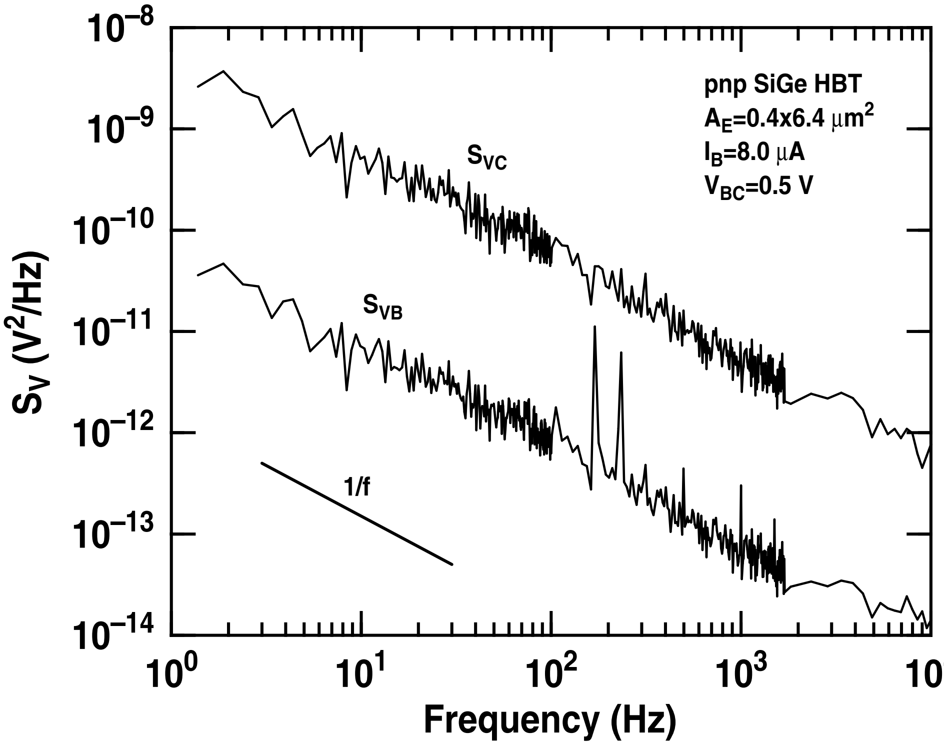

Figure 5: Typical power spectral densities S_{VB} and S_{VC} measured from the dual-channel system for a *pnp* SiGe HBT at I_B=8.0 μm with A_E=0.4×6.4μm^2.

$$S_{VB} \approx (\frac{R_S r_\pi}{R_S + r_\pi})^2 S_{IB} \tag{58}$$

and

$$S_{VC} \approx (\frac{R_L R_S \beta}{R_S + r_\pi})^2 S_{IB} \tag{59}$$

According to (58) and (59) and using the data shown in Figure 5, S_{IB} was extracted from both S_{VB} and S_{VC} and is exhibited in Figure 6. The S_{IB} drawn from the two different channels are almost the same, which proves that the proposed hybrid-π model can effectively predict the dominant noise source S_{IB}. Figure 6 also shows γ^2_{coh} measured from the dual-channel system. Since γ^2_{coh} is very close to unity, this indicates that there is only one dominant LFN source in the device. Hence, employing this dual-channel LFN system can be used to show that S_{IB} is the only dominant noise source in SiGe HBTs.

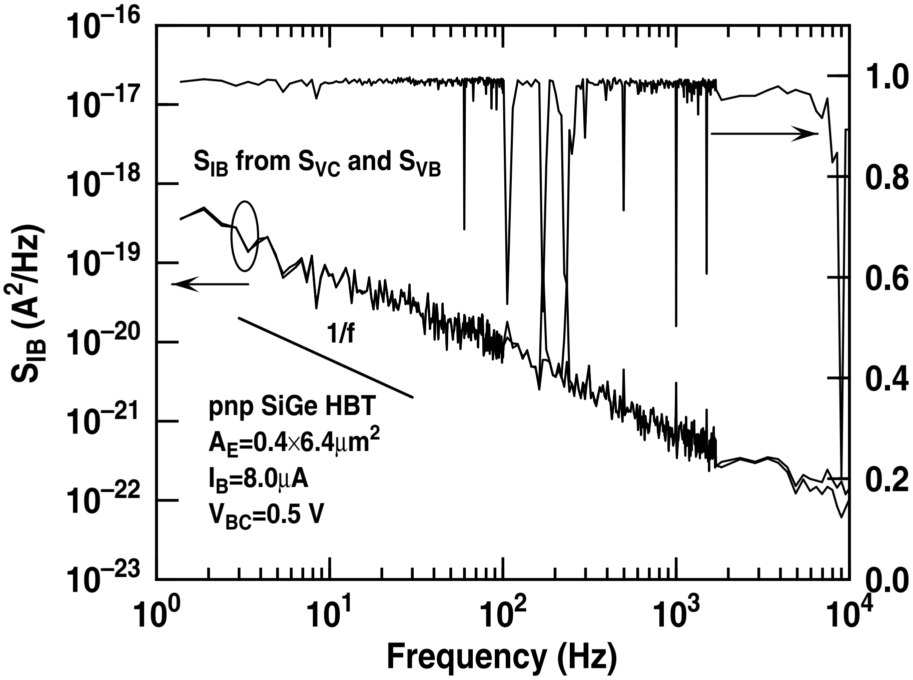

Figure 6: Extracted power spectral densities S_{IB} from S_{VB} and S_{VC} and measured coherence data for a *pnp* SiGe HBT at I_B=8.0 μm with A_E=0.4×6.4 μm^2.

CHAPTER III

PHYSICAL LFN MODELS FOR SIGE HBTS

3.1 Introduction

Physical LFN models are vital in understanding the origin of LFN. Hence, it would be very helpful to be able to predict the LFN of devices in future generations. Currently, establishing models to explain the physical origin and location of LFN is a very active research area. As discussed in [54], several models for the physics of LFN in bipolar transistors have been proposed and discussed. All of those models agree that LFN in bipolar transistors is due to fluctuations in the base current, so physical models generally focus on explaining the physics of S_{IB}. In addition, the IFO between the polysilicon emitter and the monosilicon emitter and the spacer oxide covering the E-B junction are believed to be the most likely sources of the LFN for SiGe HBTs. Therefore, models predicting S_{IB} from those oxide layers are receiving a great deal of attention.

In order to analyze noise sources in the IFO, the base current must first be examined. The base current is dominated by the minority carrier current I tunneling through the IFO. I is modulated by the interface potential ψ_{mono} at the IFO-monosilicon interface due to thermionic emission [55]-[59], which is given by

$$I = I_0 exp(-\frac{q\psi_{mono}}{kT}) \tag{60}$$

where I_0 is a constant (refer to Appendix B). In this case, LFN is believed to originate from the surface potential variation $\triangle\psi_{mono}$, which is expressed as

$$\triangle\psi_{mono} = \frac{\triangle Q_{mono}}{AC_{mo}} \tag{61}$$

where $\triangle Q_{mono}$ is the surface charge variation on the monosilicon side, A is the effective IFO area, and C_{mo} is the IFO-monosilicon interfacial capacitance per unit area. Accordingly, the variation of I is defined by

$$\frac{\triangle I}{I} = \frac{\partial ln(I)}{\partial \psi_{mono}} \triangle \psi_{mono} = \frac{q}{kT} \cdot \frac{\triangle Q_{mono}}{AC_{mo}} \tag{62}$$

Hence, one can define the power spectral density for the fluctuation of I as

$$S_I = C \cdot \frac{q^2 I^2}{k^2 T^2} \cdot \frac{S_{Q_{mo}}}{AC_{mo}^2} \tag{63}$$

where $S_{Q_{mo}}$ is the carrier fluctuation per unit area and C is a unitless ideality factor close to 0.5 [60]. $S_{Q_{mo}}$ is generated by two different physical mechanisms and can be expressed as,

$$S_{Q_{mo}} = S_{IFO} + S_{interf} \tag{64}$$

Here, S_{IFO} is the fluctuation generated by traps inside the IFO, and S_{interf} originates from states at the monosilicon-IFO interface.

The noise from the spacer oxide covering the E-B junction is associated with the surface recombination current I_S, which is modulated by the surface potential ψ_S at the emitter-base space charge region as

$$I_S = I_{S0} exp(-\frac{q\psi_S}{kT}) \tag{65}$$

where I_{S0} is the surface recombination saturation current. ψ_S is modulated by the variation in the surface charge Q_S at the $Si - SiO_2$ interface. Therefore, the variation of ψ_S is given by

$$\triangle \psi_S = \frac{\triangle Q_S}{A_S C_S} \tag{66}$$

with A_S being the effective surface area of the space charge region and C_S the effective surface capacitance per unit area. Applying the same approach used in (62), the power spectral density for the fluctuation of I_S is

$$S_{IS} = \frac{q^2}{k^2T^2} \cdot \frac{S_{QS}}{A_S C_S^2} I_S^2 \tag{67}$$

where S_{QS} is the surface charge spectral density per unit area.

3.2 Carrier Random-Walk Model

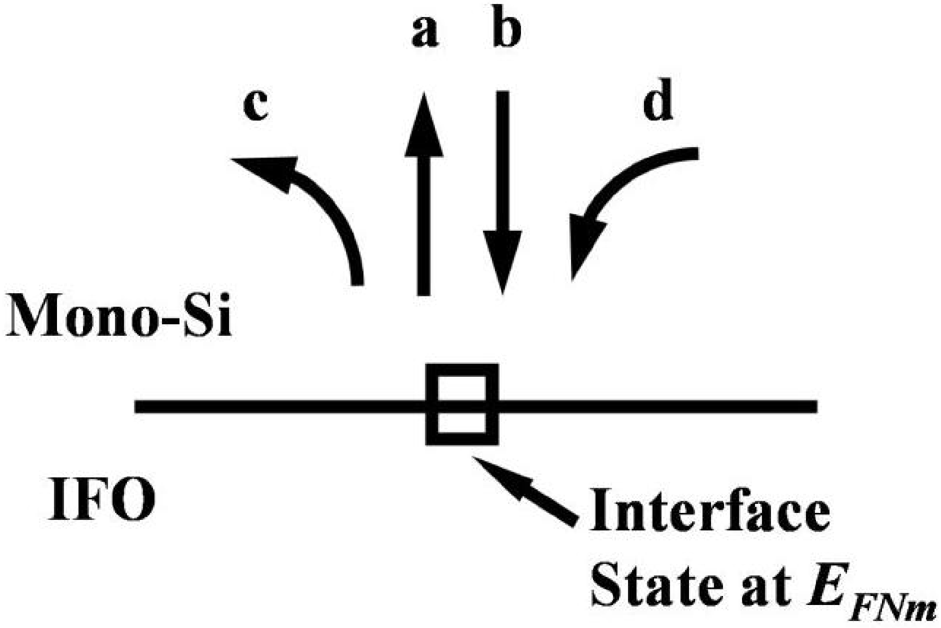

Figure 7: Schematic of carrier transport processes of the random-walk model for IFO interface states in a *pnp* device.

Figure 7 illustrates four possible carrier transition processes for an interface state. Processes (a) and (b) show the carrier trapping-detrapping transition between an interface state with energy close to the majority carrier quasi-Fermi level E_{FNm} and the conduction/valence band through the SRH process. However, unlike in the tunneling model, some of the carriers may be re-captured by other interface states when they are released (process (c)). The empty interface state will also be able to capture carriers from other interface states (process (d)). The overall trapping/detrapping process resembles that of a carrier, which is first trapped by an interface state, and then randomly emitted and released for a relatively long time (as opposed to the short-fast state time constant) by other interface states until it is de-trapped back into the conduction/valence band. If the time constant τ for this type of random-walk process is large enough, and the probability distribution of τ displays a $1/\tau$ behavior between τ_{max} and τ_{min}, LFN will demonstrate a $1/f$ spectrum in a frequency range from $1/\tau_{max}$ to $1/\tau_{min}$.

According to [61], S_{interf} for the random-walk model is

$$S_{interf} = q^2 \int f(E_t)[1 - f(E_t)] D_{it} dE_t \cdot \int_{\tau_{min}}^{\tau_{max}} g(\tau) \frac{4\tau}{1 + \omega^2 \tau^2} d\tau \tag{68}$$

where $f(E_t)$ is the trap Fermi-Dirac distribution, E_t is the trap energy, D_{it} is the interface state density with units of (cm^{-2}·eV^{-1}), and $g(\tau)$ is the probability distribution of the time constant τ, given by

$$g(\tau) = \frac{\sqrt{\sigma}}{2\pi l \tau} \approx \frac{0.1}{\tau} \tag{69}$$

where σ is the trap capture cross-section and l is the shortest possible mean free path length [61]. Considering that $f(E_t)[1 - f(E_t)]$ can be modeled as a quasi-delta function around the trap quasi-Fermi level, which is very close to E_{FNm} in this case (refer to Appendix A). (68) can be evaluated to give

$$S_{interf} = \frac{0.2q^2}{\pi f} kT D_{it}(E_{FNm}) [\arctan(2\pi f \tau_{max}) - \arctan(2\pi f \tau_{min})] \tag{70}$$

If 1/($2\pi\tau_{max}$)<<1 Hz and 1/($2\pi\tau_{min}$)>>100 kHz, $\arctan(2\pi f \tau_{max})) - \arctan(2\pi f \tau_{min}) \approx \pi/2$ within a frequency range from 1 Hz to 100 kHz. Hence, Eq.(70) can be rewritten as

$$S_{interf} = \frac{0.1q^2}{f} kT D_{it}(E_{FNm}) \tag{71}$$

3.3 Two-Step Tunneling Model

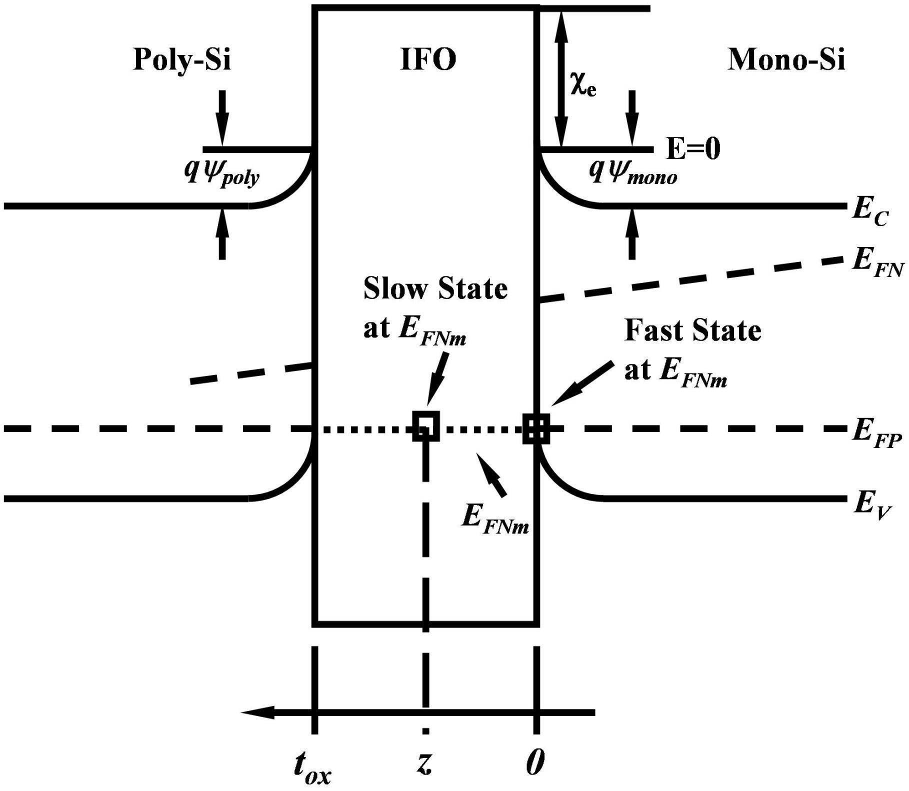

Poly-Si
IFO
Mono-Si
χ_e
$q\psi_{poly}$
$q\psi_{mono}$
E=0
E_C
E_{FN}
Slow State at E_{FNm}
Fast State at E_{FNm}
E_{FP}
E_{FNm}
E_V
t_{ox}
z
0

Figure 8: Schematic of IFO for two-step tunneling model for a *pnp* device.

As shown in Fig. 8, if the life-time for the fast state is negligible, S_{IFO} can be assumed to originate only from slow states inside the IFO. The life-time constant for carriers tunneling from the mono-silicon emitter side is then given by,

$$\tau_{mono} = \tau_0 \cdot exp(\frac{z}{\lambda}) \tag{72}$$

where z is the tunneling distance (the distance between the interface and the active trap in the IFO) and λ is the effective tunneling distance (refer to Appendix A).

The power spectral density for the fluctuation of trapped carriers in a volume element inside IFO is given by [63]

$$\triangle S_{IFO} = 4kTq^2 N_{IFO}(E_t, z, t_{ox}) f(E_t)[1 - f(E_t)] \frac{\tau_{mono}}{1 + \omega^2 \tau_{mono}^2} \triangle z \tag{73}$$

where $N_{IFO}(E_t, z, t_{ox})$ is the trap density in the IFO as a function of trap energy E_t, z, and t_{ox}. Since $f(E_t)[1 - f(E_t)]$ behaves like a quasi-delta function around the majority carrier quasi-Fermi level at the monosilicon-IFO interface E_{FNm} [62], it can be shown that

$$S_{IFO} = kTq^2 \int_0^{t_{ox}} N_{IFO}(E_{FNm}, z, t_{ox}) \frac{\tau_{mono}}{1 + \omega^2 \tau_{mono}^2} dz \tag{74}$$

It should be noted that traps occupied by carriers from the polysilicon side can be neglected since the quasi-Fermi levels between the two sides of the IFO are not equal.

3.4 Tunneling-Assisted Trapping Model

The "tunneling-assisted trapping" model predicts a non-quadratic dependence of S_{IB} on the base current, which can be used to explain the linear dependence of $1/f$ noise on I_B for post-radiation *npn* devices [64][65]. This model assumes that $1/f$ noise originates from dynamic carrier trapping and detrapping processes by slow states inside the spacer oxide covering the emitter-base junction.

As for the power spectral density for trapped carriers in a volume element discussed in the two-step tunneling model, the spectral density S_{QS} in the element tunneling depth $\triangle z'$ is [66]

$$\triangle S_{QS} = 4kTq^2 N_T(E_t) f'(E_t)[1 - f'(E_t)] \frac{\tau(z')}{1 + \omega^2 \tau^2(z')} \triangle z' \tag{75}$$

with $N_T(E_t)$ being the trap density in the spacer oxide in units of $(cm^{-3} \cdot eV^{-1})$, $f'(E_t)$ the trap occupancy distribution, and $\tau(z')$ the trapping time constant for a slow state trap at position z' inside the spacer oxide, which is given in

$$\tau(z') = \tau_S exp(z'/\lambda') \tag{76}$$

where τ_S is the mean time constant and λ' is the effective attenuation tunneling distance for the trapping-detrapping process in the spacer oxide. Integrating (75) over the whole energy region, the entire oxide charge spectral density S_{QS} is expressed by

$$S_{QS} = \int kTq^2 N'_T \frac{\tau(z')}{1+\omega^2\tau^2(z')} dz = kTq^2 N'_T \lambda' \frac{\pi/2 - tan^{-1}(\omega\tau_s)}{\omega} \tag{77}$$

where N'_T is the effective trap density in the spacer oxide, and $f'(E_t)(1-f'(E_t))$ is evaluated as a quasi-delta function at the mid-gap E_i and is close to 1/4. Note that $f'(E_t)$ in this case is close but not exactly equal to the Fermi-Dirac distribution because the electron and hole densities around the center of the space charge region are comparable. Hence, if one treats $f'(E_t)[1-f'(E_t)]$ as a quasi-delta function in the same way as $f(E_t)[1-f(E_t)]$ in the last section, N'_T is slightly larger than $N_T(E_i)$. Since τ_S is on the order of μs, $tan^{-1}(\omega\tau_S)$ is negligible up to $f = 100$ KHz. Therefore, S_{QS} becomes

$$S_{QS} \approx \frac{kTq^2 N'_T \lambda'}{4f} \tag{78}$$

Substituting Eq.(78) into Eq.(67) and assuming the surface recombination fluctuation is the dominant noise source ($S_{IB} \approx S_{IS}$), S_{IB} can be given by

$$S_{IB} = \frac{q^4 N'_T \lambda'}{4kTA_S C_S^2 f} I_S^2 \tag{79}$$

Since the base current I_B is composed of a diffusion current and the surface recombination current, it can be defined by

$$I_B = I_D + I_S \approx I_{B0} \cdot exp(\frac{qV_{BE}}{kT}) + I_{S0} \cdot exp(\frac{qV_{BE}}{m_S kT}) \tag{80}$$

where I_D is the diffusion current, and I_{B0} and I_{S0} are the diffusion and surface saturation current, respectively. Therefore, base current fluctuations can be expressed as

$$S_{IB} = \frac{q^4 N_T' \lambda}{kTA_S C_S^2 f} \cdot \frac{I_{S0}^2}{I_{B0}^{2/m_S}} I_B^{2/m_S}. \tag{81}$$

Since the surface area of the emitter-base space charge region A_S is proportional to the emitter periphery, the tunneling-assisted trapping model predicts that S_{IB} will be inversely proportional to the emitter perimeter (P_E).

CHAPTER IV

LFN IN COMPLEMENTARY SIGE HBTS

4.1 Introduction

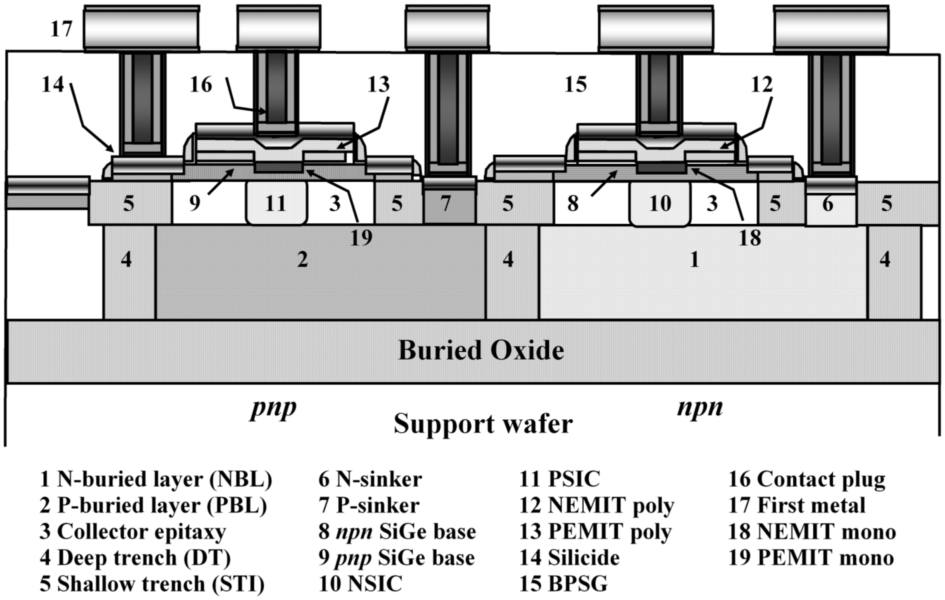
17
14
16
13
15
12
5
9
11
3
5
7
5
8
10
3
5
6
5
19
18
4
2
4
1
4
Buried Oxide
pnp
Support wafer
npn
1 N-buried layer (NBL)
2 P-buried layer (PBL)
3 Collector epitaxy
4 Deep trench (DT)
5 Shallow trench (STI)
6 N-sinker
7 P-sinker
8 npn SiGe base
9 pnp SiGe base
10 NSIC
11 PSIC
12 NEMIT poly
13 PEMIT poly
14 Silicide
15 BPSG
16 Contact plug
17 First metal
18 NEMIT mono
19 PEMIT mono

Figure 9: Schematic cross section of *npn*+*pnp* SiGe complementary HBTs (SIC is the self-aligned collector implant, BPSG is the boro-phospho-silicate glass).

The complementary SiGe HBT used in this investigation is manufactured by Texas Instruments and has dual depositions of SiGe epitaxy (boron doped for the *npn* and arsenic doped for the *pnp*) [34]. Shallow trench, deep trench, and buried oxide layer were employed to isolate the *npn* and *pnp* devices. For the standard process, the *npn* and *pnp* devices have open-base collector-emitter breakdown voltages (BV_{CEO}) of 7.0 V and 6.0 V and V_A of 150 V and 100 V, respectively, and a peak f_T of about 20 GHz. The devices used in this investigation have four different emitter areas (A_E): 0.4×0.8 μm^2, 0.4×1.6 μm^2, 0.4×3.2 μm^2, and 0.4×6.4 μm^2. With the development of high-resolution ellipsmetric microscopy, the technology for precisely estimating IFO thickness has now

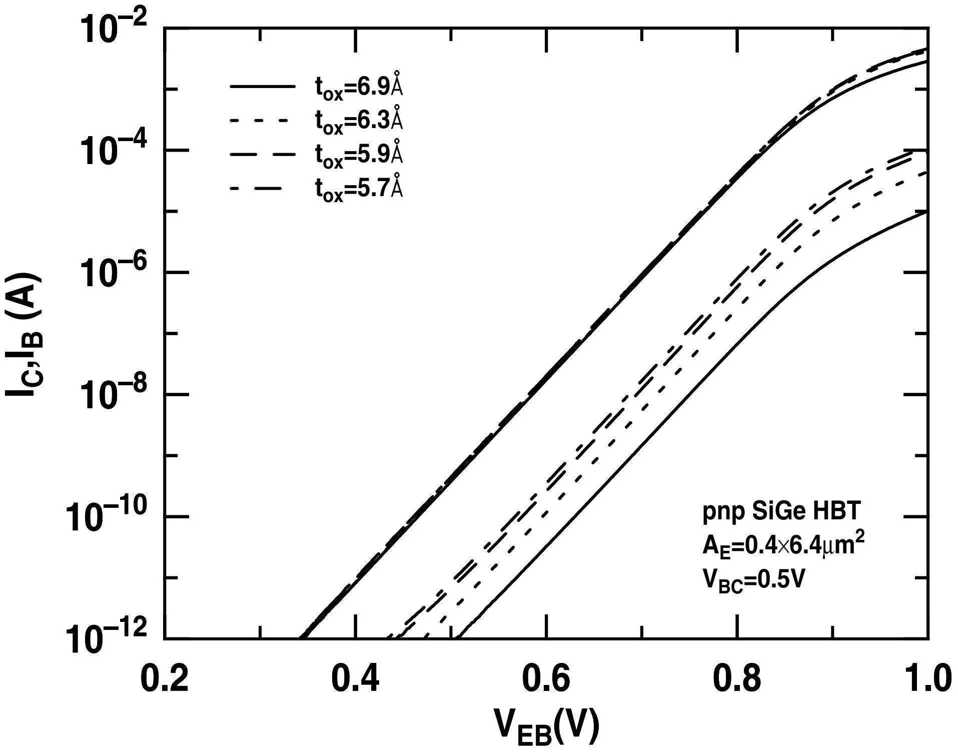

Figure 10: Gummel characteristics for *pnp* SiGe HBTs with different IFO thicknesses, but with the same emitter area A_E=0.4×6.4 μm^2, at V_{BC}=0.5 V.

become practical. Hence, a controllable IFO layer (<10 Å) was buried between the polysilicon-emitter contact and the mono-silicon emitter (Figure 9). The *pnp* transistors used here had four different IFO thicknesses t_{ox}, which are estimated to be 5.7 Å, 5.9 Å, 6.3 Å, and 6.9 Å. The *npn* devices had only two IFO thicknesses: 5.2 Å and 5.9 Å. The *pnp* devices with t_{ox}=5.9 Å and *npn* devices with t_{ox}=5.2 Å were found to offer the best performance matching. Gummel plots of *pnp* transistors with varying IFO thicknesses are shown in Figure 10. The base current (I_B) decreased significantly with slight increases in the IFO thickness, indicating suppressed minority carrier diffusion by the IFO layer. The collector currents (I_C), however, remained identical for different IFO thicknesses due to the unchanged base Gummel number and the high emitter doping level. In the high collector current region, the I_C for an IFO thickness of 6.9 Å was slightly smaller than that for other IFO thicknesses, indicating a slight degradation in the emitter resistance (R_E) of this device. The abrupt increase of R_E at t_{ox}=6.9 Å indicates that the majority carrier current is impeded by

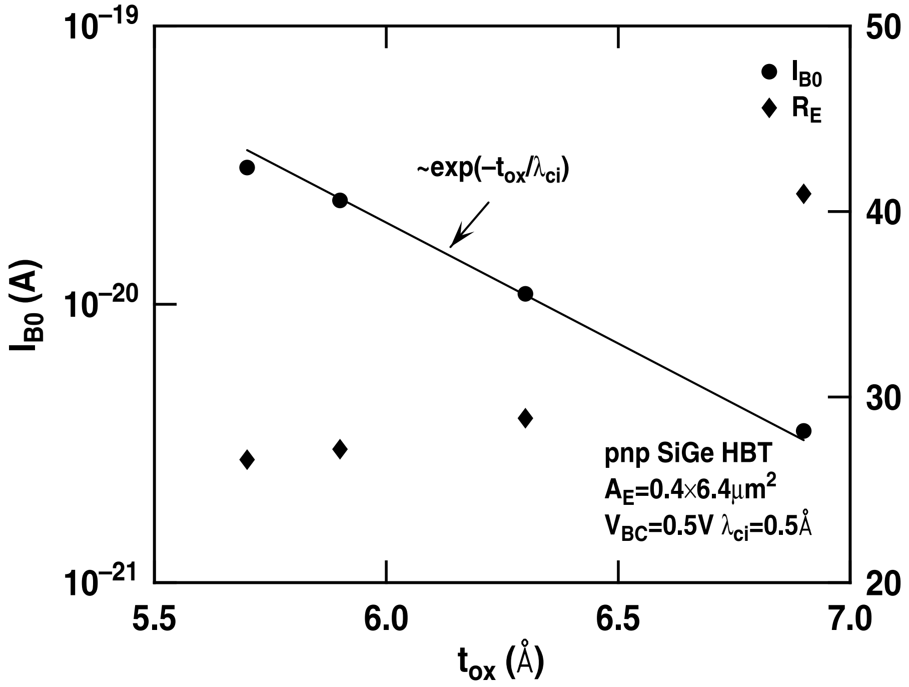

Figure 11: The base saturation current and the emitter resistance as a function of IFO thickness. Data measured from *pnp* SiGe HBTs with A_E=0.4×6.4 μm^2, and V_{BC}=0.5 V. λ_{ci} is the characteristic IFO thickness for I_B.

the IFO [67]. The base saturation current (I_{B0}) shown in Figure 11 was extracted from the transistor's ideal region of operation, and shows a clear exponential dependence on IFO thickness as $I_{B0} \propto \exp(-t_{ox}/\lambda_{ci})$, where λ_{ci} is the characteristic IFO thickness for I_B, consistent with a direct tunneling transport mechanism [68]. The emitter resistance as a function of IFO thickness is illustrated in Figure 11. As the same fabrication process was used for all these devices, this increase in R_E is, therefore, logically the result of the increase in the IFO thickness.

Although the use of an IFO may enhance the performance match for complementary SiGe HBTs, the LFN of SiGe HBTs degrades as the IFO thickness increases. Therefore, characterizing the effect of the IFO on the LFN of SiGe HBTs is essential in order to improve device performance.

4.2 Effects of the IFO on LFN

The LFN of complementary SiGe HBTs was measured over the range from I_B=0.2 μA to I_B=4.0 μA. Figure 12 shows typical noise spectra measured from three *pnp* transistors with the same emitter area but different IFO thicknesses, ranging from 5.9 Å to 6.9 Å, at I_B=1.0 μA. The

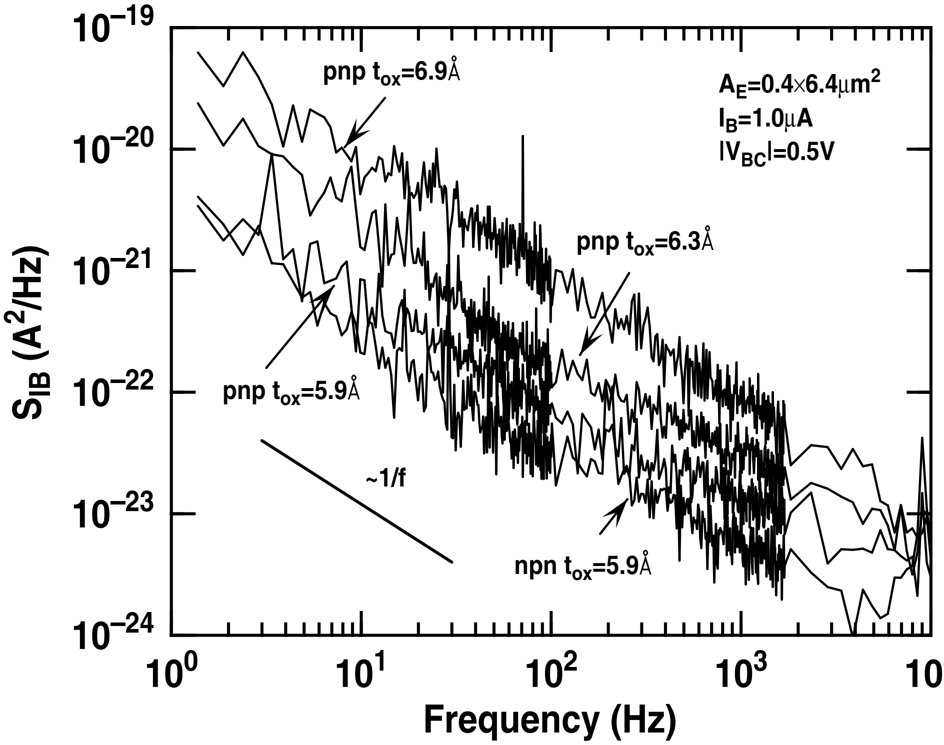

Figure 12: Noise spectra for *pnp* SiGe HBTs with the same A_E=0.4×6.4 μm^2 but different IFO thicknesses at I_B=1.0 μA and V_{BC}=0.5 V.

magnitude of the $1/f$ noise at a fixed frequency significantly increases with the IFO thickness. LFN for the *npn* device with an IFO thickness of 5.9 Å is also shown for comparison in Figure 12, which confirms that *pnp* devices have higher $1/f$ noise than *npn* devices. The $1/f$ noise of *pnp* devices with all kinds of IFO thicknesses obeys a classical quadratic dependence on I_B over the measured base current range (Figure 13) [69]. At all biasing conditions, $1/f$ noise has a uniform exponential dependence on the IFO thickness, as shown in Figure 14, with $A_E \times S_{IB}/I_B^2 \propto \exp(t_{ox}/\lambda_{cn})$ where λ_{cn} is the characteristic IFO thickness for LFN models. This phenomenon indicates that the dominant component of LFN comes from the IFO itself. The $1/f$ noise of *npn* devices in this technology is roughly comparable to that in other reported *npn* SiGe HBTs. For example, as reported in [70], the $1/f$ noise of a device with A_E=0.82×3.22 μm^2 and without an intentional IFO layer is nearly four times larger than that for the *npn* devices with A_E=0.4×6.4 μm^2 and t_{ox}=5.9 Å used in this study at I_B=7.92 μA. The $1/f$ noise of this device is close to that of the polysilicon emitter BJT with A_E=0.5×5.0 μm^2 and an oxygen dose of 2.6×10^{15} cm^{-2} reported in [71], which has a λ_{cn} $\approx$1.9

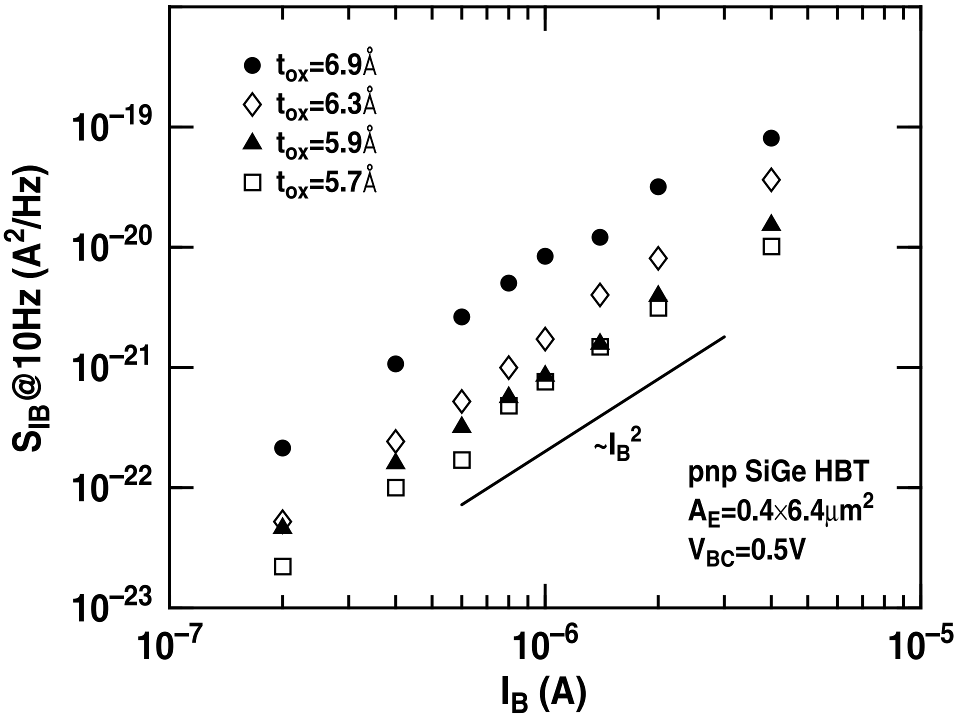

Figure 13: The dependence of LFN on I_B for *pnp* SiGe HBTs with different IFO thicknesses but the same A_E=0.4×6.4 μm^2, at V_{BC}=0.5 V and f=10 Hz.

Å.

Table 1 lists the extracted SPICE parameters K_F and A_F for devices with A_E=0.4×6.4 μm^2, which are defined by

$$S_{IB} = K_F \frac{I_B^{A_F}}{f}. \tag{82}$$

Note that the $1/f$ noise of these devices still obeys a classical $1/A_E$ dependence [1].

4.3 *Effects of Temperature on LFN*

LFN measurements at temperatures ranging from 473 K down to 94 K were used to probe the underlying noise physics of complementary SiGe HBTs. Figure 15 shows the typical Gummel characteristics for both *npn* and *pnp* transistors at 94 K, 298 K, and 473 K. Although complementary SiGe HBTs exhibit ideal characteristics at 298 K and 473 K, the non-ideal base current attributable

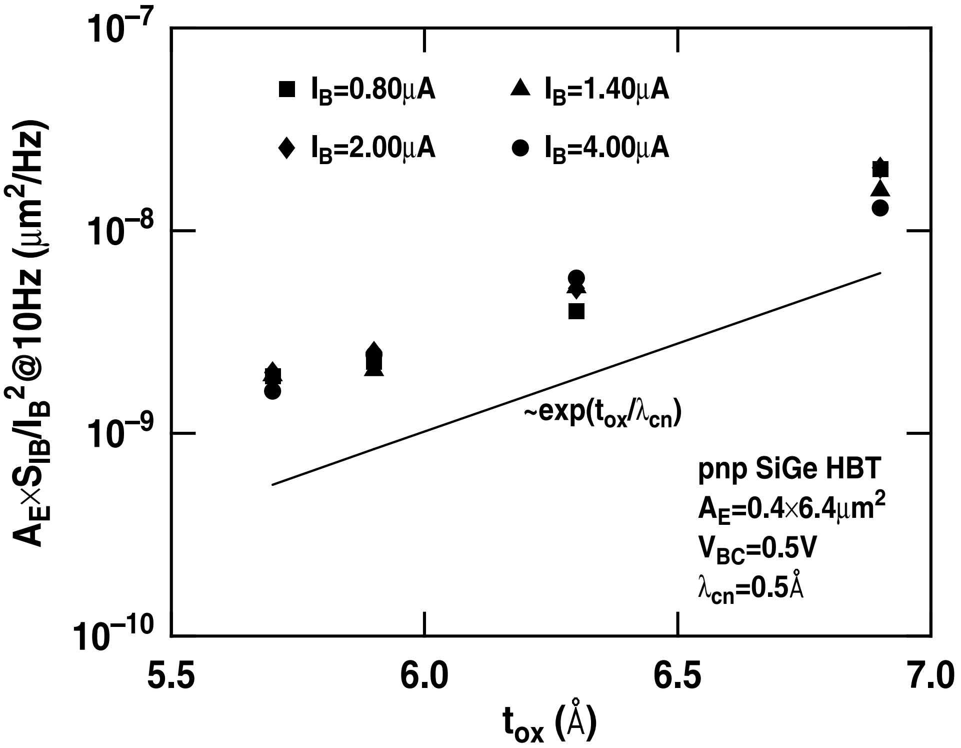

Figure 14: The dependence of LFN on the IFO thickness at different I_B. The spectral densities are for *pnp* SiGe HBTs with A_E=0.4×6.4 μm^2, with V_{BC}=0.5 V and f=10 Hz. λ_{cn} is the characteristic IFO thickness for LFN.

to field enhanced and trap-assisted tunneling becomes non-negligible in both *npn* and *pnp* at 94 K due to a significant reduction in the diffusive base current with cooling. In addition, at 94 K, an abrupt jump at $V_{EB} \approx 1.2$ V due to heterojunction barrier effects occurs in the high injection region of the *pnp* base current [22]. However, no such phenomenon is observed in *npn* transistors. Figure 16 demonstrates the noise spectra measured at I_B=1.0 μA for both *npn* and *pnp* transistors at 94 K, 298 K and 473 K, respectively. At different temperatures, the noise spectra still maintain excellent $1/f$ shapes, and this is the case for all biasing conditions and all temperatures. *pnp* transistors are more sensitive to temperature than *npn* transistors. The quadratic dependence of $1/f$ noise on I_B is still clearly present over the temperature range 94 K - 473 K for both types of devices (Figure 17). Figure 18 shows S_{IB}/I_B^2 at 10 Hz for complementary transistors as a function of temperature. Both types of devices remain quite ideal in their noise behavior, displaying near $1/T$ dependence across a wide temperature range, which is clearly beneficial for precision analog circuit design. *pnp* transistors exhibit a slightly stronger dependence on temperature than *npn* transistors,

Table 1: SPICE noise parameters K_F and A_F and $D_{it}(E_{FNm})/C^2_{mo}$ (refer to Section 4.6) for *npn*+*pnp* SiGe complementary HBTs with A_E=0.4×6.4 μm^2.

	t_{ox} (Å)	K_F	A_F	$D_{it}(E_{FNm})/C^2_{mo}$ ($\mathrm{cm}^2 \cdot F^{-2} \cdot \mathrm{eV}^{-1}$)
pnp	5.7	2.45×10^{-8}	2.09	3.4×10^{21}
	5.9	4.36×10^{-9}	1.95	4.9×10^{21}
	6.3	2.73×10^{-7}	2.20	9.0×10^{21}
	6.9	6.64×10^{-8}	2.00	3.6×10^{22}
npn	5.2	1.48×10^{-9}	2.04	4.4×10^{20}
	5.9	1.49×10^{-10}	1.73	3.9×10^{21}

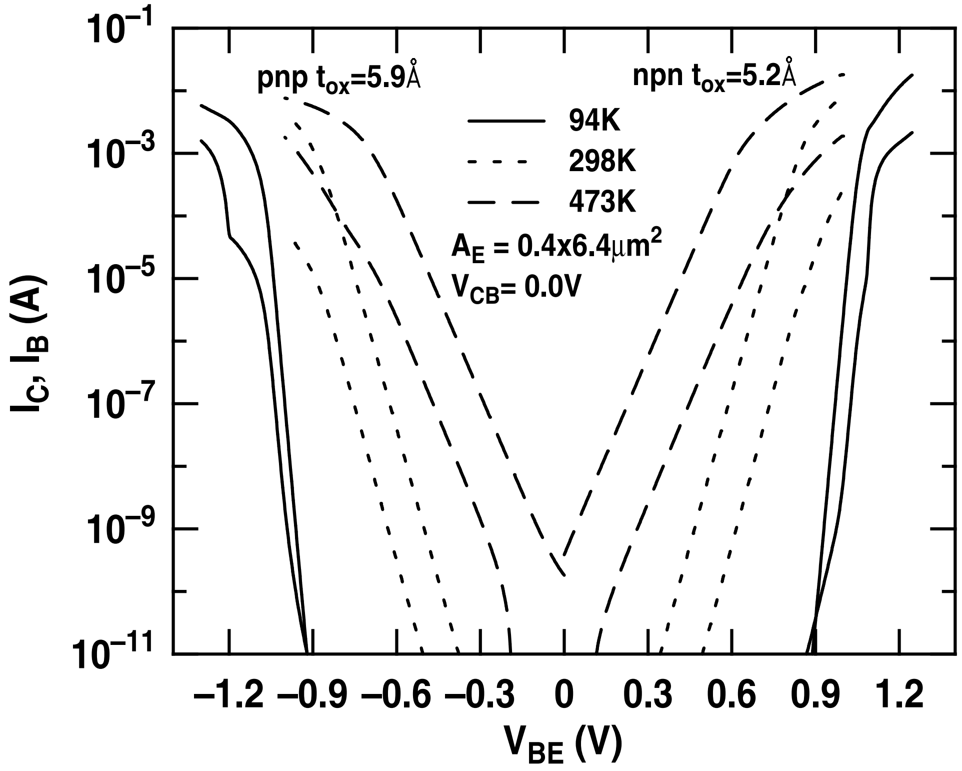

Figure 15: Gummel characteristics for *npn* and *pnp* SiGe HBTs with A_E=0.4×6.4 μm^2 and V_{BC}=0.0 V at different temperatures.

but in general, the observed temperature dependence for both types is relatively weak.

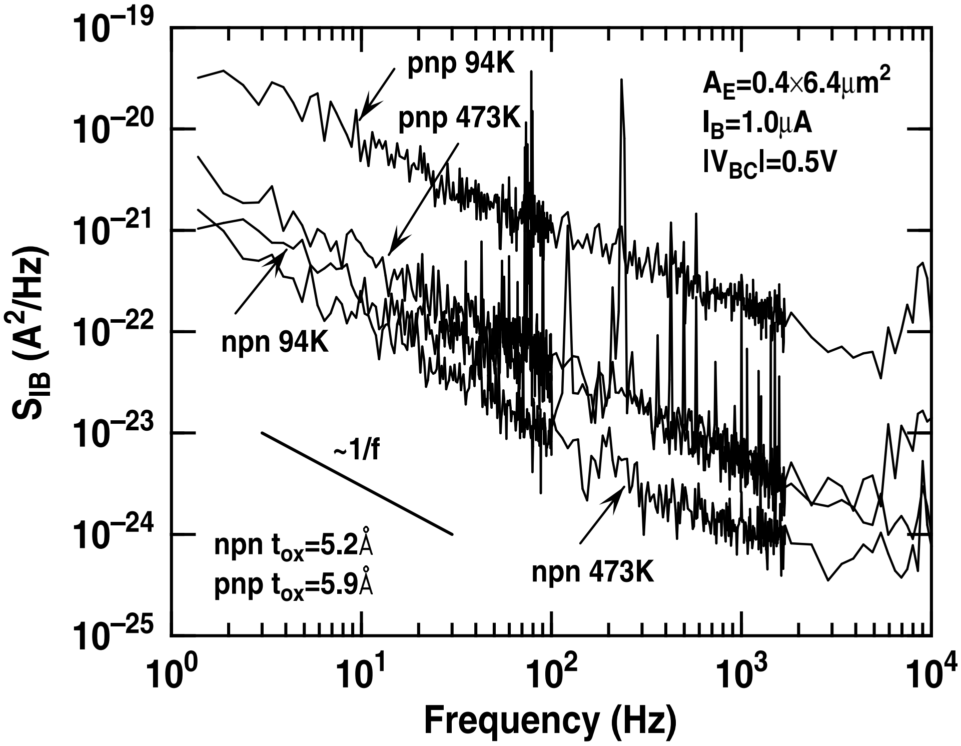

Figure 16: Typical noise spectra for *npn* and *pnp* SiGe HBTs with A_E=0.4×6.4 μm^2, I_B=1.0 μA and $|V_{BC}|$=0.5 V at different temperatures.

4.4 Effects of Proton Radiation on LFN

Samples were irradiated with 63.3 MeV protons at the Crocker Nuclear Laboratory at the University of California at Davis. Proton fluxes in radiation experiments from 10^6 to 10^{11} $p/cm^2/s$ can be achieved in the beam current range from about 5 pA to 50 nA. Details of the dosimetry system, which has an accuracy of up to about 10 %, are described in [72] and [73]. The measured equivalent gamma doses at proton fluences of 1.0 × 10^{12} and 5.0 × 10^{13} p/cm^2 were approximately 135 and 6,759 krad(Si), respectively.

Figure 19 demonstrates the radiation response of the Gummel characteristics for both device types as a function of proton fluence. The non-ideal base current component increased with increasing fluence, as expected, indicating that radiation-induced G/R traps were added to the device. Figures 20-22 show the current gain and the normalized I_B change for both *npn* and *pnp* SiGe HBTs in both the forward and inverse modes (emitter-base base terminals swapped) as a function of proton fluence. Interestingly, the *pnp* SiGe HBTs generally showed significantly better radiation tolerance

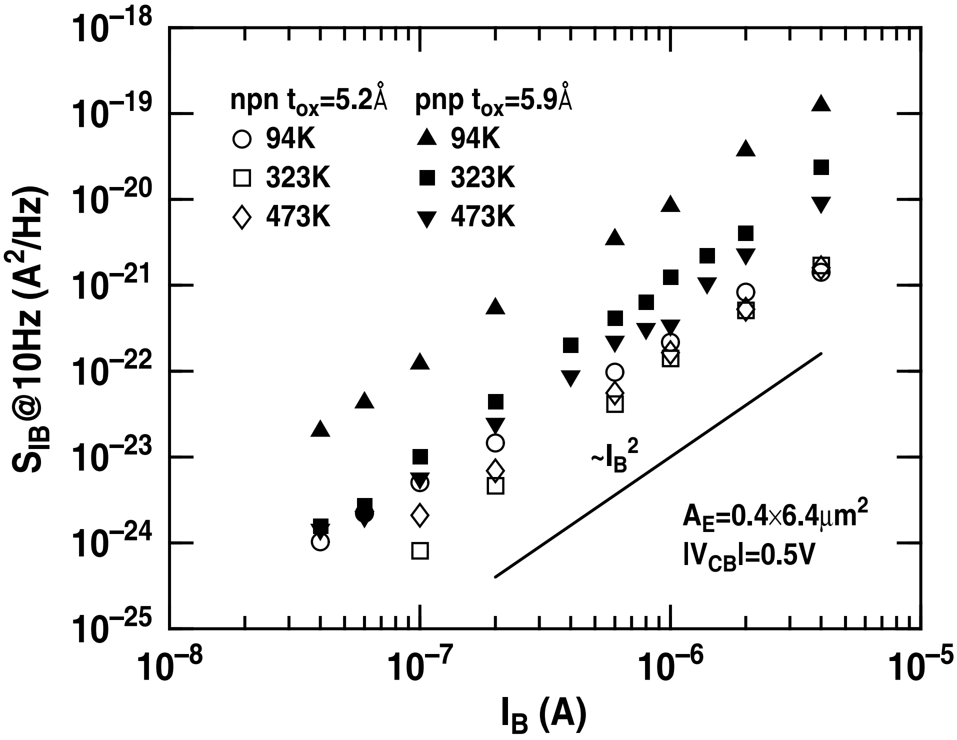

Figure 17: The noise magnitude dependence of *npn* and *pnp* SiGe HBTs with A_E=0.4×6.4 μm^2 and $|V_{BC}|$=0.5 V on I_B at different temperatures.

than *npn* SiGe HBTs, particularly in the inverse mode, although clearly there is a strong dependence on device geometry. This suggests that the damage thresholds for the two device types are fundamentally different, despite the near-identical processing associated with the damage-sensitive regions (i.e., the emitter-base spacer oxide and the shallow trench edge). Significant spontaneous self-annealing at room temperature over a span of about 6 weeks was also consistently observed .

For pre-irradiated devices, the noise spectrum was $1/f$ type in the frequency domain, generally similar to that observed in conventional Si BJTs [74] (Figure 23), with S_{IB} exhibiting an I_B^2 dependence and inverse proportionality to A_E (Figure 24).

All the spectra show clear $1/f$ dependence (e.g., Figure 23) over the base current range from $I_B = 0.1\mu$A to $I_B = 8.0\mu$A and increase with I_B. To avoid small size effects [41], the investigation here focused on the largest device, with A_E=$0.4 \times 6.4\mu$m^2. For the pre-radiation case, the $1/f$ noise of *npn* transistors was consistently smaller than that of *pnp* transistors (Figure 25 and Figure 26).

Interestingly, the post-irradiated devices again demonstrated very different behavior for *npn* and

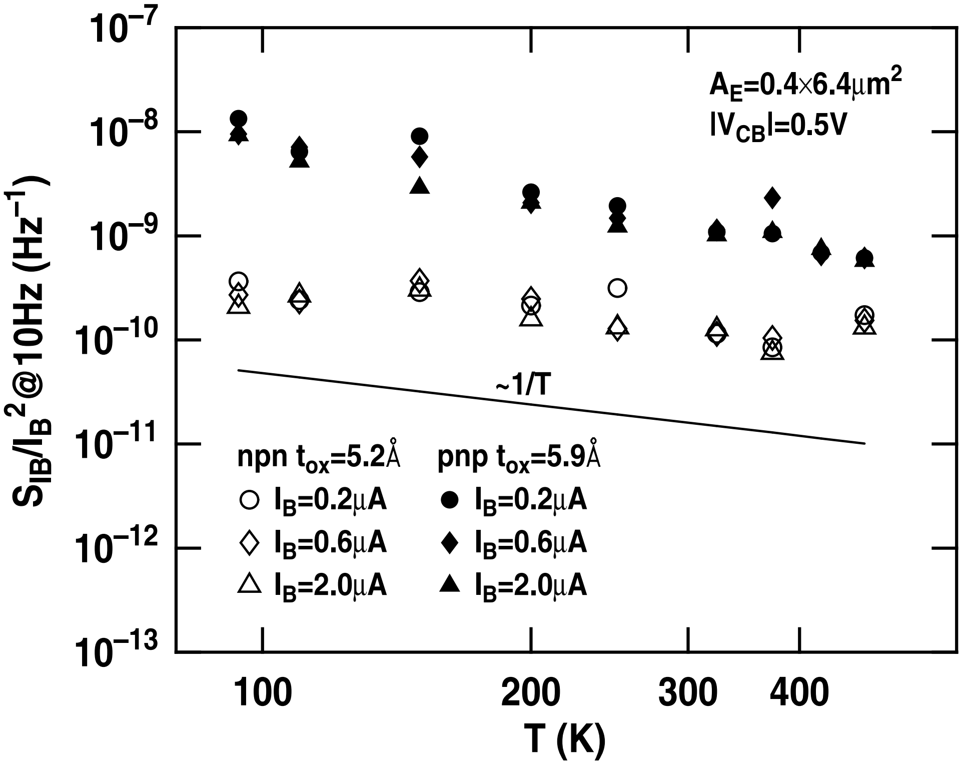

Figure 18: The LFN of *npn* and *pnp* SiGe HBTs as a function of temperature at different base currents with A_E=0.4×6.4 μm^2, $|V_{BC}|$=0.5 V, and f=10 Hz.

pnp SiGe HBTs, as shown in Figure 25 and Figure 26. For *pnp* transistors, the $1/f$ noise remained nearly unchanged up to a proton fluence of 5.0 × 10^{13} p/cm^2, while for *npn* transistors, the magnitude of the $1/f$ noise increased significantly after irradiation. This difference in noise response to radiation occurs in spite of the similar response in the *npn* and *pnp* Gummel characteristics at the same proton dose. Furthermore, for *npn* devices operating at low I_B (I_B<0.8 μA), the $1/f$ noise changed from a quadratic dependence to a near linear dependence on I_B after radiation, although it remained an I_B^2 dependence at higher bias levels. No such behavior was found in the *pnp* transistors.

A comparison of S_{IB} at 10 Hz for devices with different *npn* IFO layers is shown in Figure 27. For pre-radiation SiGe HBTs, the *npn* device with t_{ox} = 5.9Å had a larger $1/f$ noise magnitude, indicating that LFN is mainly caused by the IFO. Note, however, that the *npn* device with t_{ox} = 5.9Å also showed the same anomalous I_B dependence at low I_B as that found in the device with t_{ox} = 5.2Å, suggesting a fundamentally different noise physics between *npn* and *pnp* SiGe HBTs that is independent of emitter interface preparation.

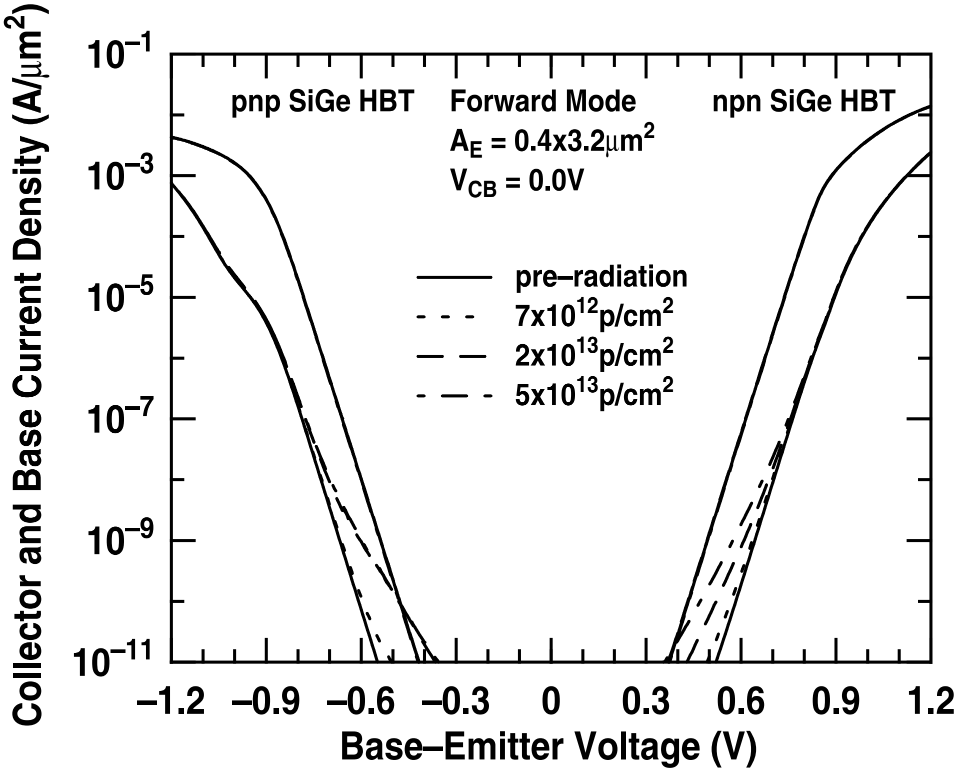

Figure 19: Gummel characteristics of pre- and post-irradiated complementary SiGe HBTs with A_E=0.4×3.2 μm^2 at V_{CB}=0.0 V.

4.5 Effects of Geometric Scaling on LFN

A geometrical emitter area scaling effect for LFN was found in *npn* SiGe HBTs and polysilicon emitter BJTs [41][75]. In this study, small-size effects on both *npn* and *pnp* SiGe HBTs were investigated, the first time such a study has been reported for *pnp* SiGe HBTs. Figure 28 demonstrates the typical noise spectra of *npn* and *pnp* devices with the same emitter area (0.4×0.8 μm^2). Although one of the *npn* SiGe HBTs shows an ideal $1/f$ noise spectrum, the other shows a dominant Lorentzian spectrum. The *pnp* devices present a very statistically reproducible $1/f$ noise spectrum, suggesting a reduced small-size effect.

Based on the standard deviation formula, a noise variation coefficient δ is given by

$$\delta = \frac{1}{n_f} \sum_{f=1Hz}^{100Hz} \frac{1}{|<log[S_{IB}(f)\cdot f]>|} \sqrt{\frac{1}{N_s-1} \sum_{i=1}^{N_s} \{log[S_{IB,i}(f)\cdot f] - <log[S_{IB}(f)\cdot f]>\}^2} \tag{83}$$

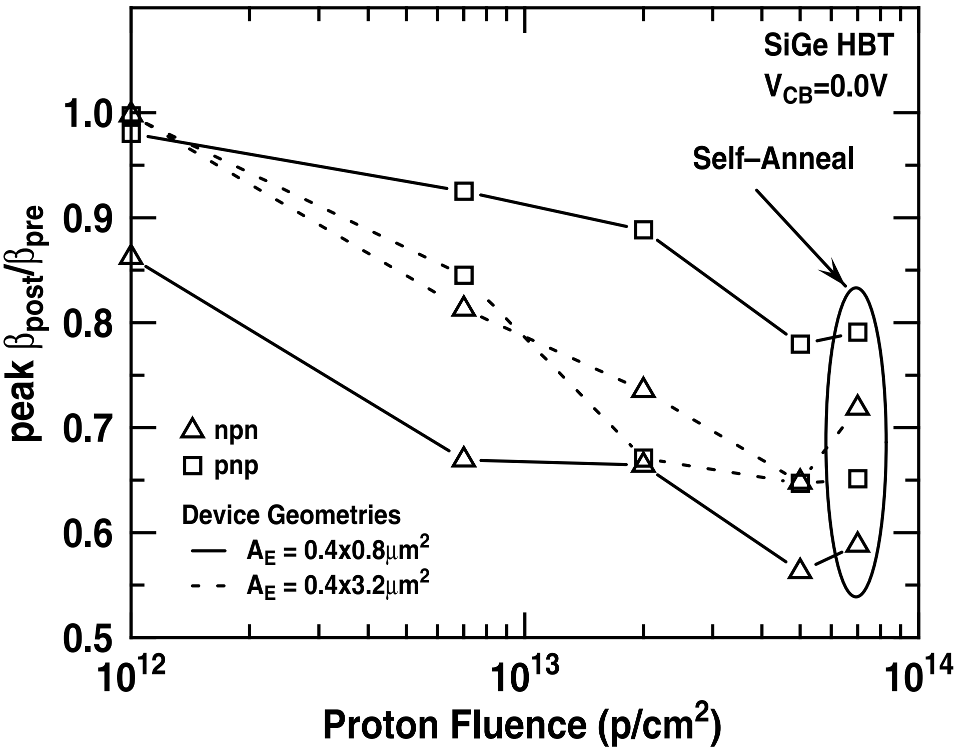

Figure 20: Current gain degradation of complementary SiGe HBTs with A_E=0.4×0.8 μm^2 and A_E=0.4×3.2 μm^2 at V_{CB}=0.0 V.

where

$$< log[S_{IB}(f) \cdot f] >= \frac{1}{N_s} \sum_{i=1}^{N_s} log[S_{IB,i}(f) \cdot f] \tag{84}$$

and n_f is the total number of sample frequencies between 1 Hz and 100 Hz (e.g., if there are three sample frequencies, such as f=1 Hz, 50 Hz, and 100 Hz, n_f=3), and i indicates the ith sample out of the total number of samples N_s. Figure 29 shows δ as a function of A_E. Each point in Figure 29 represents δ calculated from seven samples (N_s=7). For this specific process, the *npn* devices generally had a higher variance than *pnp* devices, and δ decreased with A_E increasing. This phenomenon is consistent with the assumption that there is a larger net number of noise generating traps in a *pnp* SiGe HBT than in a *npn* SiGe HBT. In addition, high noise variation may not be an intrinsic property of these *npn* devices, but may rather be due to their small magnitude LFN compared to *pnp* SiGe HBTs. A further study comparing the noise variation between *npn* and *pnp* devices with comparable LFN should clarify this issue.

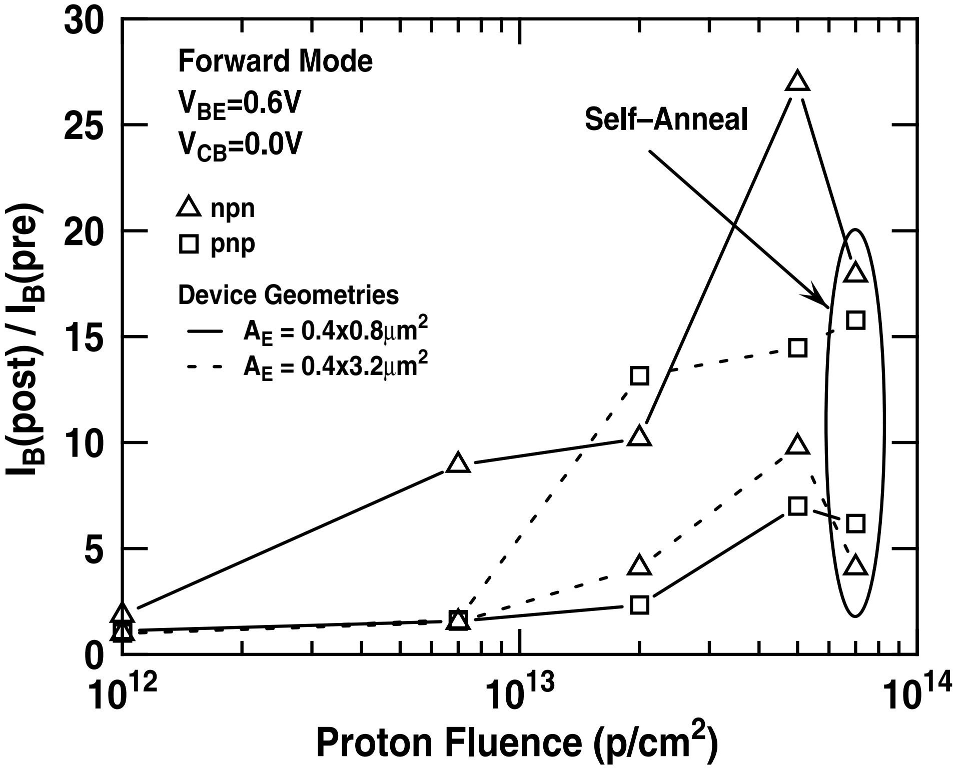

Figure 21: I_B degradation as a function of fluence in forward mode for complementary SiGe HBTs with A_E=0.4×0.8 μm^2 and A_E=0.4×3.2 μm^2 at V_{CB}=0.0 V and $|V_{BE}|$=0.6 V.

4.6 Physics of LFN in Complementary SiGe HBTs

The results of this investigation, taken together, suggest that the dominant LFN sources are in the IFO layer. To simplify the analysis of $1/f$ noise here, the following assumptions are proposed:

1. A uniform IFO layer is assumed in this analysis, since layer break-up does not generate the dominant component either in DC currents or in LFN, as demonstrated by the data in Figure 11 and Figure 14.
2. The trap density variation at the quasi-Fermi level can be neglected due to the tiny voltage drop across the IFO ($<< kT/q$) [68] [76].

Hence, the models discussed in Chapter III can also be used to explain the LFN behavior exhibited in this chapter. Substituting (71) and (74) into (64) gives

$$S_I = \frac{Cq^4 I^2}{AkTC_{mo}^2} \cdot [\int_0^{t_{ox}} N_{IFO}(E_{FNm}, z, t_{ox}) \frac{\tau_{mono}}{1+\omega^2\tau_{mono}^2} dz + \frac{0.1 D_{it}(E_{FNm})}{f}] \qquad (85)$$

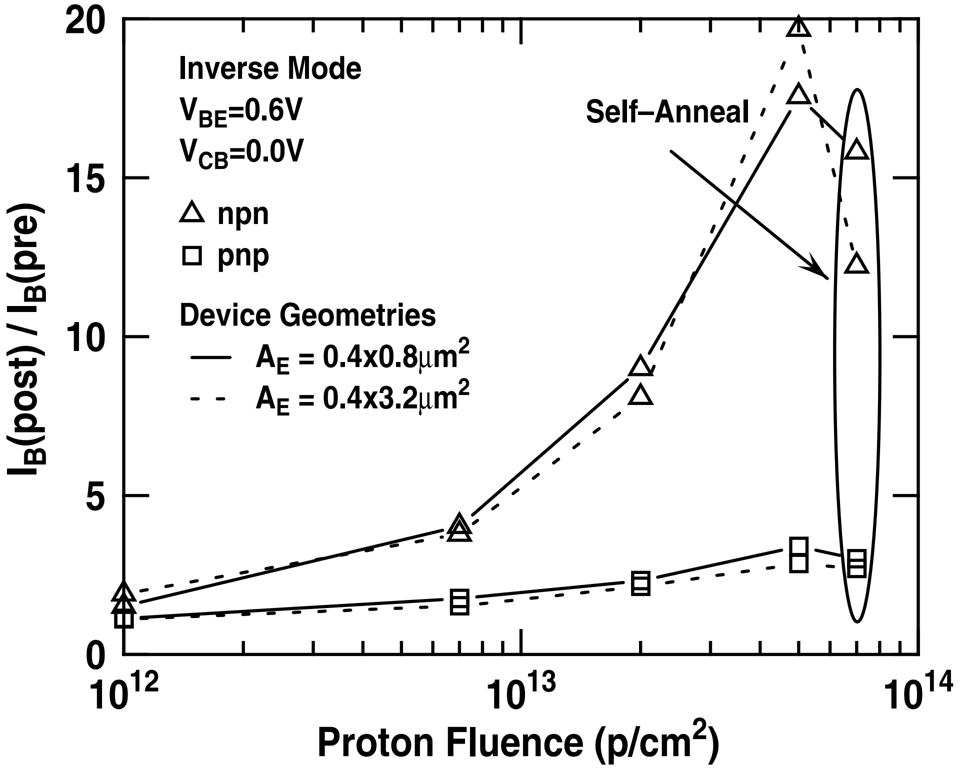

Figure 22: I_B degradation as a function of fluence in inverse mode for complementary SiGe HBTs with A_E=0.4×0.8 μm^2 and A_E=0.4×3.2 μm^2 at V_{CB}=0.0 V and $|V_{BE}|$=0.6 V.

which demonstrates that both the two-step tunneling and carrier random-walk models theoretically predict a $1/A$, $1/T$, and I^2 dependence of $1/f$ noise. However, the exponential dependence of $1/f$ noise on the IFO thickness cannot be readily explained by either of these models since exact values for the surface state density D_{it}, the oxide trap density N_{IFO}, and the interface capacitance density C_{mo} are not available from the literature due to the ultra-thin IFO in the present case. The absence of such information, however, does not rule out the possibility that the exponential dependence of $1/f$ noise on the IFO thickness could result from either $N_{IFO}(E_{FNm}, z, t_{ox})$ or $D_{it}(E_{FNm})$ being proportional to exp(t_{ox}/λ_{cn}) (where t_{ox} is in the unit of Å and λ_{cn}=0.5 Å), assuming that C_{mo} is independent of t_{ox}. Moreover, the IFO in some polysilicon emitter BJTs and SiGe HBTs is intentionally removed in order to reduce noise. In this case, the random walk model becomes more applicable. Using data from Figure 13, $D_{it}(E_{FNm})/C_{mo}^2$ is estimated to be between 3.4×10^{21} cm$^2 \cdot F^{-2}$·eV^{-1} and 3.6×10^{22} cm$^2 \cdot F^{-2}$·eV^{-1}. The $D_{it}(E_{FNm})/C_{mo}^2$ values evaluated for *npn* and *pnp* devices with

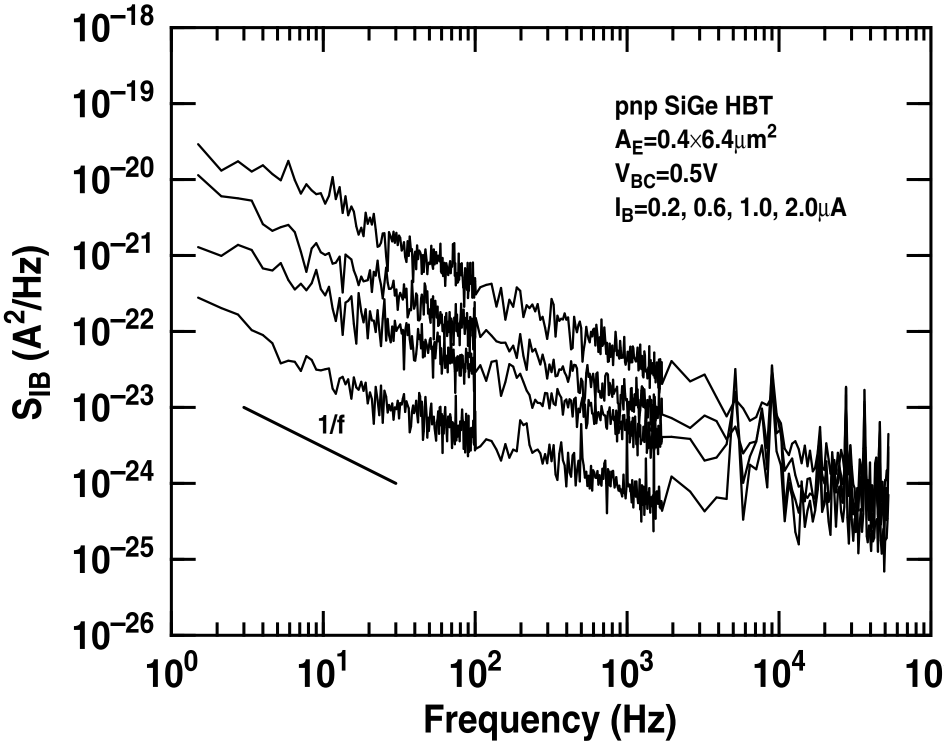

Figure 23: S_{IB} at different base currents for a *pnp* SiGe HBT with A_E=0.4×6.4 μm^2 at V_{BC}=0.5 V.

A_E=0.4×6.4 μm^2 but different t_{ox} are listed in Table I. Note, however, that as the C_{mo} values for such thin oxide films are not available in the literature, $D_{it}(E_{FNm})$ and $N_{IFO}(E_{FNm}, z, t_{ox})$ cannot be evaluated here.

A major drawback for applying the two-step tunneling model in the present case is that it is difficult to generate $1/f$ noise from two-step tunneling, which normally requires IFO thicknesses over 20 Å [62]. Therefore, although the two-step tunneling mechanism is important, it may not be the dominant noise source in the devices tested for this study. However, an advantage of this tunneling model lies in its ability to explain the small-size effects observed in *npn* devices with a minimized emitter area. As the emitter area shrinks, $N_{IFO}(E_{FNm}, z, t_{ox})$ ceases to exhibit a uniform distribution over the tunneling distance z. Therefore, the Lorentzian spectrum from traps associated with a specific tunneling distance may become much larger than that originating from traps with other tunneling distances. For example, the most active traps in the *npn* device that show a strong Lorentzian shape in Figure 28 might occur between z=5.0 Å and z=5.1 Å. In other

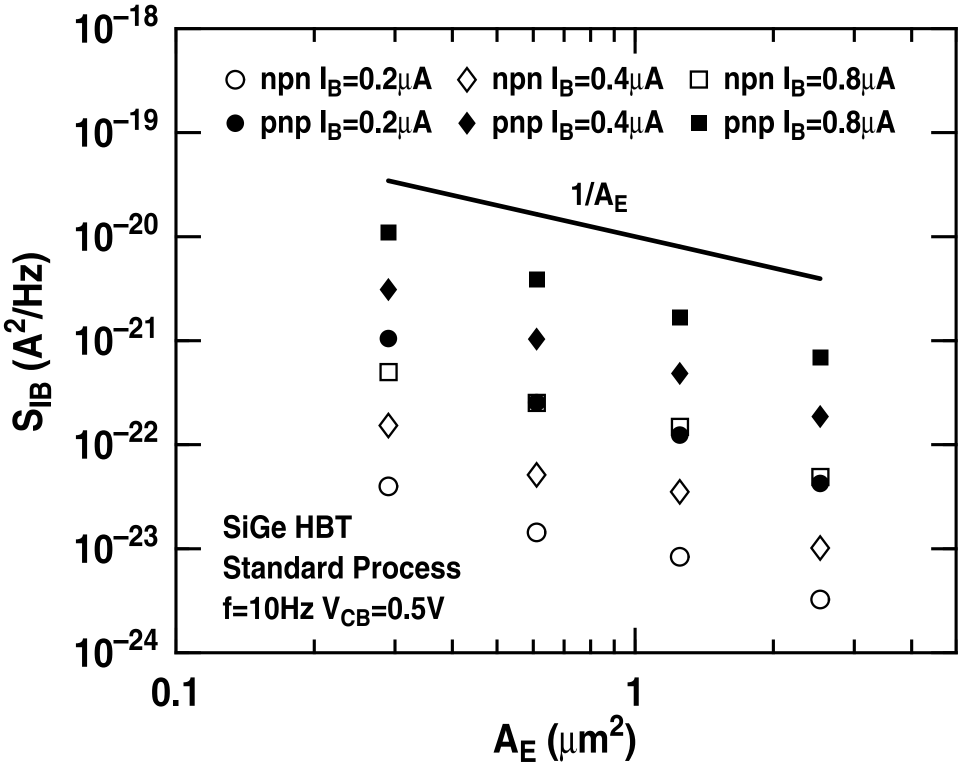

Figure 24: Extracted power spectra densities S_{IB} at 10 Hz as a function of the emitter area at $|V_{BC}|$=0.5 V.

words, $N_{IFO}(E_{FNm}, z, t_{ox})$ is a quasi-delta function with uniform distribution between z=5.0 Å and z=5.1 Å. Assuming $\tau_0 \approx 2.2 \times 10^{-6}$ s, $\lambda \approx 0.8$Å, $N_{IFO}(E_{FNm}, z, t_{ox})/C_{mo}^2$ for z ranging from 5.0 Å to 5.1 Å around $5{\times}10^{29}$ cm$\cdot F^{-2}\cdot$eV^{-1}, $D_{it}(E_{FNm})/C_{mo}^2 \approx 3.0{\times}10^{20}$ cm$^2 \cdot F^{-2}\cdot$eV^{-1}, extracted from a device demonstrating a pure $1/f$ shape, (85) gives the simulation result shown in Figure 28, which matches the measurement data very well. The value for τ_0 used here is chosen only for mathematical convenience (i.e., it is essentially used as a fitting parameter). However, using the random-walk model is not easy to explain this small-size effect since the $1/f$ spectrum in this model depends on the number of traps and not on the distribution of the time constants.

The higher magnitude observed in the $1/f$ noise of *pnp* devices compared with *npn* devices suggests that the IFO trap density in *pnp* transistors must be higher than that in *npn* transistors [77]. This is further supported by the radiation data, in which the additional traps induced by proton irradiation dramatically increase $1/f$ noise in *npn* transistors, while having almost no effect on *pnp* transistors. Assuming that proton irradiation induces a comparable number of traps in *npn* and *pnp*

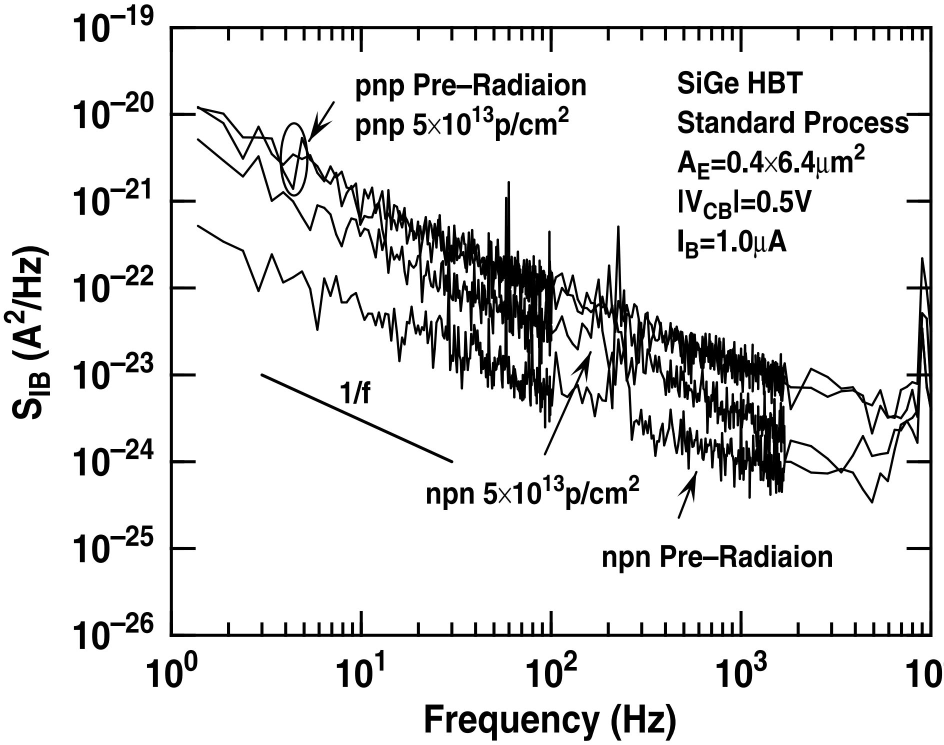

Figure 25: Comparison of the pre-radiation and the post-radiation S_{IB} spectra for both *npn* and *pnp* SiGe HBTs with A_E=0.4×6.4 μm^2 at $|V_{BC}|$=0.5 V.

devices, the dramatic increase in the $1/f$ noise of *npn* devices results from the additional traps added by irradiation being comparable to the initial number of traps in these devices. However, the number of traps in pre-radiation *pnp* devices is probably much larger than that created by irradiation. Therefore, the extra traps added by irradiation do not have a significant effect on the magnitude of $1/f$ noise, suggesting that the number of traps in pre-radiation *pnp* transistors is significantly higher than that in pre-radiation *npn* devices. It should also be emphasized that this high radiation tolerance may not actually be an intrinsic property of *pnp* SiGe HBTs, since the *pnp* devices had a higher LFN magnitude than the *npn* devices in this study. Further work on the radiation tolerance of *npn* and *pnp* devices with comparable LFN should therefore be performed to clarify this issue.

The tunneling-assisted trapping model uses the same tunneling mechanism as the two-step tunneling model. The difference between these two models mainly lies in the different trap positions. Firstly, the tunneling-assisted trapping model assumes that the dominant noise source modulates the surface recombination current, which is observed only at a low biasing level, while the two-step

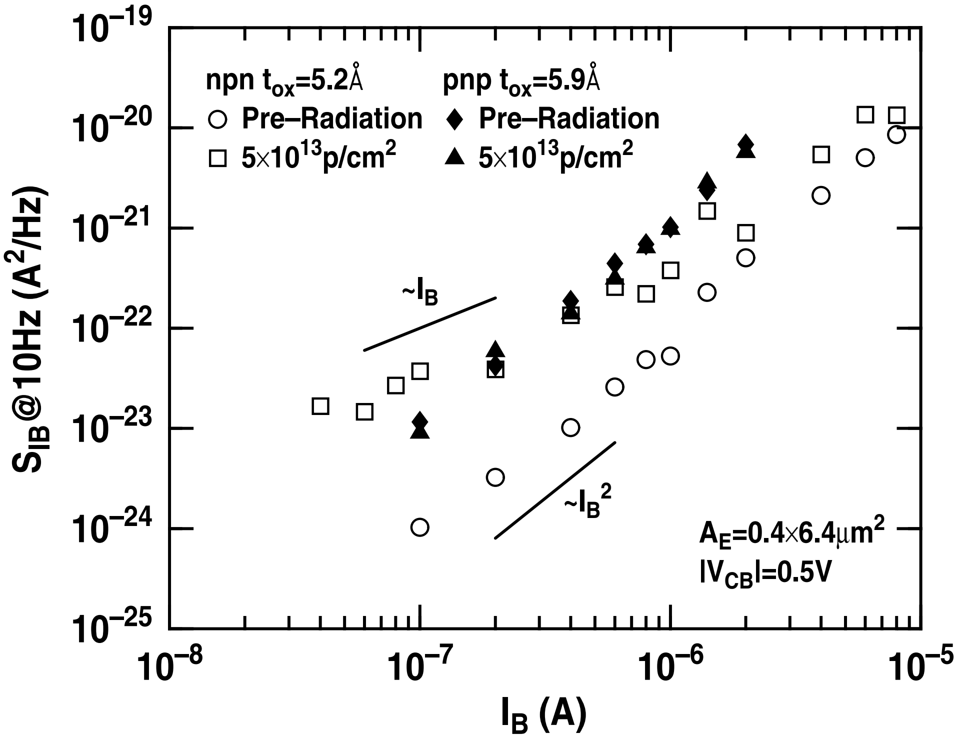

Figure 26: Effects of irradiation on the bias dependence of LFN at 10 Hz for both *npn* and *pnp* SiGe HBTs with A_E=0.4×6.4 μm^2 at $|V_{BC}|$=0.5 V.

tunneling model focuses on the diffusion current that is the dominant component of the base current in the normal operation region. Furthermore, since traps for the tunneling-assisted trapping model are in the spacer oxide over the E-B junction, the LFN predicted by this model should have a dependence on the emitter periphery (P_E). However, traps for the two-step tunneling model are within the IFO, which is proportional to A_E. In addition, the spacer oxide is thick enough to generate a $1/f$ shape in the frequency domain, but the ultra-thin IFO can only produce LFN with a Lorentzian shape.

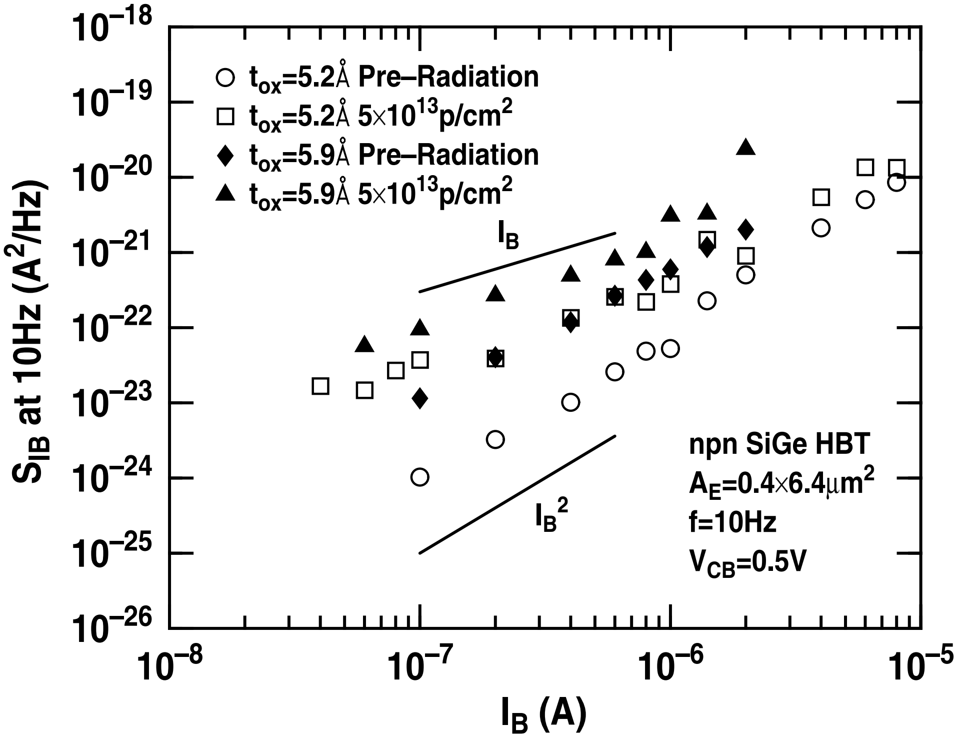

Figure 27: Effects of irradiation on the bias dependence of LFN at 10 Hz in *npn* SiGe HBTs with different interfacial oxide thicknesses and A_E=0.4×6.4 μm^2 at V_{CB}=0.5 V.

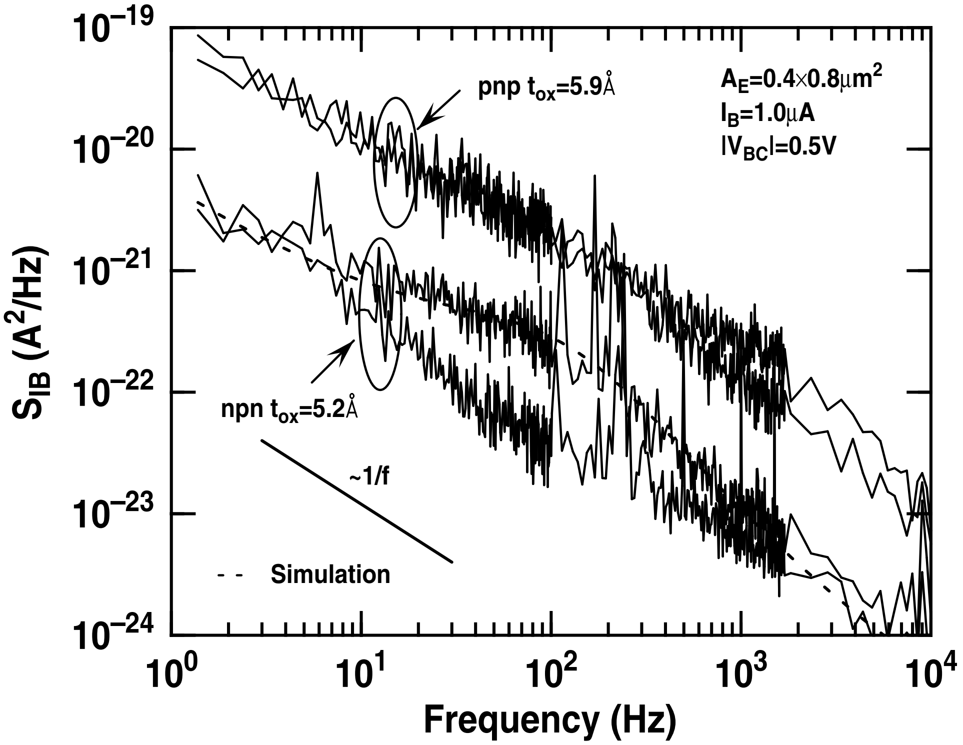

Figure 28: Noise power spectral densities measured from two identical transistors for *npn* and *pnp* SiGe HBTs, respectively, with the emitter area A_E=0.4×0.8 μm^2 at I_B=1.0 μA and $|V_{BC}|$ = 0.5 V. The model discussed in Section 4.6 is used for simulation with $\tau_0 \approx 2.2 \times 10^{-6}$ s, $\lambda \approx$ 0.8Å, $N_{IFO}(E_{FNm}, z, t_{ox})/C_{mo}^2$ for z ranging from 5.0 Å to 5.1 Å around 5.0×10^{29} cm·F^{-2}·eV^{-1}, $D_{it}(E_{FNm})/C_{mo}^2 \approx 3.0\times10^{20}$ cm$^2 \cdot F^{-2}$·eV^{-1}.

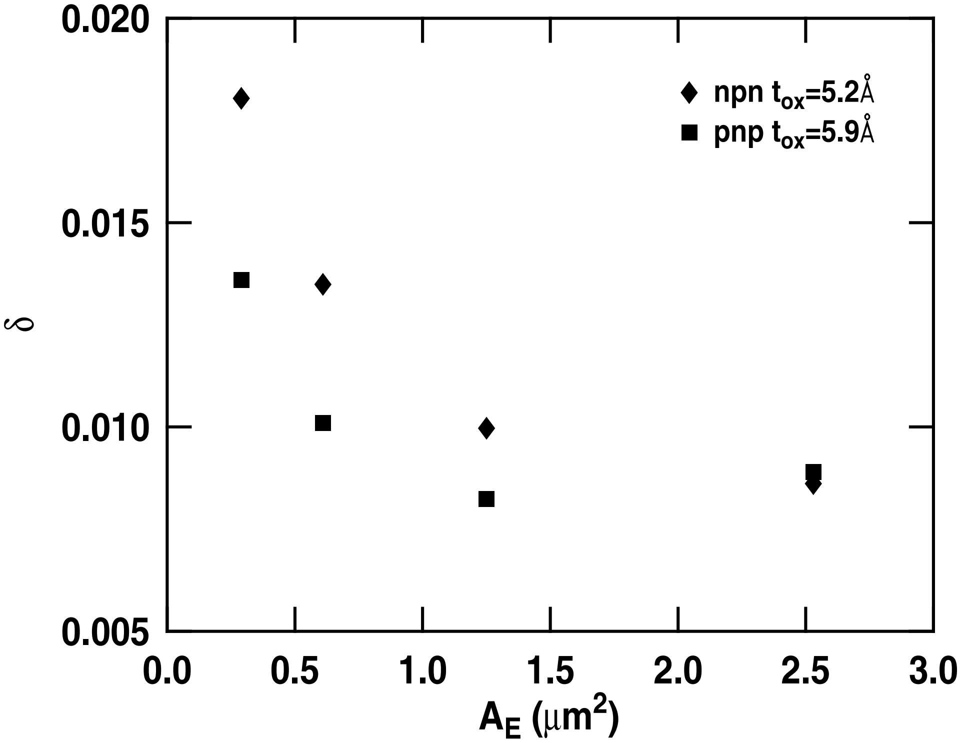

Figure 29: Noise variation coefficient versus emitter area for *npn* SiGe HBTs with t_{ox}=5.2 Å and *pnp* SiGe HBTs with t_{ox}=5.9 Å.

CHAPTER V

THE GEOMETRICAL DEPENDENCE OF LFN IN NPN SIGE HBTS

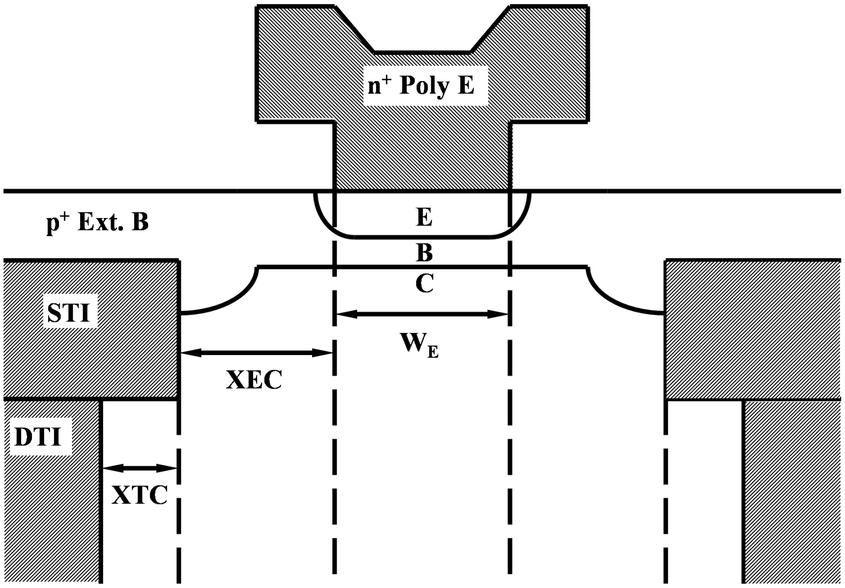

Figure 30: Schematic cross-section of a *npn* SiGe HBT.

5.1 Introduction

Several fabrication techniques, such as removing the IFO have been shown to be very promising for reducing LFN [37][38]. However, these methods all results in increased processing complexity and hence add unwanted cost. In contrast, optimizing the device geometry to improve noise performance is very attractive due to its simplicity.

In order to reduce noise by optimizing the device geometry, however, a thorough understanding of the noise characteristics of devices with varying geometries is essential. The LFN of SiGe

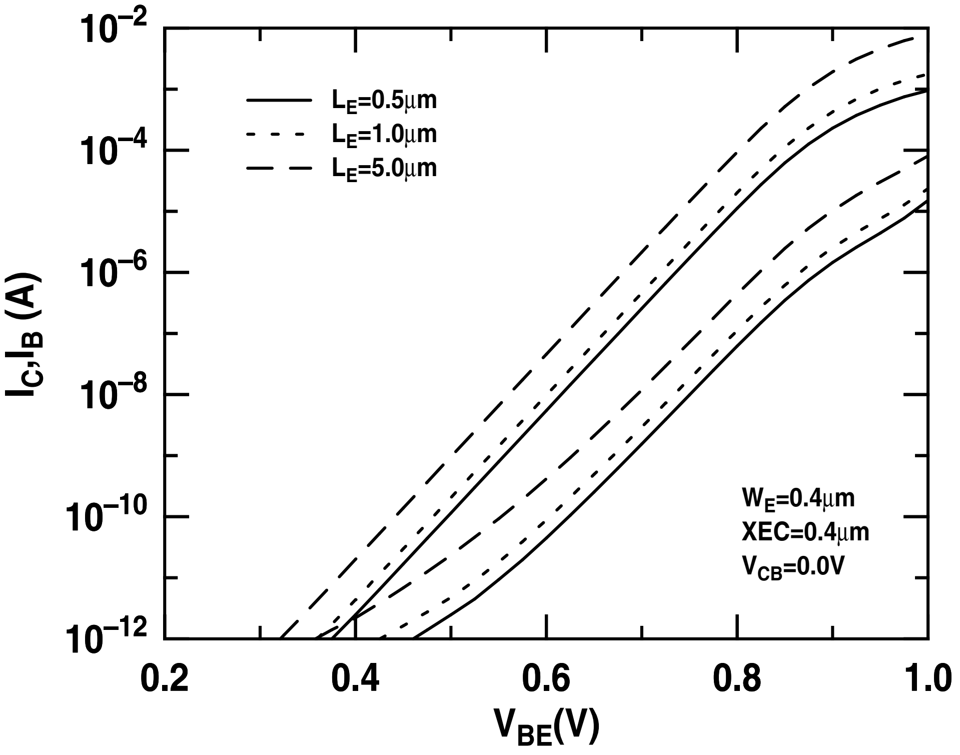

Figure 31: Gummel characteristics of *npn* SiGe HBTs with different emitter length L_E. Data were measured from *npn* SiGe HBTs with W_E=0.4 μm, XEC=0.4 μm, and V_{CB}=0.5 V.

HBTs and polysilicon emitter Si BJTs with different emitter geometries has been investigated extensively in the past [49][52][69][74][78]-[87]. Most of these studies [49][52][69][78]-[86] suggest that $1/f$ noise is associated with A_E (i.e., an A_E^{-1} dependence). In [74], $1/f$ noise is considered a function of both A_E and P_E, with the P_E/A_E ratio in the range of 2.65-3.50. The authors found that $1/f$ noise showed both an A_E^{-1} and a P_E^{-1} dependence, and speculated that this was related to fabrication tolerances in the width of the emitter. Recently, [87] presented a paper on devices with varying W_E that indicated that $1/f$ noise is generated at P_E. Although this study covered a relatively large range of P_E/A_E ratios, transistors with different L_E, which are generally more relevant to actual circuit designs, were not discussed. Moreover, in investigating the physical mechanism of $1/f$ noise, opinions are generally divided into two groups, one of which suggests that the measured noise comes from the diffusion current, while the other considers that it comes from the surface recombination current [78] [79][80][88]. The noise from the surface recombination current generally has a P_E^{-1} dependence and a non-quadratic dependence on I_B, whereas the noise from

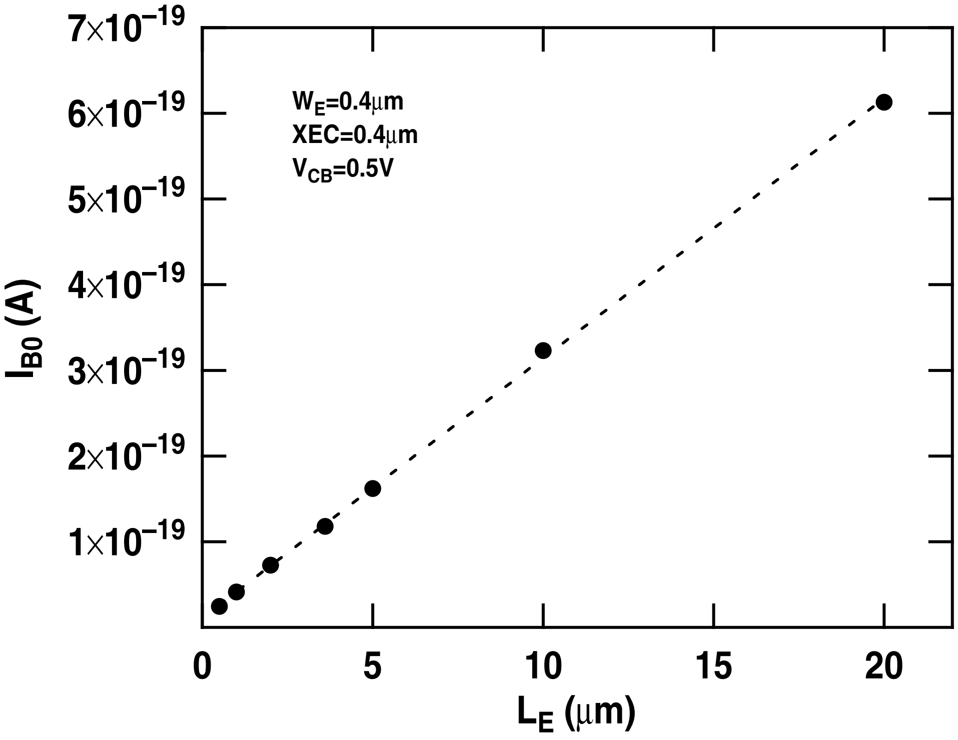

Figure 32: The base saturation current I_{B0} as a function of the emitter length L_E for *npn* SiGe HBTs with L_E between 0.5 μm and 20.0 μm. Data were measured from *npn* SiGe HBTs with W_E=0.4 μm, XEC=0.4 μm, and V_{CB}=0.5 V.

diffusion current is normally believed to be inversely proportional to A_E with a quadratic dependence on I_B, since the diffusion current has almost the same magnitude as I_B under normal biasing conditions [78][79][80][88]. However, considering that a significant component of the diffusion current may consist of the flux in the lateral direction, the universal A_E^{-1} and I_B^2 dependence for the $1/f$ noise of the diffusion current still remains questionable. In addition, in order to reduce LFN, a better understanding of the impact on the LFN of dimensional variations in other device structure components, such as XEC and XTC, is highly desirable.

The *npn* SiGe HBTs used in the research reported in this chapter were manufactured by National Semiconductor and target analog circuit applications. This SiGe technology uses a combination of shallow trenches and deep trenches to isolate the device (Figure 30). For the standard process, the devices have a peak f_T of about 70 GHz, a BV_{CEO} of about 2.9 V, and a V_A of about 100 V. The devices used in this noise study have fixed W_E=0.4 μm, and several different L_E: 0.5 μm, 1.0 μm, 2.0 μm, 3.6 μm, 5.0 μm, 10.0 μm, and 20.0 μm. Four different values of XEC were used in this

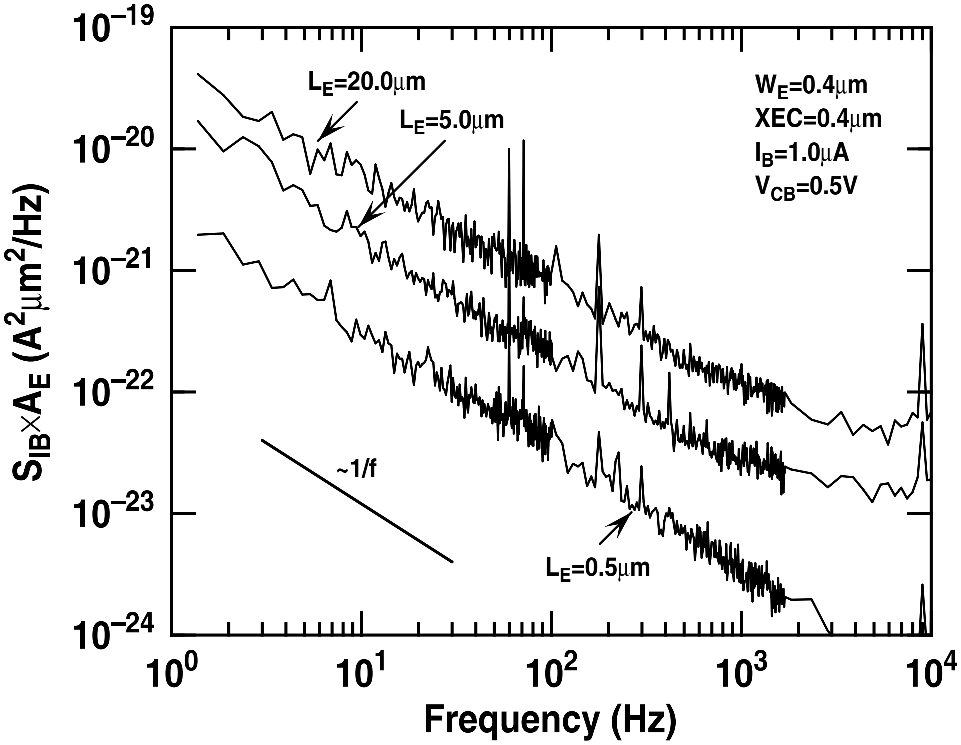

Figure 33: The multiplication product of S_{IB} and A_E at I_B=1.0 μA versus frequency for *npn* SiGe HBTs with different L_E. Data were measured from *npn* SiGe HBTs with W_E=0.4 μm, XEC=0.4 μm and V_{CB}=0.5 V.

technology: 0.25 μm, 0.30 μm, 0.35 μm, and 0.40 μm; while two different values of XTC were examined: 0.30 μm and 0.35 μm.

5.2 L_E Effects

The Gummel characteristics of SiGe HBTs with varying L_E are shown in Figure 31. As expected, both I_B and I_C increase as L_E increases. I_{B0} as a function of L_E is plotted in Figure 32. As the figure shows, I_{B0} is proportional to L_E, which proves that the drawn and electrical emitter geometries are nearly identical.

Figure 33 shows typical LFN spectra measured from devices with varying L_E. As L_E ranges from 0.5 μm to 20.0 μm, LFN spectra exhibit a clear $1/f$ shape in the frequency domain. Figure 34 shows $1/f$ noise as a function of I_B. For L_E ranging from 0.5 μm to 20.0 μm, $1/f$ noise shows an inconsistent dependence on I_B. For instance, the $1/f$ noise of devices with L_E<5.0 μm obeys a classical quadratic dependence on I_B, but when L_E reaches 20.0 μm, the $1/f$ noise is almost

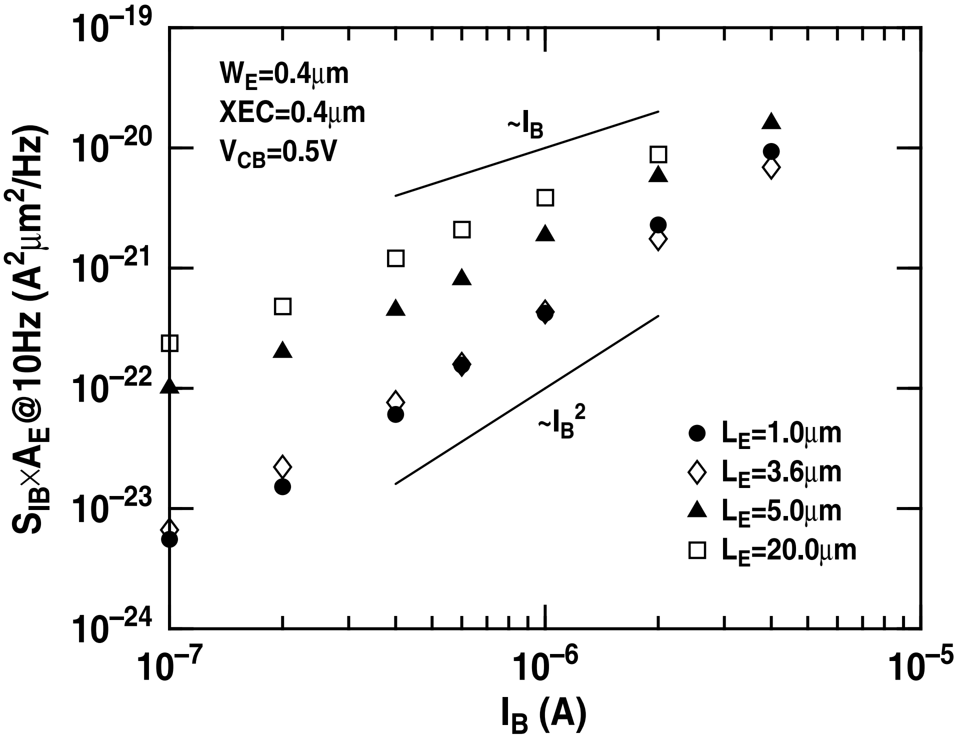

Figure 34: The product of the magnitude of $1/f$ noise S_{IB} at 10 Hz and A_E versus I_B with different L_E. Data were measured from *npn* SiGe HBTs with W_E=0.4 μm, XEC=0.4 μm and V_{CB}=0.5 V.

proportional to I_B. The SPICE noise parameter A_F, which is defined in (82), also demonstrates the same behavior. A_F as a function of L_E is shown in Figure 35. The error bar in Figure 35 represents the range of A_F extracted from seven samples on different dies. The solid circles are the median values of A_F minimizing the effects of the large data fitting tolerance. From Figure 35, the median values of A_F for devices with $L_E \leq 3.6$ μm are close to 1.9. However, A_F decreases to 1.6 for devices with L_E=5.0 μm and approaches 1.2 when L_E becomes larger than 5.0 μm, which suggests that a fundamentally different noise mechanism is dominant in devices with $L_E \leq 3.6$ μm. For comparison purposes, S_{IB} at 10 Hz was normalized to unity for the shortest L_E (at a fixed I_B, S_{IB} at 10 Hz for different L_E were divided by S_{IB} at 10 Hz extracted from the device with L_E=0.5 μm), and plotted in Figure 36. The normalized S_{IB} at 10 Hz tends to have a $1/P_E$ dependence for L_E ranging from 0.5 μm to 3.6 μm, instead of the expected classical $1/A_E$ behavior. For L_E>3.6 μm, it is difficult to differentiate whether LFN is correlated to A_E or P_E, since the P_E/A_E ratios in that range are very close to one another. The noise variance of the emitter geometry was also compared.

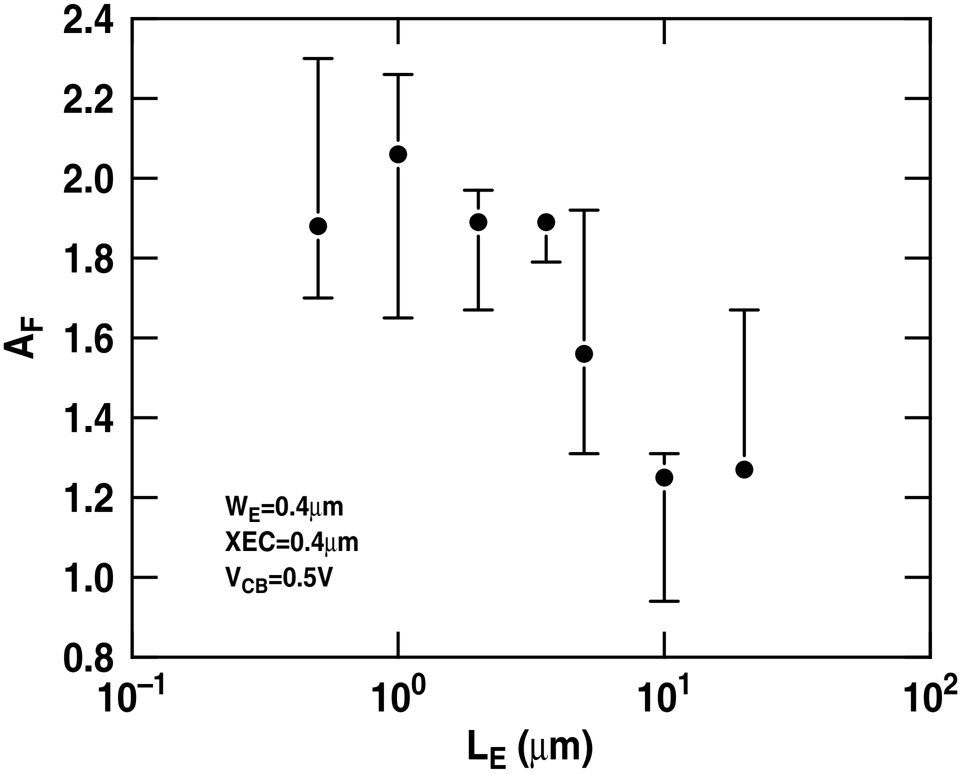

Figure 35: The SPICE noise parameter A_F as a function of the emitter length L_E. For each L_E, data were measured from *npn* SiGe HBTs with W_E=0.4 μm, XEC=0.4 μm and V_{CB}=0.5 V on seven different dies.

δ, which takes into accounts possible deviations occurring at any frequency and is defined in (83), is shown in Figure 37 with N_s=7 [2]. As expected, smaller devices result in a larger noise variation, as discussed at length in [2][41].

5.3 XEC and XTC Effects

Figure 38 shows typical noise spectra measured from two devices with different XEC, which shows LFN is dominated by $1/f$ noise. Furthermore, the device with a smaller XEC generated a larger amount of $1/f$ noise. Figure 39 shows the magnitude of the $1/f$ noise for devices with different XEC as a function of I_B, which also confirms that devices with smaller XEC give larger $1/f$ noise for I_B varying from 0.1 μA to 4.0 μA. As shown in Figure 39, the device with the smaller XEC has a slightly stronger dependence on I_B than the device with larger XEC, indicating that the device with smaller XEC has a higher trap density in the spacer oxide layer. Since the $1/f$ noise of devices with varying XEC have different dependences on I_B, it is clear that $1/f$ noise has a different

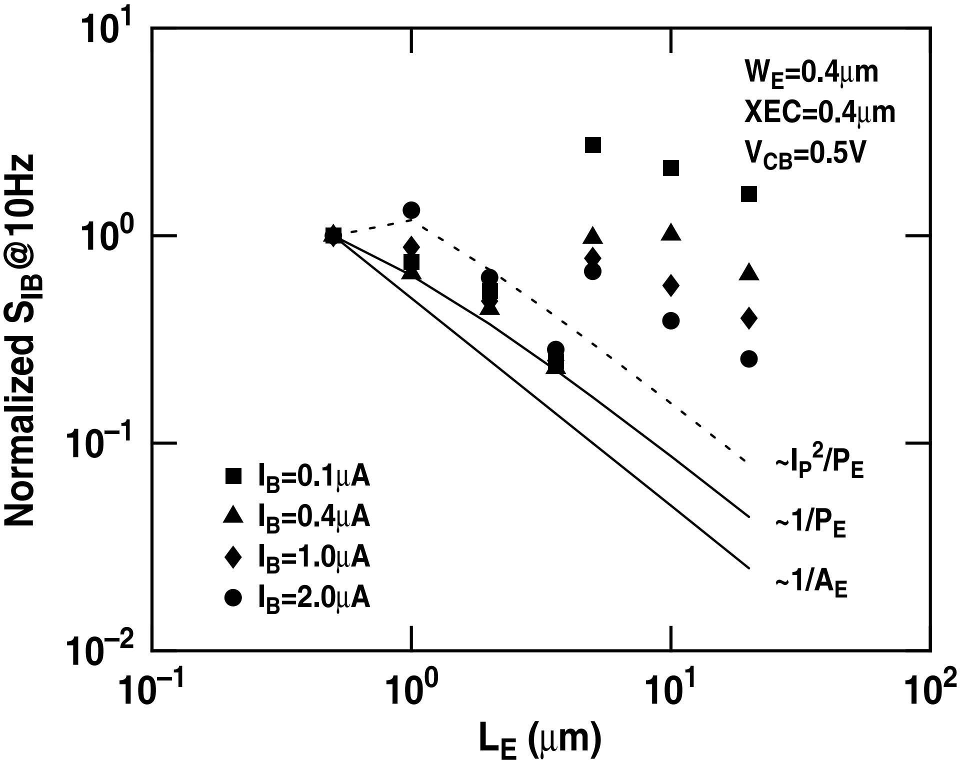

Figure 36: Normalized noise magnitude S_{IB} at 10 Hz to unity for the shortest L_E as a function of the emitter length L_E. Data were measured from *npn* SiGe HBTs with W_E=0.4 μm, XEC=0.4 μm and V_{CB}=0.5 V. I_p^2/P_E is defined in Section 5.4.

dependence on XEC for varying I_B, as shown in Figure 40. The normalized S_{IB} at 10 Hz for the shortest XEC (at a fixed I_B, S_{IB} at 10 Hz for different XEC is divided by S_{IB} at 10Hz extracted from the device with XEC=0.25 μm) shown in Figure 40 proves that the larger I_B makes the effects of varying XEC less significant.

Figure 41 demonstrates the magnitude of the $1/f$ noise for devices with varying XTC, which suggests that XTC does not have a significant impact on $1/f$ noise.

5.4 Discussion

The IFO between the polysilicon emitter and the monosilicon emitter is generally considered to be one of the most likely noise sources in SiGe HBTs and polysilicon emitter BJTs, as discussed in previous chapters. The current is modulated by the surface potential at the IFO-monosilicon interface when it tunnels through the IFO layer. Since the surface charge at the IFO-monosilicon interface can modulate this surface potential, the fluctuation in the number of surface charged carriers

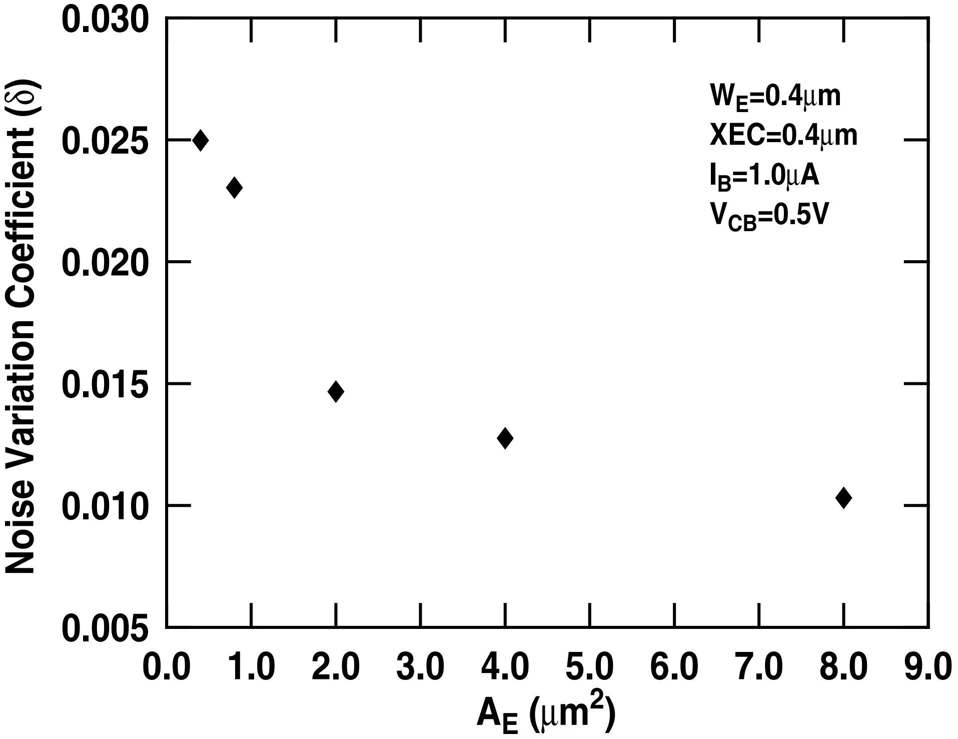

Figure 37: The noise coefficient δ at I_B=1.0 μA as a function of A_E. For each A_E, data were measured from *npn* SiGe HBTs with W_E=0.4 μm, XEC=0.4 μm and V_{CB}=0.5 V on seven different dies.

will eventually produce LFN. Furthermore, number fluctuations in the charged carriers are believed to originate from the IFO-monosilicon interface states and traps inside the IFO. As shown in chapter IV, LFN generated by the IFO in SiGe HBTs has a quadratic dependence on I, the tunneling current, and is inversely proportional to the effective IFO area. The evidence reported in this chapter supports the assertion that the $1/f$ noise of devices with $L_E \leq 3.6$ μm has its origin in the IFO. However, it also suggests that the noise-dominant region of the IFO is associated with P_E. In other words, this data indicates that the traps that dominate the $1/f$ noise of these devices are physically located at the periphery of the IFO layer at the edge of the emitter.

In order to investigate the dependence of $1/f$ noise on I_B, it is necessary to separate I_B as a function of its peripheral component I_p and its internal base current component I_i. Following [89]-[91], I_B at normal bias conditions is given by

$$I_B = I_i + I_p \approx A_E C_i exp\frac{qV_{BE}}{m_i kT} + P_E C_p exp\frac{qV_{BE}}{m_p kT} \tag{86}$$

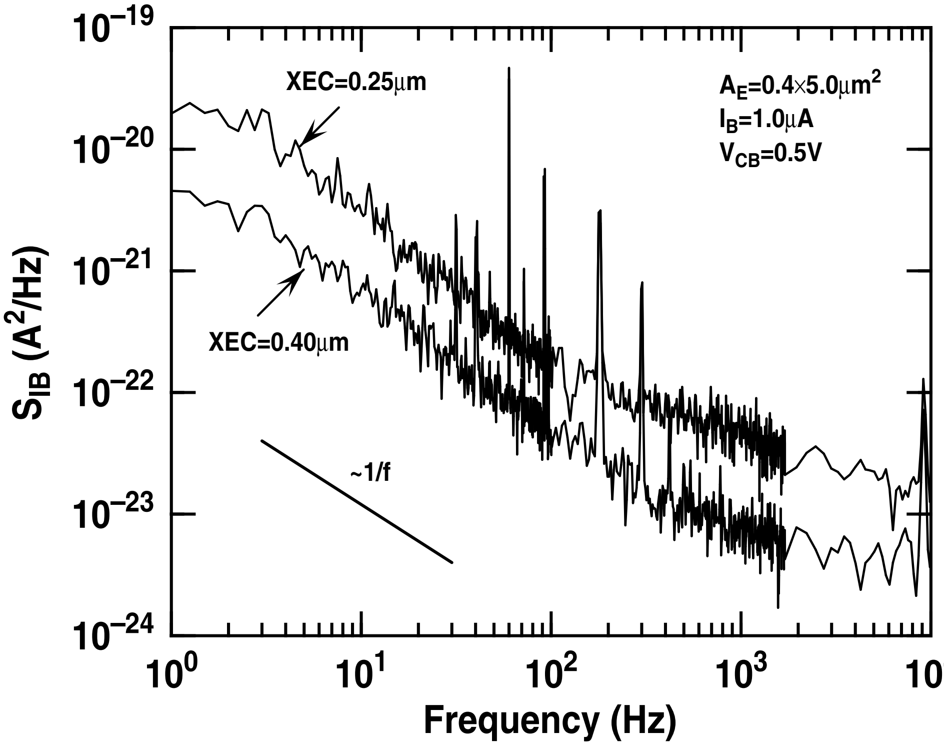

Figure 38: Typical noise power spectral densities S_{IB} measured from devices with A_E=0.4×5.0 μm^2 and different XEC at I_B=1.0 μA and V_{CB}=0.5 V versus frequency.

where I_i is proportional to A_E, I_p is proportional to P_E, C_i and C_p are constants independent of emitter dimensions, and m_i and m_p are ideality factors. At normal biasing, m_i and m_p can be considered to be very close to each other and approximately equal to unity. Hence, C_i and C_p can be precisely estimated from I_B of devices with different P_E/A_E ratios. Dividing (86) by A_E and setting V_{BE} to 0 yields

$$\frac{I_{B0}}{A_E} = C_i + C_p \frac{P_E}{A_E} \tag{87}$$

Figure 42 shows I_{B0} as a function of P_E/A_E. To simplify this case, I_{B0} can be divided into two regions: 5.1 μm^{-1}$\leq P_E/A_E \leq$7.0 μm^{-1} and P_E/A_E>7.0 μm^{-1}, allowing C_i and C_p to be extracted from those two regions, respectively. Since only one device with P_E/A_E=9.0 μm^{-1} is in the region of P_E/A_E>7.0 μm^{-1}, C_i and C_p are extracted from two points: P_E/A_E=7.0 μm^{-1} and P_E/A_E=9.0

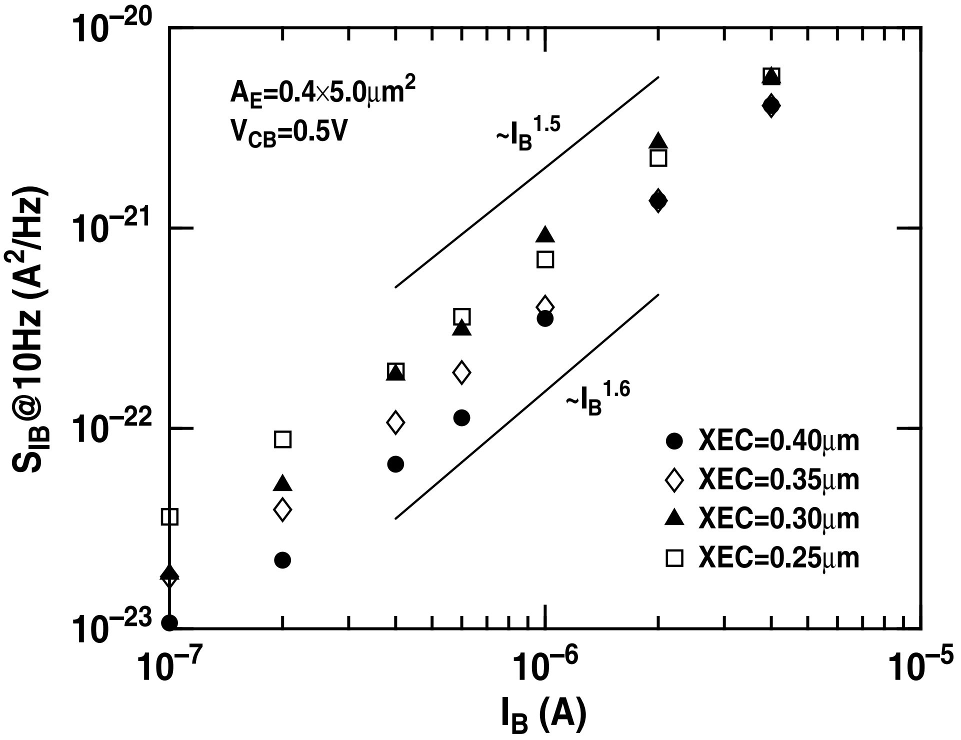

Figure 39: The magnitude of $1/f$ noise, S_{IB} at 10 Hz, measured from devices with A_E=0.4×5.0 μm^2 and V_{CB}=0.5 V as a function of the base current I_B.

μm^{-1}. For P_E/A_E= 9.0 μm^{-1}, C_i and C_p are roughly 3.59×10^{-20} A/μm^2 and 9.63×10^{-21} A/μm, respectively. However, for 5.1 μm^{-1}≤ P_E/A_E ≤7.0 μm^{-1}, C_i and C_p change to 3.99×10^{-21} A/μm^2 and 1.42×10^{-20} A/μm, respectively.

As stated in Chapter III, LFN generated by traps at the IFO periphery (S_p) is defined by

$$S_p = C \cdot \frac{q^2 S_{Q_{mo}}}{k^2 T^2 C_{mo}^2} \cdot \frac{I_p^2}{A} \tag{88}$$

where C is a dimensionless ideality factor, $S_{Q_{mo}}$ is the monosilicon-IFO interface charge spectral density per unit area, C_{mo} is the monosilicon-IFO interfacial capacitance per unit area, I_p is considered as tunneling through the effective IFO in this case, and A=P_E × W_{IFO} is the area of the effective IFO, in which W_{IFO} is the width of the effective IFO at the emitter edge [2]. Hence, S_p has a quadratic dependence on I_p and is inversely proportional to P_E, $S_p \propto I_p^2/P_E$.

Following (86) and (87), I_p^2/P_E becomes

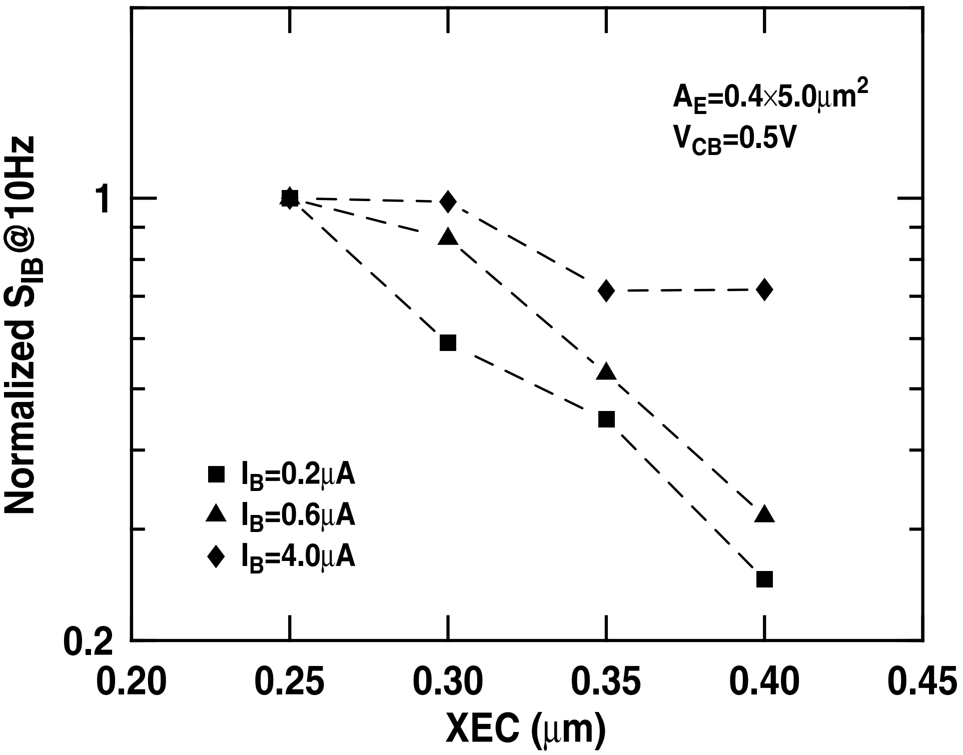

Figure 40: Normalized $1/f$ noise magnitude, S_{IB} at 10 Hz, to unity for the shortest XEC with A_E=0.4×5.0 μm^2 and V_{CB}=0.5 V versus XEC at different base currents.

$$\frac{I_p^2}{P_E} = \frac{I_p^2}{P_E I_B^2} I_B^2 = \frac{(P_E C_p)^2}{P_E (P_E C_p + A_E C_i)^2} I_B^2 = \frac{1}{P_E (1 + \frac{A_E C_i}{P_E C_p})^2} I_B^2 (m_i \approx m_p \approx 1.0) \tag{89}$$

for 5.1 μm^{-1}≤ P_E/A_E ≤7.0 μm^{-1}, C_i/C_p is approximate 0.28 μm^{-1}, and A_E/P_E is less than 0.2 μm. Hence, $(A_E C_i)/(P_E C_p)$<0.056, and can be considered <<1. Substituting the value of $(C_i A_E)/(C_p P_E)$ into (89) gives

$$\frac{I_p^2}{P_E} \approx \frac{I_B^2}{P_E} \; (5.1\mu m^{-1} \leq \frac{P_E}{A_E} \leq 7.0\mu m^{-1}) \tag{90}$$

If S_p is the dominant component of S_{IB}, (90) suggests that S_{IB} has an approximately P_E^{-1} and I_B^2 dependence for devices with L_E≤3.6 μm, as shown in Figure 36. Moreover, considering the base current crowding effects, which suggest that I_i increases in devices with very small emitters, S_{IB}

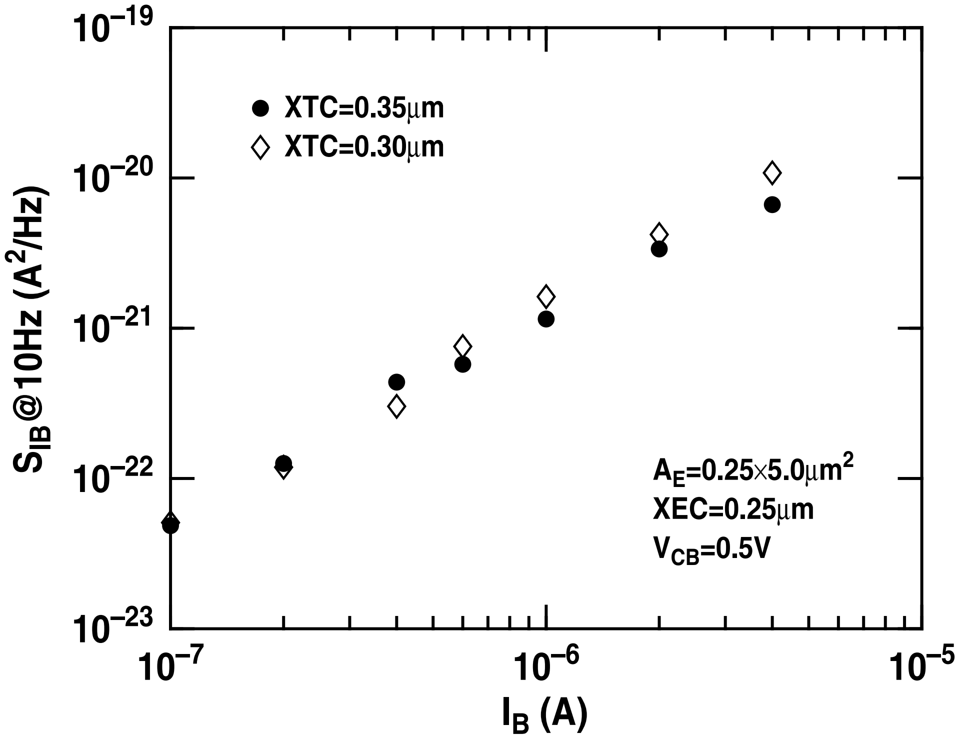

Figure 41: The magnitude of $1/f$ noise, S_{IB} at 10 Hz, measured from devices with A_E=0.25×5.0 μm^2, XEC=0.25 μm, but different XTC at V_{CB}=0.5 V as a function of I_B.

will slightly deviate from P_E^{-1}. In order to probe for current crowding effects, I_p^2/P_E was normalized to unity for the shortest L_E, as shown in Figure 36, and found to closely match the measured data, indicating that these assumptions are reasonable.

$S_{Q_{mo}}$ in (88) gives the $1/f$ dependence of S_p as demonstrated in (85), which can be defined by

$$S_{Q_{mo}} = \frac{0.1q^2}{f} kTD_{it} \tag{91}$$

where D_{it} is the IFO-monosilicon interface state density in units of cm^{-2}·eV^{-1}. Substituting (91) into (88) yields

$$S_p = C \cdot \frac{0.1q^4 I_p^2}{kTfP_E W_{IFO}} \cdot \frac{D_{it}}{C_{mo}^2} \tag{92}$$

Substituting a typical value of D_{it}/C_{mo}^2=4.4×10^{20} cm^2 · F^{-2}·eV^{-1} extracted from a *npn* SiGe HBT

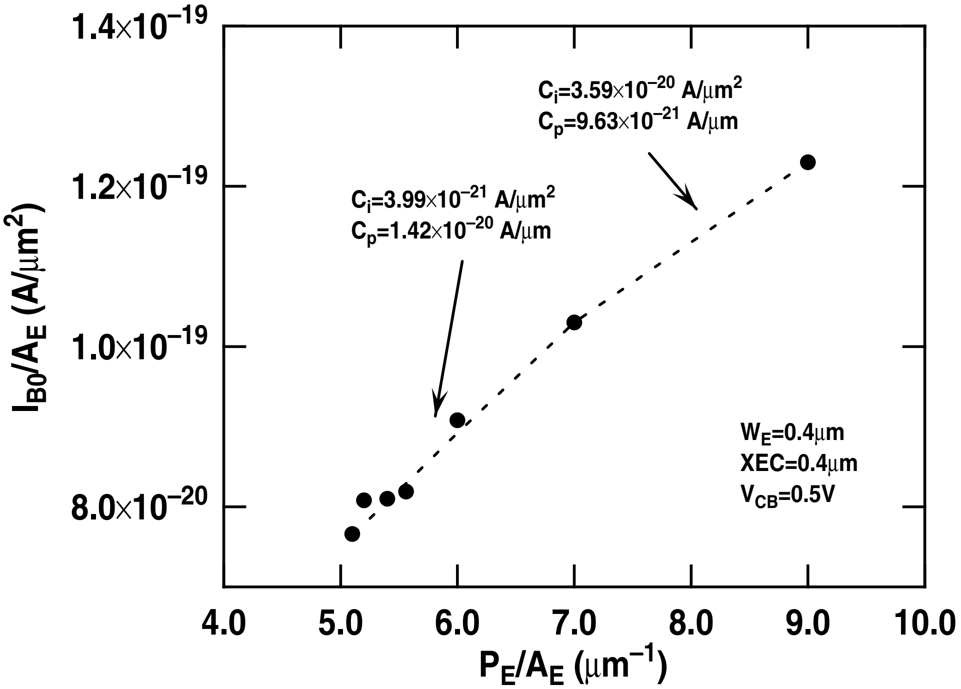

Figure 42: The base saturation current I_{B0} per unit area versus the ratio of the emitter perimeter P_E to the emitter area A_E. Data were measured from devices with W_E=0.4 μm, XEC=0.4 μm and V_{CB}=0.5 V. C_i and C_p extracted from the region at P_E/A_E=9.0 μm^{-1} are roughly 3.59×10^{-20} A/μm^2 and 9.63×10^{-21} A/μm, respectively. When 5.1 μm$^{-1}\leq P_E/A_E \leq$7.0 μm^{-1}, C_i and C_p are 3.99×10^{-21} A/μm^2 and 1.42×10^{-20} A/μm, respectively.

with an IFO thickness close to 5.2 Å shown in Table I [2] and C=0.5 into (92), and using the data shown in Figure 36, a reasonable W_{IFO} value of close to 0.05 μm is obtained.

The other potentially important noise source in these devices is the emitter-base spacer oxide covering the E-B space charge region, as discussed in Chapter III. Traps within this spacer oxide can serve as SRH recombination centers and when carriers pass through the E-B junction, some can recombine and generate a surface recombination current. The surface potential at the junction-oxide interface can modulate this surface recombination current, so the fluctuation of the surface potential eventually generates LFN that is associated with the surface recombination current. Assuming that the spacer oxide is the dominant noise source and m_S ranges from 1.3 to 2.0 in (81), S_{IB} will have a dependence on I_B between $I_B^{1.5}$ and $I_B^{1.0}$. This model is very useful in explaining the A_F values for devices with $L_E \geq$5.0 μm, which are less than 1.5. In addition, this model also predicts the $1/P_E$ dependence of $1/f$ noise that is observed experimentally, providing strong support for the model.

LFN measured from devices with varying XEC indicates that XEC mainly affects the spacer oxide region. As shown in Figure 39, A_F for devices with different values of XEC lies between 1.5 and 1.6 and slightly increases with increasing XEC. This phenomenon indicates that $1/f$ noise is dominated by noise generated from the spacer oxide (m_S around 1.3) or has comparable contributions from both the spacer oxide and the IFO. This proposed mechanism can also be evaluated by investigating the fabrication processes involved. During non-selective base epi growth, the monosilicon emitter grows over the mono-crystalline substrate and the polysilicon emitter grows over the oxide region. Moreover, the IFO between the polysilicon emitter and the monosilicon emitter in the base epi is tilted from the STI towards the emitter window at about 45 degrees. Therefore, for devices with small XEC, the doping process can be very close to the E-B lateral junction, which is highly likely to introduce more defects into the spacer oxide at the perimeter portion of the E-B junction. In contrast, if XEC has a significant effect on the IFO, A_F should decrease as XEC increases since the $1/f$ noise generated by the IFO has a A_F value close to two.

CHAPTER VI

LFN OF LATERAL BJTS

6.1 Introduction

The rationale for investigating the LFN of lateral BJTs was presented in Section 1.4. This chapter opens with a brief introduction to the methods used to optimize the performance of lateral BJTs, which include using different doping profiles, different base widths (W_B), and different p type low-density drains (PLDD) among other. It then goes on to discuss the LFN characteristics of lateral BJTs.

6.2 DC and AC Characteristics

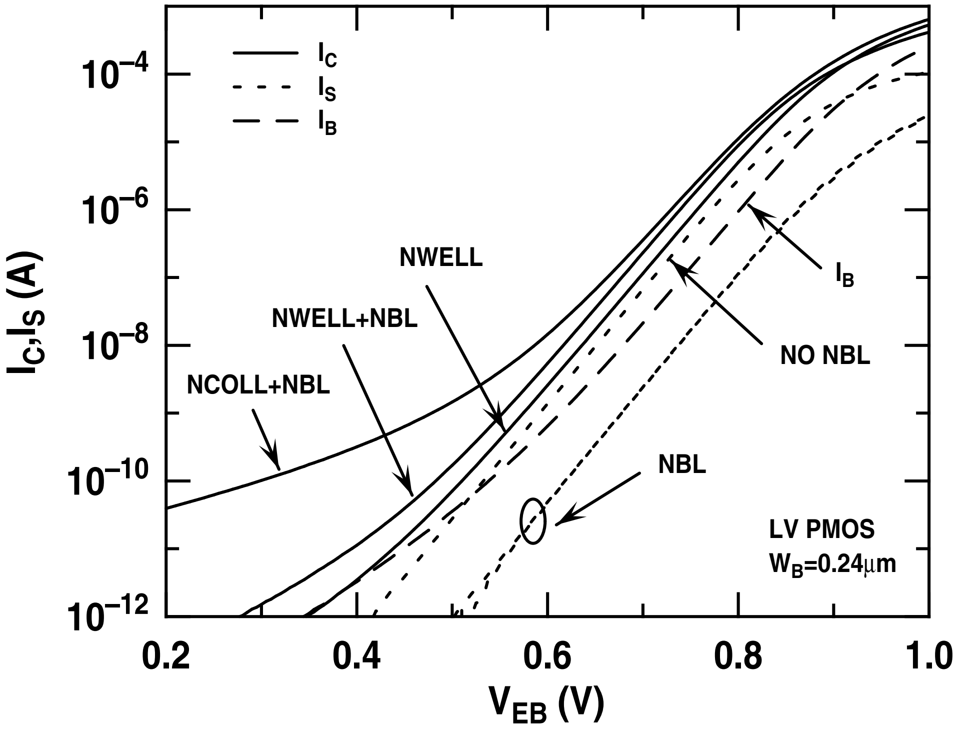

Figure 43: The collector current and the substrate vertical current vs. the emitter-base voltage for a lateral pnp BJT with different base profiles. The gate is tied to the emitter ($V_{GE} = 0.0V$) and $V_{BC} = 0.0V$.

The Gummel characteristics for three different base profiles (NCOLL + NBL, NWELL + NBL, and NWELL) are shown in Figure 43. For these measurements, tying the gate to the emitter ensures a true four terminal device (E/G, B, C, S), which is desirable for circuit applications. As shown in Figure 43, the base currents I_B were almost identical for all devices. However, the device with NWELL doping but no NBL (i.e., a standard pMOS) produced a significantly larger substrate current I_S than any of the devices with NBL, seriously compromising the device utility. Using NCOLL doping by itself gives the highest current gain β, although this also induces a large parasitic subthreshold leakage. The NWELL + NBL base profile offers the best subthreshold leakage (<1nA) in this study, but has the lowest current gain.

Table 2: Peak current gain and threshold voltage for lateral *pnp* BJTS using a NCOLL + NBL design approach (GOX represents the gate oxide).

$W_B(\mu m)$	HiPLDD	GOX	peak β	V_T(V)
0.30	NONE	LV	7.78	-0.236
0.30	NONE	HV	6.40	-0.342
0.30	E+C	HV	19.2	-0.086
0.35	E+C	HV	11.3	-0.253
0.40	E+C	HV	8.64	-0.317
0.40	C	HV	5.58	-0.348
0.40	NONE	HV	4.75	-0.378

Table 2 summarizes the peak β and the threshold voltage (V_T) measured for devices with various structures. From Table 2, the LV pMOS with a thinner oxide layer than the HV pMOS has a slightly higher β than the HV pMOS, and is thus a better starting point for the lateral *pnp*. Hence, the tradeoff in this case focuses on the off-state leakage, since V_T for the LV pMOS is larger than that for the HV pMOS.

As expected, the shortest base width (W_B) delivers easily the highest β, but it also produces the largest subthreshold leakage; V_T rises from -0.253 V to -0.086 V when W_B decreases from 0.35 μm to 0.30 μm. No significant changes occur when W_B>0.35 μm. Therefore, W_B should be carefully optimized to obtain the best tradeoff between attainable β and the subthreshold leakage.

The p^+ implantation (PLDD) used to improve the reliability of the CMOS device can also be used to reduce the effective base width in lateral *pnp* BJTs, hence, increase β. However, normal PLDD implantation using BF_2 with a dose of 1 × 10^{14} cm^{-2} at 20 keV produces a very shallow doping channel and does not affect the base width. Fortunately, HiPLDD using B^{11} with a dose of 1 × 10^{14} cm^{-2} at 15 keV is available for this process and is able to reduce the effective W_B. As shown in Table 2, a significant β enhancement is achieved when HiPLDD is implemented in both the emitter and the collector regions. Table 2 also shows that HiPLDD, applied in either the collector or the emitter, can reduce the effective W_B, but increase the subthreshold leakage.

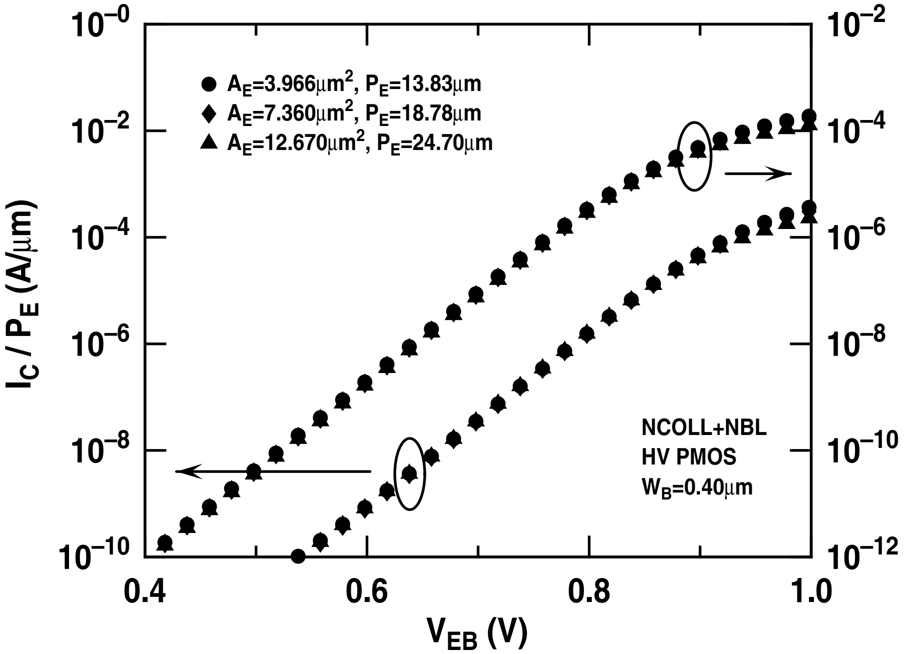

Figure 44: The collector current normalized to emitter perimeter I_C/P_E and the base current density (I_B/A_E) of lateral *pnp* BJTs with different emitter geometries as a function of V_{EB} at $V_{GB} = 1.0V$ (pMOS is off), and $V_{BC} = 0.0V$.

Devices with small emitter geometries enhance β. To investigate these geometrical effects in β, several devices with varying emitter geometries were fabricated and characterized. As expected, I_C was found to be dominated by the lateral injection current, as most of the collector current passes through the surface close to the gate oxide (Si-SiO$_2$ interface). Figure 44 shows that the collector current densities normalized by I_C/P_E for three different emitters are almost identical. This proves that the net collector current is a lateral current since the P_E/A_E ratios are different for those emitters.

In this research, I_B primarily follows a vertical current flow path, which is different from reports in the literature, where researchers generally employ a dominant lateral component in the base current (e.g., [92]). The utility of this new approach is shown in Figure 44, which reveals the same base current densities (I_B/A_E) for the same three devices with different emitter areas and P_E/A_E ratios.

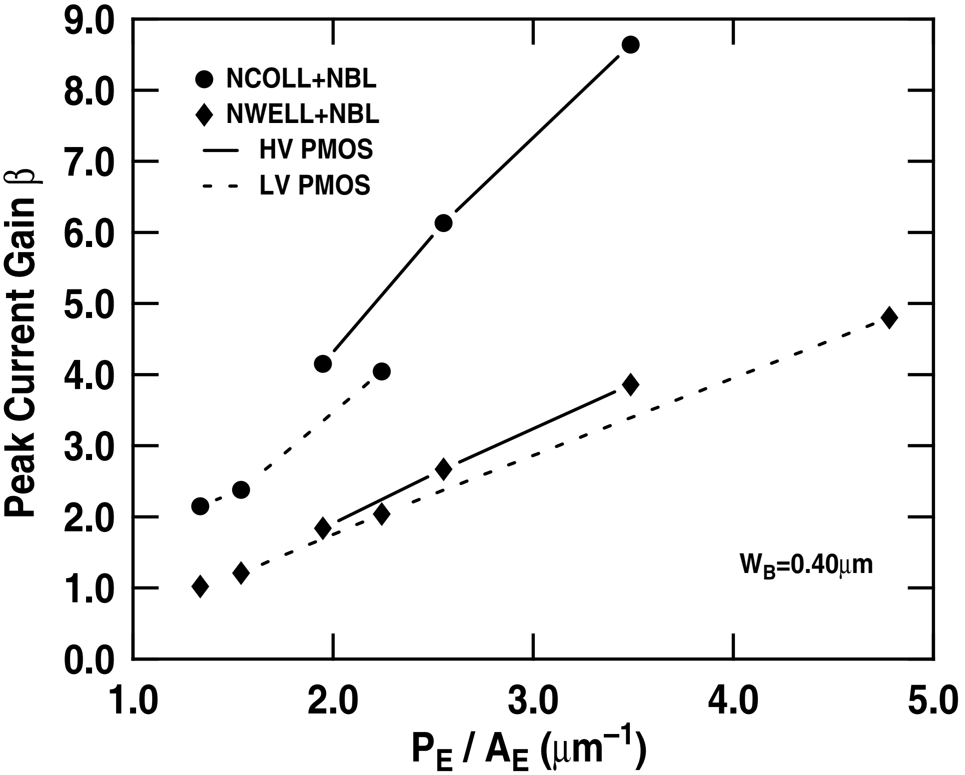

Figure 45: β as a function of P_E/A_E for lateral a *pnp* BJT with $W_B = 0.40\mu m$. HV pMOS has HiPLDD in both the emitter and the collector. LV pMOS has no HiPLDD.

A high P_E/A_E ratio is desired in order to obtain a high current gain since I_B is proportional to A_E, while I_C has a linear dependence on P_E. All four of the possible structures presented in Figure 45 confirm that the current gain β increases as P_E/A_E increases, and clearly defines an optimal device layout path.

Fig. 46 shows the measured cut-off frequency f_T characteristics. The peak f_T occurs at $I_C \approx$ 0.13 mA. For $V_{BC} = 0.5$ V, peak f_T is around 2.47 GHz. For $V_{BC} = 1.5$ V, peak f_T approaches 2.87 GHz. 2-D MEDICI simulation results confirm the validity of the f_T measurements (Fig. 46), and suggest that these devices can achieve a sufficiently good *ac* performance to make them suitable

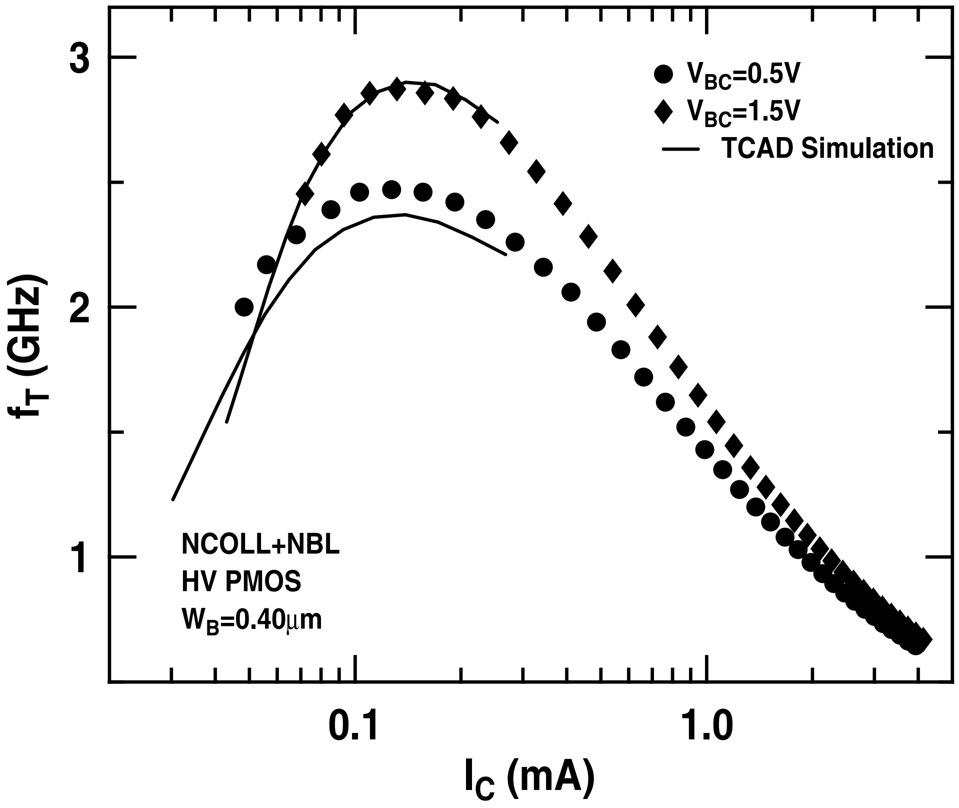

Figure 46: Typical cut-off frequency f_T for a lateral *pnp* BJT built with the NCOLL + NBL profile, HV pMOS, and $W_B = 0.40 \mu m$.

for certain types of lower frequency circuits.

6.3 LFN in Lateral BJTs

Due to the different transport directions of I_C and I_B in these devices, it is not possible to utilize standard measurement approaches for the equivalent base current noise spectral density (S_{IB}) reported previously in vertical and lateral *pnp* BJTs [1][52][64]. Instead, the collector current noise power spectral density (S_{IC}), converted by S_{VC}/R_L^2, is used here to characterize the noise physics for lateral devices. Figure 47 shows the typical noise power spectral densities measured for the lateral devices used in this investigation.

Considering the strong dependence of the *dc* characteristics on the base doping profile and the emitter geometry, it is useful to compare the LFN of devices with different base doping profiles and geometries is compared. Figure 48 shows S_{IC} at 10 Hz measured from devices with the same NCOLL + NBL profile but different emitter geometries. The magnitude of S_{IC} for these devices

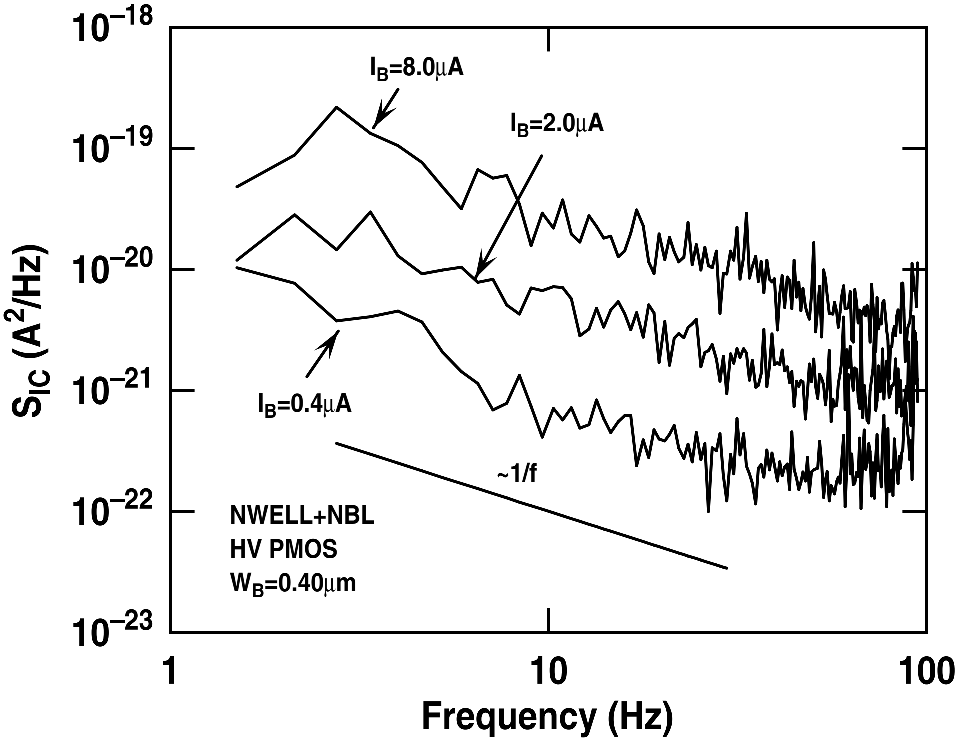

Figure 47: Typical collector current noise power spectral densities for lateral *pnp* BJTs with the NWELL + NBL profile, HV pMOS and $W_B = 0.40 \mu m$ (V_{GB}=1.0 V (pMOS is off)).

is proportional to $I_C^{1.8}$, but has no significant dependence on the emitter area. In contrast, the LFN for the NWELL + NBL profile has a strong dependence on the emitter area (Figure 49). Furthermore, S_{IC} as a function of A_E is shown in Figure 50, which demonstrates that S_{IC} is inversely proportional to A_E, although $I_C \propto P_E$. In addition, S_{IC} for the NWELL + NBL profile has less dependence on I_C ($S_{IC} \propto I_C^{1.2}$).

Interestingly, optimized lateral *pnp* BJTs, despite lateral transport devices, exhibit much better LFN performance than standard pMOS transistors, and are even better than their vertical counterparts. For a 25 GHz peak f_T vertical *pnp* SiGe HBT, for example, that has a similar emitter area, S_{IC} at 10 Hz is around 6 × 10^{-18} A^2/Hz at I_C = 0.05 mA, compared to S_{IC} at 10 Hz of the lateral device of only 1 × 10^{-19} A^2/Hz.

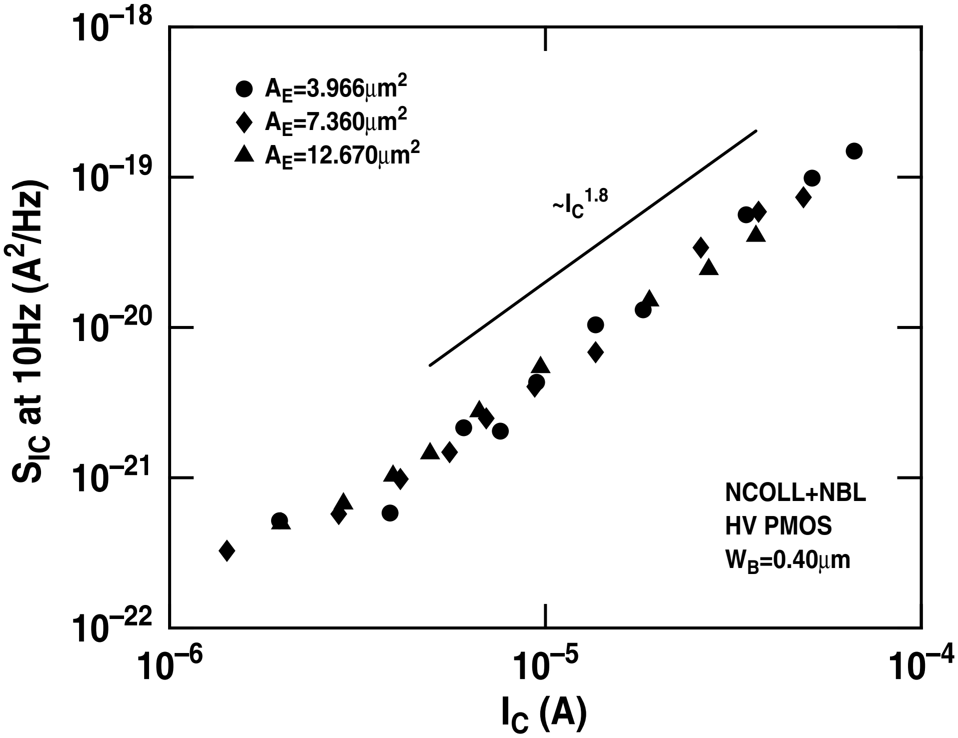

Figure 48: S_{IC} at 10 Hz as a function of I_C for lateral *pnp* BJTs with the NCOLL + NBL profile (V_{GB}=1.0 V (pMOS is off)).

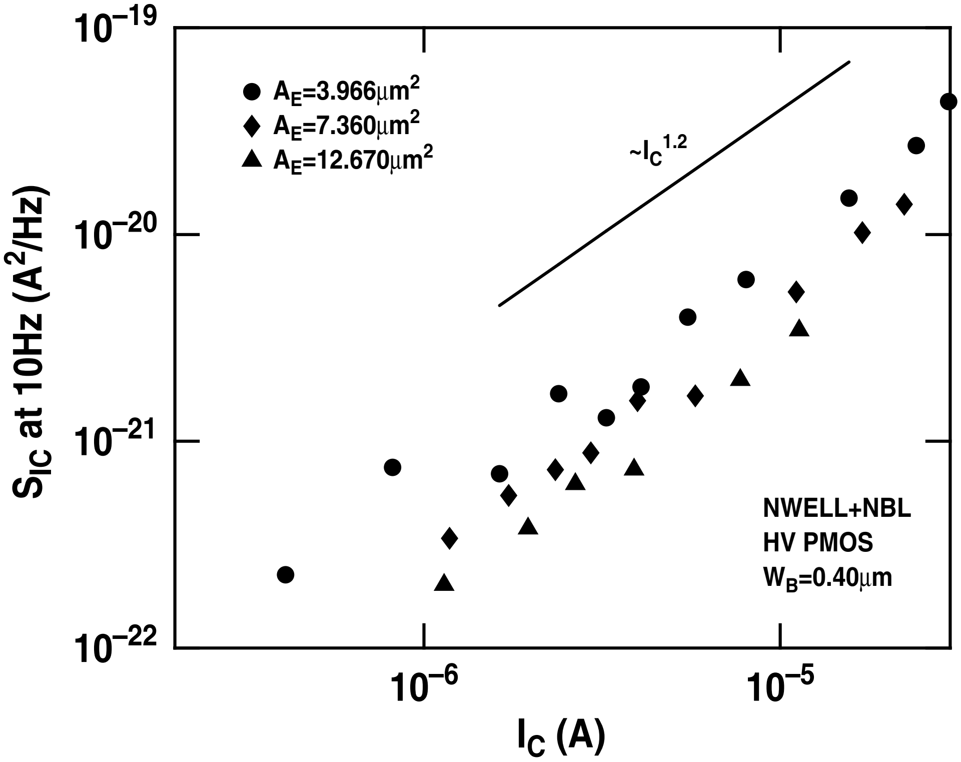

Figure 49: S_{IC} at 10 Hz as a function of I_C for lateral *pnp* with the NWELL + NBL profile (V_{GB}=1.0 V (pMOS is off)).

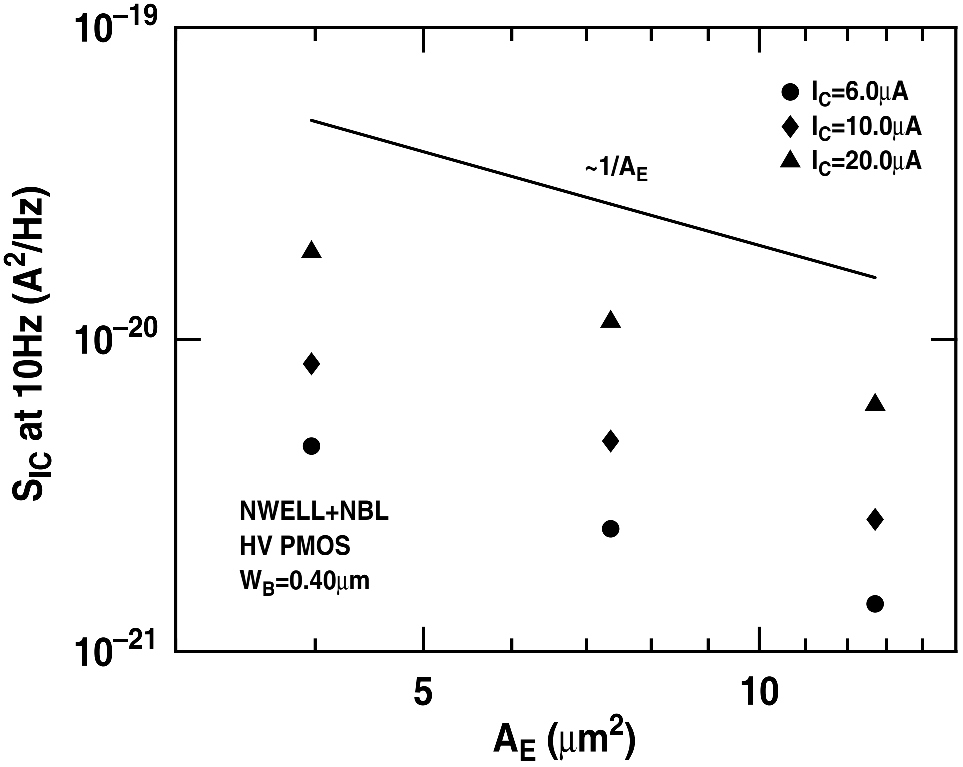

Figure 50: Calculated S_{IC} as a function of A_E for lateral *pnp* BJTs with the NWELL + NBL profile. V_{GB}=1.0V (PMOS off).

CHAPTER VII

CONCLUSIONS AND FUTURE WORK

The contributions made by this work can be summarized as follows:

1. For the first time, a comprehensive assessment of the LFN characteristics of complementary SiGe HBTs has been conducted. The LFN of complementary SiGe HBTs was probed using a novel dual-channel base-collector low-frequency noise measurement system. The system setup, which combines the coherence measured between those two channels, proves that there is a single dominant noise source within the complementary SiGe HBT, and this is associated with the base current. The comprehensive study included an investigation of the effects of the interfacial oxide layer, temperature, proton radiation, and geometric scaling. The Gummel characteristics demonstrate that interfacial oxide buried between the polysilicon emitter and the monosilicon emitter in complementary SiGe HBTs can effectively adjust current gain, hence delivering a comparable performance match for complementary devices. However, LFN degrades with increasing interfacial oxide thickness. The experimental data shows that the magnitude of LFN has an exponential dependence on the interfacial oxide thickness. The variable temperature measurements, which are very useful in probing the noise physics, showed that LFN has a very weak dependence on temperature (close to $1/T$). The LFN of *pnp* SiGe HBTs is almost unaffected by proton radiation. However, the magnitude of the LFN in *npn* SiGe HBTs significantly increases after proton radiation, providing indirect proof that *pnp* devices naturally have higher trap densities than *npn* devices. Furthermore, the dependence of LFN in *npn* SiGe HBTs on the base current changes from I_B^2 to I_B at low biasing, which indicates a fundamental difference between pre and post radiation *pnp* devices. Testing devices with different emitter areas demonstrated that devices with small emitter areas experience higher noise variance, which means that small-size devices suffer more from singular traps.

2. A comprehensive study of LFN in *npn* devices with variable device dimensions was conducted including investigations of the effect of varying emitter length, the distance between the emitter edge and the shallow trench (XEC), and the distance between the shallow trench and the deep trench (XTC). The Gummel characteristics of devices with different emitter lengths demonstrated that the base current has a significant component fluxing in the lateral direction. LFN measured from devices with different emitter lengths displayed a quadratic dependence on the base current and was inversely proportional to the emitter perimeter. This proves that low-frequency noise from the diffusion base current is generated at the emitter perimeter, not over the emitter area, as reported previously. Investigation of devices with different XEC showed that devices with shorter XCE have higher LFN and less dependence on the base current. However, no significant difference was found in the LFN of devices with different XTC.

3. A comprehensive assessment of LFN theories was included in the research study. The LFN investigated in this work is mainly explained by three models: 1) the carrier random-walk model, 2) the two-step tunneling model, and 3) the tunneling assisted trapping model. The carrier random-walk model predicts that LFN will have I_B^2, $1/T$, and $1/A$ dependence. When the base current tunnels through IFO, it is modulated by the surface potential at the IFO-monosilicon interface, while the surface potential is modulated by the charges accumulated at the IFO-monosilicon interface. If the charges are captured by the interface states and randomly emitted-recaptured among different interface states, it will generate LFN with a $1/f$ shape. In addition, the effective area may be close to either the emitter area or the area at the emitter perimeter. The two-step tunneling model is based on a similar mechanism to that invoked in the carrier random-walk model, where the charges are captured by the interface states. The charges may then be captured by traps inside the oxide layer and stay for a long time. Since the thickness of the IFO is very small in our case, the two-step tunneling model cannot be used to predict $1/f$ noise, but is useful in explaining the small-size effect, which has a Lorentzian spectrum. The tunneling assisted trapping model predicts that LFN originates primarily from the spacer oxide covering the E-B junction. LFN predicted by this model can be used to explain LFN with a non-quadratic dependence on the base current.

4. A comprehensive assessment of approaches to characterizing the LFN and optimizing the performance of lateral BJTs was also performed. To optimize the current gain and the subthreshold leakage, several different structure configurations were explored. For a four terminal lateral *pnp* BJT, the most promising structure available is a device fabricated with the HiPLDD implantation in both the emitter and the collector, exactly as a HV pMOS. For the NCOLL + NBL profile, the base width can be chosen to be $0.35\mu m$ to obtain the best trade-off between β and the subthreshold leakage. The NWELL + NBL profile offers the smallest subthreshold leakage; however, a shorter base width is required to make its β comparable to that of the NCOLL + NBL profile. The peak current gain β increases with increases in the P_E/A_E ratio. Consequently, a large P_E/A_E ratio is preferred. LV pMOS devices are a preferred starting point, and have a slightly higher β than the HV pMOS starting point. Choosing a LV pMOS path, however, requires the sacrifice of the subthreshold leakage.

   The LFN characteristics for the NCOLL + NBL profile and the NWELL + NBL profile have many differences. For the NCOLL + NBL profile, S_{IC} has an $I_C^{1.8}$ dependence and no dependence on emitter area, which suggests that the fundamental noise sources are due to mobility fluctuations. The $1/f$ noise for the NWELL + NBL profile, on the other hand, has a near-linear I_C dependence, ($S_{IC} \propto I_C^{1.2}$) and is proportional to $1/A_E$. This indicates that the dominant noise sources lie in the E-B junction for the NWELL + NBL device, and thus that the noise sources only affect part of I_C.

In the future, this work should be extended as follows:

1. Characterize the properties of the IFO-monosilicon interface, especially the interface density and the interface capacitance.

2. Characterize the radiation effects on *npn* SiGe HBTs with significantly different P_E/A_E ratios to verify the tunneling assisted trapping model.

3. Characterize the temperature dependence of LFN for devices with significant break-up, which demonstrate the cubic dependence of LFN on the IFO thickness at room temperature.

APPENDIX A

DERIVATION OF FLUCTUATIONS FROM TRAPS

A.1 Fluctuations from Thermodynamics

The microscopic theory of thermodynamic fluctuations, originally elucidated by Einstein, expresses the entropy $S^{(ep)}$ as

$$S^{(ep)} = klnW + const. \tag{93}$$

with W the "thermodynamic probability" [93][94]. The quantity W, as stated by Einstein, measures the number of different ways to realize a given thermodynamic state, which means it is a large integer. Assuming during a long time t, the system spends a total of time t_i in the state Γ_i. Hence, it is expected that t_1, $t_2 \cdots t_m$ are proportional to the probabilities W_1, $W_2 \cdots W_m$. It follows that t_1/t, $t_2/t \cdots t_m/t$ are also proportional to the probabilities W_1, $W_2 \cdots W_m$. (93) can be revised to

$$S_i^{(ep)} = kln(\frac{t_i}{t}) + const. \tag{94}$$

where $S_i^{(ep)}$ is the entropy in the state Γ_i. Introducing a distribution-function $K(a_1, \cdots, a_m)$,

$$\int \cdots \int K(a_1, \cdots, a_m) da_1 \cdots da_m = 1 \tag{95}$$

This represents the possibility of any states, where $a_1, \cdots, a_m$ are the variables that can change the state of the system. For example, $t_i/t \approx K(a_1^{(i)}, \cdots, a_m^{(i)})$ with $a_1^{(i)}, \cdots, a_m^{(i)}$ only exist for the state Γ_i. Therefore, (93) can be rewritten to

$$S^{(ep)}_{1\cdots m} = kln[K(a_1, \cdots, a_m)] + const. \tag{96}$$

Differentiating (96) yields

$$K(a_1, \cdots a_m)\frac{dS^{(ep)}_{1\cdots m}}{da_i} = k\frac{dK(a_1, \cdots a_m)}{da_i} \tag{97}$$

The variation of a_i is expressed by

$$\alpha_i = a_i - < a_i > \tag{98}$$

Hence,

$$\begin{aligned} < \alpha_i \frac{dS^{(ep)}_{1\cdots m}}{da_i} > &= \int_{-\infty}^{\infty} \cdots \int_{-\infty}^{\infty} \alpha_i \frac{dS^{(ep)}_{1\cdots m}}{da_i} K(a_1, \cdots a_m) da_1 \cdots da_m \\ &= k\int_{-\infty}^{\infty} \cdots \int_{-\infty}^{\infty} \alpha_i \frac{dK(a_1, \cdots a_m)}{da_i} da_1 \cdots da_m \\ &= k\int_{-\infty}^{\infty} \alpha_i \frac{dK(a_i)}{da_i} da_i \\ &= k[\alpha_i K(a_i)]_{-\infty}^{\infty} - k\int_{-\infty}^{\infty} K(a_i) da_i \\ &= -k \end{aligned} \tag{99}$$

Here, the term $k[\alpha_i K(a_i)]_{-\infty}^{\infty}$ vanishes because $K(a_i)$ at infinity is zero. Otherwise, $<\alpha_i dS^{(ep)}_{1\cdots m}/da_i>$ would be infinite. Using the same treatment,

$$< \alpha_j \frac{dS^{(ep)}_{1\cdots m}}{da_i} >= 0 \tag{100}$$

Close to the equilibrium state, the entropy can be expanded to

$$S_{1\cdots m}^{(ep)} = S_0^{(ep)} - \frac{1}{2}\sum_{ij} s_{ij}\alpha_i\alpha_j \tag{101}$$

where

$$s_{ij} = s_{ji} = -\frac{\partial^2 S_{1\cdots m}^{(ep)}}{\partial a_i \partial a_j} \tag{102}$$

and higher terms are neglected [93][94]. Thus,

$$\frac{\partial S_{1\cdots m}^{(ep)}}{\partial a_i} = -\sum_{j=1}^{m} s_{ij}\alpha_j \tag{103}$$

Substituting (103) into (99) and (100)

$$\sum_{j=1}^{m} s_{ij} < \alpha_i\alpha_j >= k\delta_{ij} = \begin{cases} k \ (i = j) \\ 0 \ (i \neq j) \end{cases} \tag{104}$$

Finally, the moments of this distribution express as

$$< \alpha_i\alpha_j >= k(s^{-1})_{ij} \tag{105}$$

Taking entropy to be the basic thermodynamic potential, the force conjugated with variation α_i to restore the equilibrium state is defined by

$$X_i = \frac{\partial S^{(ep)}}{\partial \alpha_i} = -\sum_{j} s_{ij}\alpha_j \tag{106}$$

Hence,

$$s_{ij} = -\frac{\partial^2 S^{(ep)}}{\partial \alpha_i \partial \alpha_j} = -\frac{\partial X_i}{\partial \alpha_j} \tag{107}$$

Therefore, (106) can be inverted to

$$\alpha_i = -\sum_i (s^{-1})_{ij} X_j \tag{108}$$

Hence,

$$(s^{-1})_{ij} = -\frac{\partial \alpha_i}{\partial X_j} = -\frac{\partial a_i}{\partial X_j} \tag{109}$$

Substituting (109) into (105), the moments are redefined as

$$< \alpha_i \alpha_j >= -k \frac{\partial a_i}{\partial X_j} \tag{110}$$

where all X's except X_j are held fixed.

Thermodynamic forces, or the external forces acting on the system, are conventionally expressed as the derivatives of internal energy,

$$P_i = \frac{\partial U(\vec{a})}{\partial a_i} \tag{111}$$

Hence, work done by the system is given by,

$$\triangle w = -\sum P_i da_i \tag{112}$$

The heat flux into the system is defined by,

$$\triangle Q = \triangle U - \sum P_i da_i \tag{113}$$

The variation of entropy is given by,

$$dS^{(ep)} = \frac{\triangle Q}{T} = \frac{dU}{T} - \sum \frac{P_i da_i}{T} \tag{114}$$

At equilibrium, the forces defined by entropy yield

$$X_i = \frac{\partial S^{(ep)}}{\partial a_i} = -\frac{P_i}{T} \tag{115}$$

Substituting (115) into (110), the moments can be rewritten to

$$< \alpha_i \alpha_j >= kT \frac{\partial a_i}{\partial P_j} \tag{116}$$

where T and all expect P_j are held fixed.

A.2 Fluctuations from Traps

If there is a trap states density per unit energy N_t (in units of $cm^{-3}\cdot\mathrm{eV}^{-1}$, an electron density associated with a trap Fermi level F_t, using Fermi statistics, can be found from

$$n_t = N_t f(E_t) = \frac{N_t}{1 + exp(\frac{E_t - F_t}{kT})} \tag{117}$$

where E_t is the trap energy. In this case, the variation of internal energy is

$$\begin{aligned} \triangle U &\approx \int_0^{F_t + \triangle F_t} N_t f(E_t) E_t dE_t - \int_0^{F_t} N_t f(E_t) E_t dE_t \\ &\approx \frac{1}{2} N_t [(F_t + \triangle F_t)^2 - F_t^2] \\ &\approx N_t F_t \triangle F_t \end{aligned} \tag{118}$$

The variation of n_t is

$$\triangle n_t = N_t \triangle F_t \tag{119}$$

Therefore, the external force in this case is

$$P \approx \frac{\triangle U}{\triangle n_t} = F_t \tag{120}$$

Hence, the moments for the fluctuation of n_t are

$$\begin{aligned} < (\triangle n_t)^2 > &= kT \frac{\partial n_t}{\partial F_t} \\ &= -kT [f(E_t)]^2 \cdot \frac{-1}{kT} exp(\frac{E_t - F_t}{kT}) N_t \\ &= N_t f(E_t)[1 - f(E_t)] \end{aligned} \tag{121}$$

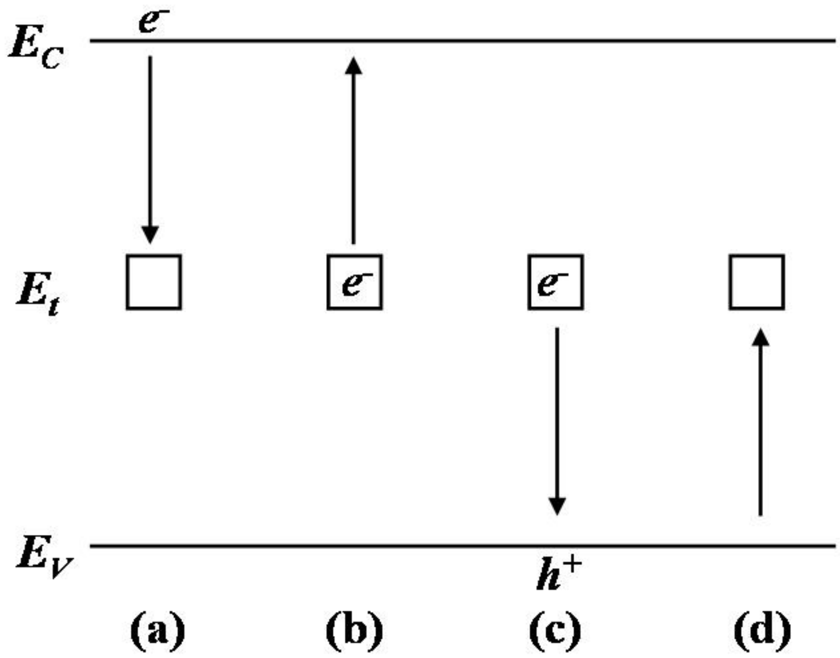

Figure 51: The processes involved in recombination through traps: (a) electron capture, (b) electron emission, (c) hole capture, (d) hole emission.

A.3 Derivation of Trap Distribution

According to the SRH model, the basic processes include electron capture, electron emission, hole capture, and hole emission, as shown in Figure 51 [95]. The rates of capture and emission are $f_p(E_t)N_tc_n(E)f(E)N(E)dE$ and $f(E_t)N_te_n(E)f_p(E)N(E)dE$ respectively, where E is the electron energy, f_p=1-f, $f(E)$ is the Fermi distribution for electron with Fermi level F_n, c_n is the average probability per unit time that an electron is captured by an empty trap, e_n is the average probability per unit time that an electron is emitted by an occupied trap, and N is the quantum state density. Hence, the net rate of capture for the energy interval dE is given in the form

$$dU_{cn} = [f_p(E_t)f(E) - \frac{e_n(E)}{c_n(E)}f(E_t)f_p(E)]N_tc_n(E)N(E)dE \tag{122}$$

At thermal equilibrium condition, dU=0. Hence,

$$\frac{e_n(E)}{c_n(E)} = \frac{f_p(E_t)f(E)}{f(E_t)f_p(E)} = exp(\frac{E_t - F_t + F_n - E}{kT}) \tag{123}$$

Since F_n=F_t in thermal equilibrium, (123) can be rewritten to

$$\frac{e_n(E)}{c_n(E)} = exp(\frac{E_t - E}{kT}) \tag{124}$$

Substituting (124) into (122)

$$dU_{cn} = [1 - exp(\frac{F_t - F_n}{kT})]f_p(E_t)N_t f(E)N(E)c_n(E)dE \tag{125}$$

Integrating (125) from the bottom of the conduction band to all higher levels yields

$$\begin{aligned} U_{cn} &= [1 - exp(\frac{F_t - F_n}{kT})]f_p(E_t)N_t \int_{E_c}^{\infty} f(E)N(E)c_n(E)dE \\ &\approx [1 - exp(\frac{F_t - F_n}{kT})]f_p(E_t)N_t \int_{E_c}^{\infty} exp(\frac{F_n - E}{kT})N(E)c_n(E)dE \\ &= [1 - exp(\frac{F_t - F_n}{kT})]f_p(E_t) \cdot N_C exp(\frac{F_n - E_C}{kT}) \cdot \frac{N_t}{N_C} \int_{E_C}^{\infty} exp(\frac{E_C - E}{kT})c_n(E)N(E)dE \\ &= [1 - exp(\frac{F_t - F_n}{kT})]f_p(E_t)nC_n \end{aligned} \tag{126}$$

where

$$n = N_C exp(\frac{F_n - E_C}{kT}) \tag{127}$$

is the electron density in the conduction band,

$$C_n = \frac{N_t}{N_C}\int_{E_C}^{\infty} exp(\frac{E_C - E}{kT})c_n(E)N(E)dE \tag{128}$$

and N_C is the effective density of states in the conduction band. Furthermore,

$$exp(\frac{F_t - F_n}{kT})f_p(E_t)n = N_C f(E_t)exp(\frac{E_t - E_C}{kT}) = n_1 f(E_t) \tag{129}$$

where

$$n_1 = N_C exp(\frac{E_t - E_C}{kT}) \tag{130}$$

Therefore, the net rate of electron capture (126) is rewritten to

$$U_{cn} = C_n n f_p(E_t) - C_n n_1 f(E_t) \tag{131}$$

A similar treatment can be carried out for the net rate of hole capture, which is given by

$$U_{cp} = C_p p f(E_t) - C_p p_1 f_p(E_t) \tag{132}$$

For the steady state condition, the net rate of electron capture must be equal to that of hole capture. Therefore,

$$C_n n f_p(E_t) - C_n n_1 f(E_t) = C_p p f(E_t) - C_p p_1 f_p(E_t) \tag{133}$$

The solution for $f(E_t)$ yields

$$f(E_t) = \frac{C_n n + C_p p_1}{C_n(n + n_1) + C_p(p + p_1)} \tag{134}$$

Assuming the capture coefficients (C_n and C_p for electrons and holes are very close, (134) can be rewritten to

$$f(E_t) = \frac{n + p_1}{n + n_1 + p + p_1} \tag{135}$$

with

$$n = n_i exp(\frac{E_{Fn} - E_i}{kT}) \tag{136}$$

and

$$p = n_i exp(\frac{E_i - E_{Fp}}{kT}) \tag{137}$$

Here, E_{Fn} and E_{Fp} are the electron and hole quasi-Fermi levels, respectively, n_i is the intrinsic carrier density, and E_i is the midgap energy. Substituting (136) into (130), n_1 can be changed to

$$\begin{aligned} n_1 &= N_C exp(\frac{E_{Fn} - E_C}{kT}) \cdot exp(\frac{E_t - E_{Fn}}{kT}) \\ &= n_i exp(\frac{E_{Fn} - E_i}{kT}) \cdot exp(\frac{E_t - E_{Fn}}{kT}) \\ &= n_i exp(\frac{E_t - E_i}{kT}) \end{aligned} \tag{138}$$

Applying the similar treatment to p_1,

$$p_1 = n_i exp(\frac{E_i - E_t}{kT}) \tag{139}$$

Taking a *pnp* device as an example, (135) can then be rewritten to

$$f(E_t) = \frac{\frac{n}{p} + \frac{p_1}{p}}{\frac{n}{p} + 1 + \frac{n_1+p_1}{p}} \tag{140}$$

Since $p \gg n$ (heavily doped), $n/p \approx 0$. Substituting (136), (137), (138) and (139) into (140),

$$f(E_t) = \frac{1}{1 + exp(2\frac{E_t - E_i}{kT}) + exp(\frac{E_t - E_{FP}}{kT})} \approx \frac{1}{1 + exp(\frac{E_t - E_{FP}}{kT})} \tag{141}$$

Hence, $f(E_t)[1 - f(E_t)]$ can be considered as a quasi delta function at E_{FP} with magnitude 1/4. Finally, (142) is revised to

$$< (\triangle n_t)^2 >= \frac{1}{4} N_t(E_{FP}) \tag{142}$$

In Section 3.4, E_{FP} is set to E_{FNm} as the majority carrier quasi-Fermi level at the IFO-monosilicon interface.

A.4 Derivation of Trap Life Time

Using a p type material as an example, the net rate of hole capture is given by

$$dU_{cp} = f(E_t)N_t c_p f_p(E)N(E)dE - f_p(E_t)N_t e_p f(E)N(E)dE \tag{143}$$

where c_p and e_p are the average probabilities per unit time that a hole will be captured and emitted by an occupied trap state, respectively. If one assumes that only traps at a tunneling distance z dominate the hole capture process, the net rate is defined by, using (143),

$$\begin{aligned} U_{cp} &= N_t(z)f(E_t)c_p(z)\int_{-\infty}^{E_V} f_p(E)N(E)dE - N_t(z)f_p(E_t)\int_{-\infty}^{E_V} e_p(z)f(E)N(E)dE \\ &= N_t(z)f(E_t)c_p(z)p - N_t(z)f_p(E_t)e'_p(z) \end{aligned} \tag{144}$$

At equilibrium, U_{cp}=0. Hence,

$$N_t(z)f(E_t)c_p(z)p = N_t(z)f_p(E_t)e'_p(z) \tag{145}$$

Therefore,

$$\begin{aligned} \frac{e'_p}{c_p} &= \frac{N_t f(E_t)p}{N_t f_p(E_t)} = n_i exp(\frac{E_i - E_{Fp}}{kT})/exp(\frac{E_t - F_t}{kT}) \\ &= n_i exp(\frac{E_i - E_t}{kT}) \\ &= p' \end{aligned} \tag{146}$$

Since the trapping-detrapping process dominates in the hole capture, as assumed, (144) can be rewritten to

$$\begin{aligned} U_{cp} &= \frac{\partial[N_t(z)f(E_t)]}{\partial t} \\ &= [c_p(z)p + e'_p(z)]N_t(z)f(E_t) - N_t(z)e'_p(z) \end{aligned} \tag{147}$$

Neglecting the variation from p, the variation in occupied states $N_t(z)f(E_t$ is defined by

$$\frac{\partial\triangle[N_t(z)f(E_t)]}{\partial t} = [c_p(z)p + e'_p(z)]\triangle[N_t(z)f(E_t)] \tag{148}$$

Hence,

$$\triangle[N_t(z)f(E_t)] \propto exp\{[c_p(z)p + e'_p(z)]t\} \tag{149}$$

with the trap life time given by, using (146),

$$\tau(z) = \frac{1}{c_p(z)(p + p')} \tag{150}$$

According to the well-kown WKB model, $c_p(z)$ is expressed by

$$c_p(z) = c_p(0)P_h(z) \tag{151}$$

with

$$P_h(z) \approx exp(-\frac{4\pi z}{h}\sqrt{2m_h^* q\chi_h}) = exp(-\frac{z}{\lambda}) \tag{152}$$

Substituting (151) into (150) yields

$$\tau(z) = \frac{1}{c_p(0)(z)(p + p')}exp(\frac{z}{\lambda}) = \tau_s exp(\frac{z}{\lambda}) \tag{153}$$

APPENDIX B

THE TUNNELING COMPONENT OF THE BASE CURRENT

Following [96][97], the electron tunneling current through the IFO, which is the dominant component of the base current, is defined by

$$I = \frac{4\pi q m_e^* A}{h^3} \int_{E_x}^{\infty} \{f(E)_{poly} - f(E)_{mono}]\} dE \int_0^{\infty} P_e(E_x) dE_x \tag{154}$$

where m_e^* is the effective electron mass, $f(E)_{poly}$ and $f(E)_{mono}$ are the Fermi-Dirac distribution functions for electrons at the polysilicon-IFO and the monosilicon-IFO interfaces, respectively, E_x is the energy component of E, which belongs to the momentum component perpendicular to IFO, and the tunneling probability P_e is given by

$$P_e(E_x) \approx exp[-2t_{ox}\sqrt{\frac{8\pi^2 m_e^*}{h^2}(q\chi_e + E_x)}] \tag{155}$$

where χ_e is the workfunction of IFO as shown in Figure 8 [96][98]. The "supply function" can be given by

$$\begin{aligned}
\textstyle\int_{E_x}^{\infty} \quad & \{f(E)_{poly} - f(E)_{mono}\} dE \\
= \quad & \int_{E_x}^{\infty} \{\frac{1}{1 + exp[\frac{E - E_{FN}(poly)}{kT}]} - \frac{1}{1 + exp[\frac{E - E_{FN}(mono)}{kT}]}\} dE \\
= \quad & \int_{E_x}^{\infty} \{\frac{exp[\frac{E_{FN}(poly) - E}{kT}]}{1 + exp[\frac{E_{FN}(poly) - E}{kT}]} - \frac{exp[\frac{E_{FN}(mono) - E}{kT}]}{1 + exp[\frac{E_{FN}(mono) - E}{kT}]}\} dE \\
= \quad & kTln\frac{1 + exp[\frac{E_{FN}(poly) - E_x}{kT}]}{1 + exp[\frac{E_{FN}(mono) - E_x}{kT}]}
\end{aligned} \tag{156}$$

where $E_{FN}(poly)$ is the minority carrier quasi-Fermi level at IFO-polysilicon inter face, and $E_{FN}(mono)$ is the minority carrier quasi-Fermi level at IFO-monosilicon inter face. Using Taylor series,

$$ln\{1+exp[\frac{E_{FN}(poly)-E_x}{kT}]\} \approx exp[\frac{E_{FN}(poly)-E_x}{kT}] \tag{157}$$

and

$$ln\{1+exp[\frac{E_{FN}(mono)-E_x}{kT}]\} \approx exp[\frac{E_{FN}(mono)-E_x}{kT}] \tag{158}$$

Substituting (157), (158), and (156) into (154) yields

$$\begin{aligned} I &\approx \frac{4\pi q m_e^* A}{h^2} kTP_e \int_0^\infty \{exp[\frac{E_{FN}(poly)-E_x}{kT}] - exp[\frac{E_{FN}(mono)-E_x}{kT}]\} dE_x \\ &\approx \frac{4\pi q m_e^* A}{h^2} (kT)^2 P_e \{exp[\frac{E_{FN}(poly)}{kT}] - exp[\frac{E_{FN}(mono)}{kT}]\} \end{aligned} \tag{159}$$

Here, P_e is treated as a constant because most of the electrons are close to the conduction band. When the tunneling current is large enough, $E_{FN}(mono) - E_{FN}(mono) >> kT$. Then, the term associated with polysilicon can be neglected. Hence, (159) can be rewritten to

$$I \approx -\frac{4\pi q m_e^* A}{h^2} (kT)^2 P_e exp[\frac{E_{FN}(mono)}{kT}] \tag{160}$$

The electron concentration at the IFO-monosilicon interface is

$$\begin{aligned} n_{mono} &\approx \frac{n_{imono}^2}{N_A} exp[\frac{q(V_{EB}-\psi_{mono})}{kT}] \\ &\approx N_C exp[\frac{E_{FN}(mono)}{kT}] \end{aligned} \tag{161}$$

where n_{imono} is the intrinsic electron concentration at the IFO-monosilicon interface, N_C is the state density above the conduction band, N_A is the doping level in the monosilicon, and E_C at the IFO-monosilicon interface equals to 0 (Figure 8). Substituting (161) into (160) yields

$$I = -\frac{4\pi q m_e^*}{h^3}(kT)^2 P_e \frac{n_{imono}^2}{N_A N_C} exp[\frac{q(V_{EB} - \psi_{mono})}{kT}] \tag{162}$$

Therefore, I is rewritten to

$$I = I_0 exp(-\frac{q\psi_{mono}}{kT}). \tag{163}$$

REFERENCES

[1] E. Zhao, A. K. Sutton, B. M. Haugerud, J. D. Cressler, P. W. Marshall, R. A. Reed, B. El-Kareh, S. Balster, and H. Yasuda "The effects of radiation on $1/f$ noise in complementary ($npn + pnp$) SiGe HBTs," *IEEE Trans. Nucl. Sci.* vol. 51, pp. 3243-3249, 2004.

[2] E. Zhao, R. Krithivasan, A. K. Sutton, Z. Jin, J. D. Cressler, B. El-Kareh, S. Balster, and H. Yasuda, "An Investigation of Low-Frequency Noise in Complementary SiGe HBTs," *IEEE Trans. Elec. Dev.*, vol. 53, pp. 329-338, Feb., 2006.

[3] E. Zhao, J. D. Cressler, M. El-Diwany, T. L. Krakowski, A. Sadovnikov, and D. Kocoski, "On the geometrical dependence of low-frequency noise in SiGe HBTs," *Sol. State Elec.* under review.

[4] E. Zhao, M. El-Diwany, J. D. Cressler, J. Shibley, A. Sadovnikov, D. Kocoski, and T. L. Krakowski, "Optimization of lateral pnp BJTs found in BiCMOS technologies," *Proc. IEEE BCTM*, paper 13.2, 2005.

[5] M. J. Kirton and M. J. Uren, "Noise in solid-state microstructures: a new perspective on individual defects, interface states and low-frequency ($1/f$) noise," *Advances in Phys.*, vol. 38, pp. 367-468, 1989.

[6] J. Johnson, "Thermal agitation of electricity in conductors," *Phys. Rev.*, vol. 32, pp. 97-109, 1928.

[7] H. Nyquist, "Thermal agitation of electric charge in conductors," *Phys. Rev.*, vol. 32, pp. 110-113, 1928.

[8] A. Van Der Ziel, "Noise in solid state devices," *Advances in Electronics and Electron Phys.*, vol. 46, pp. 313-382, 1978.

[9] W. Schottky, "Über spontane stromschwankungen in verschiedenen elektrizitätsleitern," *Annalen der Physik*, vol. 57, pp. 541-567, 1918.

[10] S. O. Rice, "Mathematical analysis of random noise," *Bell Syst. Tech. J.*, vol. 23, pp. 282-332, 1944.

[11] M. von Haartman, M. Sandén, and M. Östling, "Random telegraph signal noise in SiGe heterojunction bipolar transistors," *J. Appl. Phys.*, vol. 92, pp. 4414-4421, 2002.

[12] S. Machlup, "Noise in semiconductors: spectrum of a two parameter random signal," *J. Appl. Phys.*, vol. 25, pp. 341-343, 1954.

[13] C. H. Suh, "Spectral density due to the fluctuation of the total number of carriers in a semiconductor," *J. Appl. Phys.*, vol. 57, pp. 318-321, 1985.

[14] A. L. Mc Whorter, *Semiconductor Surface Physics,* University of Pennsylvania Press, Philadelphia, 1957.

[15] A. Van Der Ziel, "Flicker noise in electronic devices," *Advances in Electronics and Electron Phys.*, vol. 49, pp. 225-297, 1979.

[16] M. J. Buckingham, *Noise in Electronic Devices and Systems,* Ellis Horwood Seies in Electrical and Electronic Engineering, 1983.

[17] C. T. Sah, "Theory of low-frequency generation noise in junction-gate field-effect transistors," *Proc. IEEE*, vol. 52, pp. 795-814, 1964.

[18] H. S. Fu and C. T. Sah, "Theory and experiments on surface $1/f$ noise," *IEEE Trans. Elec. Dev.*, vol. ED-19, pp. 273-285, 1972.

[19] M. Lax, "Fluctuations from the nonequilibrium steady state," *Rev. of Modern Phys.*, vol. 32, pp. 25-64, 1960.

[20] F. N. Hooge and L. K. J. Vandamme, "Lattice scattering causes $1/f$ noise," *Phys. Lett.*, vol. 66A, pp. 315-316, 1978.

[21] J. T. M. Stroeken and T. G. M. Kleinpenning, "$1/f$ noise of deformed crystals," *J. Appl. Phys.*, vol. 47, pp. 4691-4692, 1976.

[22] J. D. Cressler and G. Niu, *Silicon-Germanium Heterojunction Bipolar Transistors*, Artech House, 2003.

[23] W. Shockley, U.S. Patent 2,569,347, issued 1951.

[24] H.Kroemer, "Theory of a wide-gap emitter for transistors," *Proc. IRE,* vol. 45, pp. 1535-1537, 1957.

[25] B. S. Meyerson, "Low-temperature silicon epitaxy by ultrahigh vacuum/chemical vapor deposition," *Appl. Phys. Lett.*, vol. 48, pp. 797-799, 1986.

[26] T. O. Sedgwick, M. Berkenblit, and T. S. Kuan, "Low-temperature selective epitaxial growth of silicon at atmospheric pressure," *Appl. Phys. Lett.*, vol. 54, pp. 2689-2691, 1989.

[27] S. S. Iyer, G. L. Patton, S. L. Delage, S. Tiwari, and J. M. C. Stork, "Silicon-germanium base heterojunction bipolar transistors by molecular beam epitaxy," *Tech. Dig. IEEE Int. Elect. Dev. Meeting,* pp. 874-876, 1987.

[28] J. S. Rieh, B. Jagannathan, H. Chen, *et al.*, "SiGe HBTs with cut-off frequency of 350 GHz," *Tech. Dig. IEEE Int. Elec. Dev. Meeting,* pp. 771-774, 2002.

[29] E. J. Prinz, P. M. Garone, P.V. Schwartz, X. Xiao, and J.C. Sturm, "The effect of emitter-base spacers and strain-dependent density-of-states in Si/SiGe/Si heterojunction bipolar transistors," *Tech. Dig. IEEE Int. Elec. Devices Meeting*, pp.639-642, 1989.

[30] C. T. Chuang, J. D. Cressler, and J. D. Warnock, "*ac*-coupled complementary push-pull ECL circuits with 34fJ power-delay product," *Elec. Lett.*, vol. 29, pp. 1938-1939, 1993.

[31] J. D. Cressler, *The Silicon Heterostructure Handbook: Materials, Fabrication, Devices, Circuits, and Applications of SiGe and Si Strained-Layer Epitaxy*, CRC Press, New York, NY, 2005.

[32] D. L. Harame, J. M. C. Stork, B. S. Meyerson, *et al.*, "SiGe-base *pnp* transistors fabrication with n-type UHV/CVD LTE in a "NO DT" process," *Tech. Dig. IEEE Sym. on VLST Technology*, pp.47-48, 1990.

[33] D. L. Harame, B. S. Meyerson, E. F. Crabbé, *et al.*, "55 GHz polysilicon-emitter graded SiGe-base *pnp* transistors," *Tech. Dig. IEEE Sym. on VLST Technology*, pp.71-72, 1991.

[34] B. El-Kareh, S. Balster, W. Leitz, *et al.*, "A 5V complementary-SiGe BiCMOS technology for high-speed precision analog circuits," *Proc. IEEE BCTM*, pp. 211-214, 2003.

[35] S. P. O. Bruce, L. K. J. Vandamme and A. Rydberg, "Measurement of low-frequency base and collector current noise and coherence in SiGe heterojunction bipolar transistors using transimpedence amplifiers," *IEEE Trans. Electron Devices*, vol. ED-46, pp. 993-1000, 1999.

[36] R. Plana, L. Escotte, J. P. Roux, J. Graffeuil, A. Gruhle, and H. Kibbel, "$1/f$ noise in self-aligned Si/SiGe heterojunction bipolar transistors," *IEEE Elec. Dev. Lett.*, vol. 16, pp.58-60, 1995.

[37] A. Gruhle, and C. Mahner, "Low $1/f$ noise SiGe HBT's with application to low phase noise microwave oscillators," *IEEE Elec. Dev. Lett.*, vol. 33, pp. 2050-2052, 1997.

[38] B. van Haaren, M. Regis, O. Llopis, L. Escotte, A. Gruhle, C. Mahner, R. Plana, and J. Graffeuil, "Low-frequency noise properties of SiGe HBT's and application to ultra-low phase-noise oscillators", *IEEE Trans. Micro. Theory and Tech.*, vol. 46, pp. 647-652, 1998.

[39] J. A. Babcock, J. D. Cressler, L. S. Vempati, A. J. Joseph, and D. L. Harame, "Correlation of low-frequency noise and emitter-base reverse-bias stress in epitaxial Si- and SiGe-base bipolar transistors," *Technical Digest of the 1995 IEEE International Electron Devices Meeting*, pp.357-360, 1995.

[40] J.A. Babcock, J.D. Cressler, L.S. Vempati, S.D. Clark, R.C. Jaeger, and D.L. Harame, "Ionizing radiation tolerance of high performance SiGe HBTs grown by UHV/CVD," *IEEE Trans. Nucl. Sci.,* vol. 42, pp. 1558-1566, 1995.

[41] Z. Jin, J. D. Cressler, N. Guofu, A. J. Joseph, "Impact of geometrical scaling on low-frequency noise in SiGe HBTs," *IEEE Trans. Elec. Dev.*, vol. 50, pp. 676-682, 2003.

[42] M.J. Kumar and V. Parihar, "Surface accumulation layer transistor (SALTran): a new bipolar transistor for enhanced current gain and reduced hot-carrier degradation," *IEEE Trans. Dev. Material Reliab.*, vol. 4, pp. 509-515, 2004.

[43] A. Tamba *et al.*, "CMOS-compatible lateral bipolar transistor for BiCMOS technology. II. Experimental results," *IEEE Trans. Elec. Dev.*, vol. 39, pp. 1865-1869, 1992.

[44] F. Corsi, M. Di Ciano and C. Marzocca, "DC characterization of lateral bipolar devices in standard CMOS technology: a new model for base current partitioning," *Sol. State Elec.*, vol. 43, pp. 883-889, 1999.

[45] J. Ho, T. Huang and M. Chen, "High gain p-n-p gated lateral bipolar action in a fully depleted counter-type channel p-MOSFET structure," *Sol. State Elec.*, vol. 39, pp. 261-267, 1996.

[46] Y. Kook *et al.*, "Surface accumulated lateral npn BJT's characteristics in SOI NMOSFETs," *IEEE Trans. Electron Devices*, vol. 46, pp. 1917-1919, 1999.

[47] J.C. Sturm *et al.*, "A lateral silicon-on-insulator bipolar transistor with a self-aligned base contact" *IEEE Electron Device Letters*, vol. 8, pp. 104-106, 1987.

[48] Z. Yan, M.J. Deen, and D.S. Malhi, "Gate-controlled lateral PNP BJT: characteristics, modeling and circuit applications," *IEEE Trans. Electron Devices*, vol. 44, pp. 118-128, 1997.

[49] H. A. W. Markus and T. G. M. Kleinpenning, "Low-frequency noise in polysilicon emitter bipolar transistors," *IEEE Trans. Elec. Dev.*, vol. 42, pp. 720-727, 1995.

[50] T. G. M. Kleinpenning, "On low frequency noise in tunnel diodes," *Sol. State Elec.*, vol. 21, pp. 927-931, 1978.

[51] T. G. M. Kleinpenning, "On low frequency noise in tunnel diodes," *Sol. State Elec.*, vol. 25, pp. 79-80, 1982.

[52] M. J. Deen *et al.*, "Measurements and comparison of low-frequency noise in *npn* and *pnp* polysilicon emitter bipolar junction transistors," *J. Appl. Phys.*, vol. 84, pp. 625-633, 1998.

[53] S. Jarrix *et al.*, "Noise correlation measurements in bipolar transistors. I. Theoretical expressions and extracted current spectral densities," *J. Appl. Phys.*, vol. 81, pp. 2651-2657, 1997.

[54] M. J. Deen and F. Pascal, "Review of low-frequency noise behaviour of polysilicon emitter bipolar junction transistors", *IEE Proc. Circuits Devices Syst.*, vol. 152, pp. 125-137, 2004.

[55] H. C. de Graaff and J. G. de Groot, "The SIS tunnel emitter: A theory for emitters with thin interface layers," *IEEE Trans. Elec. Dev.*, vol. ED-26, pp. 1771-1776, 1979.

[56] P. Ma *et al.*, "An analytical model for determining carrier transport mechanism of polysilicon emitter bipolar transistors," *IEEE Trans. Elec. Dev.*, vol. 42, pp. 1789-1797, 1995.

[57] A. A. Eltoukhy and D. J. Roulston, "The role of the interfacial layer in polysilicon emitter bipolar transistors," *IEEE Trans. Elec. Dev.*, vol. ED-29, pp. 1862-1869, 1982.

[58] M. M. Mandurah, K. C. Saraswat, and T. I. Kamins, "A model for conduction in polycrystalline silicon - part I: theory," *IEEE Trans. Elec. Dev.*, vol. ED-28, pp. 1163-1171, 1981.

[59] E. L. Murphy and R. H. Good Jr., "Thermionic emission, field emission, and the transition region," *Phys. Rev.*, vol. 102, pp. 1464-1473, 1956.

[60] V. Kumar, and W. E. Dahlke, "Low-frequency noise in $Cr - SiO_2 - n - Si$ tunnel diodes," *IEEE Trans. Elec. Dev.*, vol. 24, pp. 146-153, 1977.

[61] O. Jäntsch, "Flicker $(1/f)$ noise generated by a random walk of electrons in interfaces," *IEEE Trans. Elec. Dev.*, vol. 34, pp. 1100-1115, 1987.

[62] S. Christensson, I. Lundström, and C. Svensson, "Low frequency noise in MOS transistors - I theory," *Sol. State Elec.*, vol. 11, pp. 797-812, 1968.

[63] C. T. Sah, "Theory of low-frequency generation noise in junction-gate field-effect transistors," *Proc. of the IEEE*, vol. 52, pp. 795-814, 1964.

[64] E. Zhao *et al.*, "Temperature dependence of $1/f$ noise in polysilicon-emitter bipolar transistors," *IEEE Trans. Elec. Dev.*, vol. 49, pp. 2230-2236, 2001.

[65] A. Mounib *et al.*, "Low-frequency $(1/f)$ noise model for the base current in polysilicon emitter bipolar junction transistors," *J. Appl. Phys.*, vol. 79, pp. 3330-3336, 1996.

[66] H. Hong, "Low-frequency noise study in electron devices: review and update," *Microelec. Reliability.*, vol. 43, pp. 585-599, 2003.

[67] J. S. Hamel *et al.*, "Two-dimensional analysis of emitter resistance in the presence of interfacial oxide breakup in polysilicon emitter bipolar transistors," *IEEE Trans. on Electron Device* vol. 39, pp. 2139-2146, 1992.

[68] N. F. Rinaldi, "On the modeling of polysilicon emitter bipolar transistors," *IEEE Trans. on Electron Device* vol. 44, pp. 395-403, 1997.

[69] M. J. Deen, and E. Simoen, "Low-frequency noise in polysilicon-emitter bipolar transistors", *IEE Proc. Circuits Devices Syst.*, vol. 149, pp. 40-50, 2002.

[70] Z. Jin *et al.*, "Using proton irradiation to probe the origins of low-frequency noise variations in SiGe HBTs," *IEEE Trans. Nucl. Sci.*, vol. 50, pp. 1816-1820, 2003.

[71] E. Simoen *et al.*, "Impact of polysilicon emitter interfacial layer engineering on the l/f noise of bipolar transistors," *IEEE Trans. Elec. Dev.*, vol. 43, pp. 2261-2268, 1996.

[72] P. W. Marshall *et al.*, "Particle induced bit errors in high performance fiber optic data links for satellite data management," *IEEE Trans. Nucl. Sci.*, vol. 41, pp. 1958-1965, 1994.

[73] K. M. Murray, W. J. Stapor, and C. Castenada, "Proton beam facility for single event research," *Nucl. Instrum. Methods*, vol. B56/57, p. 616, 1991.

[74] M. J. Deen, J.Iiowski, and P.Yang, "Low-frequency noise in polysilicon-emitter bipolar junction transistors," *J. Appl. Phys.*, vol. 77, pp. 6278-6288, 1995.

[75] M. Sanden, O. Marinov, and M. J. Deen, "A new model for the low-frequency noise and the noise level variation in polysilicon emitter BJTs," *IEEE Trans. Elec. Dev.*, vol. 49, pp. 514-520, Mar. 2002.

[76] Z. Yu, B. Riccò, and B. W. Dutton, "A comprehensive analytical and numerical model of polysilicon emitter contacts in bipolar transistors," *IEEE Trans. Elec. Dev.*, vol. ED-31, pp. 773-784, 1984.

[77] S. Kar, "Interface charge characteristics of MOS structure with different metals on steam grown oxides," *Sol. State Elec.*, vol. 18, pp. 723-732, 1975.

[78] M. Sandén, B. G. Malm, J. V. Grahn, M. Östling, "Decreased low-frequency noise by hydrogen passivation of polysilicon-emitter bipolar transistors," *Microelectronics Reliability* vol. 40, pp. 1863-1867, 2000.

[79] Z. Jin, G. Niu, J. D. Cressler, C. J. Marshall, P. W. Marshall, H. S. Kim, R. A. Reed, and D. L. Harame, "$1/f$ noise in proton-irradiated SiGe HBTs," *IEEE Trans. Nuclear Sci.* vol. 48, pp. 2244-2249, 2001.

[80] Z. Jin, J. D. Cressler, G. Niu, P. W. Marshall, H. S. Kim, R. A. Reed, and A. J. Joseph, "Proton response of low-frequency noise in 0.20 μm 90 GHz f_T UHV/CVD SiGe HBTs," *Sol. State Elec.*, vol. 47, pp. 39-44, 2003.

[81] P. Llinares, D. Celi, O. Roux-dit-Buisson, G. Ghibaudo, and J. A. Chroboczek, "Dimension scaling of $1/f$ noise in the base current of quasiself-aligned polysilicon-emitter bipolar junction transistors," *J. Appl. Phys.*, vol. 82, pp. 2671-2675, 1997.

[82] P. Llinares, G. Ghibaudo, and J. A. Chroboczek, "On noise sources in hot electron-degraded bipolar junction transistors," *J. Appl. Phys.*, vol. 82, pp. 2676-2679, 1997.

[83] X. Y. Chen, M. J. Deen, Z. X. Yan, and M. Schroter, "Effects of emitter dimensions on low-frequency noise in double-polysilicon BJTs," *Elec. Lett.*, vol. 34, pp. 219-220, 1998.

[84] C. Delseny, A. Pénarier, F. Pascal, S. G. Jarrix, and P. Llinares, "Comparison of low-frequency noise and high-frequency performances of double and simple polysilicon Bi-CMOS BJT," *Microelectronics Reliability*, vol. 40, pp. 1869-1874, 2000.

[85] M. J. Deen and S. Rumyantsev, "Low-frequency noise in complementary *npn* and *pnp* polysilicon-emitter bipolar junction transistors," *Microelectronics Reliability*, vol. 40, pp. 1855-1861, 2000.

[86] M. Sandén, O. Marinov, M. J. Deen, and M. Östling, "A new model for the low-frequency noise and the noise level variation in polysilicon-emitter BJTs," *IEEE Trans. Elec. Dev.*, vol. 49, pp. 514-520, 2002.

[87] N. Valdaperez, J. M. Routoure, D. Bloyet, R. Carin, and S. Bardy, "Size effects on the DC characteristics and low-frequency noise of double polysilicon NPN bipolar transistors," *Microelectronics Reliability*, vol. 45, pp. 1167-1173, 2005.

[88] P. Benoit, J. Raoult, C. Delseny, F. Pascal, L. Snadny, J. C. Vildeui, M. Marin, B. Martinet, D. Cottin, and O. Noblanc, "Dc and low frequency noise analysis of hot-carrier induced degradation of low complexity 0.13 μm CMOS bipolar transistors," *Microelectronics Reliability*, vol. 45, pp. 1800-1806, 2005.

[89] J. N. Burghartz, J. Y. Sun, C. L. Stanis, S. R. Mader, and J. D. Warnock, "Identification of perimeter depletion and emitter plug effects in deep-submicrometer, shallow-junction polysilicon emitter bipolar transistors," *IEEE Trans. Elec. Dev.*, vol. 39, pp. 1477-1489, 1992.

[90] H. M. Rein, "A simple method for separation of the internal and external (peripheral) currents of bipolar transistors," *Sol. State Elec.*, vol. 27, pp. 625-631, 1984.

[91] M. Schròter and D. J. Walkey, "Physical modeling of lateral scaling in bipolar transistors," *IEEE J. Solid-State Cir.*, vol.31, pp.1484-1492, 1996.

[92] K. Joardar, "An improved analytical model for collector currents in lateral bipolar transistors," *IEEE Trans. Elec. Dev.*, vol. 41, pp. 373-382, 1994.

[93] L. Onsager, "Reciprocal relations in irreversible processes. I," *Physical Rev.*, vol. 37, pp. 405-426, 1931.

[94] L. Onsager, "Reciprocal relations in irreversible processes. II," *Physical Rev.*, vol. 38, pp. 2265-2279, 1931.

[95] W. Shockley and W. T. Read, "Statistics of the recombinations of holes and electrons," *Physical Rev.*, vol. 87, pp. 835-842, 1952.

[96] R. Stratton, "Volt-current characteristics for tunneling through insulating films," *J. Phys. Chem. Solids*, vol. 4, pp. 1177-1190, 1962.

[97] P. J. Price and J. M. Radcliffe, "Esaki tunneling," *IBM J. Res. Dev.*, vol. 3, pp. 364-371, 1959.

[98] H. C. Card and E. H. Rhoderick, "Studies of tunnel MOS diode, part I," *J. Phys. D: Appl. Phys.*, vol. 4, pp. 1589-1601, 1971.

VITA

Enhai Zhao was born in Nanjing, Jiangsu, P. R. China. He earned his B.E. and M.S. degrees in Electrical Engineering from the Nanjing University of Aeronautics and Astronautics and Nanjing University, China, in 1998 and 2000, respectively, and is currently completing a Ph.D. degree in electrical and computer engineering at the Georgia Institute of Technology in Atlanta, GA.

His research work focuses on low-frequency noise in SiGe HBTs, polysilicon emitter BJTs, and lateral BJTs.